SMIP14

SMIP14 SEMINAR ON
UTILIZATION OF STRONG-MOTION DATA

Berkeley, California
October 9, 2014

PROCEEDINGS

Sponsored by

California Strong Motion Instrumentation Program
California Geological Survey
California Department of Conservation

Co-Sponsors

California Seismic Safety Commission
California Governor's Office of Emergency Services
California Department of Transportation
Office of Statewide Health Planning and Development

The California Strong Motion Instrumentation Program (CSMIP), a program within the California Geological Survey (CGS) of the California Department of Conservation, records the strong shaking of the ground and structures during earthquakes for analysis and utilization by the engineering and seismology communities through a statewide network of strong motion instruments (www.conservation.ca.gov/CGS/smip). CSMIP is advised by the Strong Motion Instrumentation Advisory Committee (SMIAC), a committee of the California Seismic Safety Commission. Major program funding is provided by an assessment on construction costs for building permits issued by cities and counties in California, with additional funding from the California Governor's Office of Emergency Services (Cal OES), the California Department of Transportation (Caltrans) and the Office of Statewide Health Planning and Development (OSHPD).

In July 2001, the California Governor's Office of Emergency Services (Cal OES) began funding for the California Integrated Seismic Network (CISN), a newly formed consortium of institutions engaged in statewide earthquake monitoring that grew out of TriNet, funded by FEMA, and includes CGS, USGS, Caltech and UC Berkeley. The goals are to record and rapidly communicate ground shaking information in California, and to analyze the data for the improvement of seismic codes and standards (www.cisn.org). CISN produces ShakeMaps of ground shaking, based on shaking recorded by stations in the network, within minutes following an earthquake. The ShakeMap identifies areas of greatest ground shaking for use by OES and other emergency response agencies in the event of a damaging earthquake.

The Center for Engineering Strong Motion Data (CESMD) is operated by the CSMIP Program of the CGS in cooperation with the National Strong-Motion Project (NSMP) and the Advanced National Seismic System (ANSS) of the U.S. Geological Survey (USGS). The CESMD builds on and incorporates the CISN Engineering Data Center and will continue to serve the California region while expanding to serve other ANSS regions. The Data Center provides strong-motion data rapidly after a significant earthquake in the United States. Users also have direct access to data from previous earthquakes and detailed information about the instrumented structures and sites. The Data Center is co-hosted by CGS and USGS at www.strongmotioncenter.org

DISCLAIMER

SMIP14

SMIP14 SEMINAR ON
UTILIZATION OF STRONG-MOTION DATA

Berkeley, California
October 9, 2014

PROCEEDINGS

Edited by

Moh Huang

Sponsored by

California Strong Motion Instrumentation Program
California Geological Survey
California Department of Conservation

Co-Sponsors

California Seismic Safety Commission
California Governor's Emergency Services
California Department of Transportation
Office of Statewide Health Planning and Development

PREFACE

The California Strong Motion Instrumentation Program (CSMIP) in the California Geological Survey of the California Department of Conservation established a Data Interpretation Project in 1989. Each year CSMIP Program funds several data interpretation contracts for the analysis and utilization of strong-motion data. The primary objectives of the Data Interpretation Project are to further the understanding of strong ground shaking and the response of structures, and to increase the utilization of strong-motion data in improving post-earthquake response, seismic code provisions and design practices.

As part of the Data Interpretation Project, CSMIP holds annual seminars to transfer recent research findings on strong-motion data to practicing seismic design professionals, earth scientists and post-earthquake response personnel. The purpose of the annual seminar is to provide information that will be useful immediately in seismic design practice and post-earthquake response, and in the longer term, useful in the improvement of seismic design codes and practices. Proceedings and individual papers for each of the previous annual seminars are available in PDF format at http://www.consrv.ca.gov/CGS/smip/proceedings.htm Due to the State budget restraints, CSMIP did not fund as many projects as in other years and did not hold an annual seminar in 2010 or 2011. The SMIP14 Seminar is the twenty-third in this series of annual seminars.

The SMIP14 Seminar is divided into two sessions in the morning and two sessions in the afternoon. The sessions in the morning include four invited presentations. The first session will focus on ground motions and will include an invited presentation by Professor Baker of Stanford University on engineering application of ground motion simulation, and a presentation by Professor Rodriguez-Marek of Virginia Tech on accounting topographic effects in ground motion predication equations. The second session will include presentations of some preliminary results from two CSMIP-funded projects on building code seismic provisions on the direction of loading in building codes by Mr. Lizundia of Rutherford+Chekene and effects of multiple-component ground motion on building response by Professor Bernal of Northeastern University.

The first afternoon session will start with a presentation of the results from the CSMIP-funded project on seismic performance analysis of port structures by Dr. Dickenson of New Albion Geotechnical, followed by an invited presentation on seismic analysis of an instrumented concrete gravity dam by Mr. Schultz of Department of Water resources. The last session will include a presentation of CSMIP-funded project on building modeling sensitivity by Professor Kunnath of UC Davis, followed by an invited presentation by Professor Allen of UC Berkeley on California earthquake early warning system, and highlights of strong-motion data from the M6.0 South Napa earthquake of August 24, 2014 by Dr. Shakal of CSMIP. Individual papers and the proceedings are available to the SMIP14 participants in an USB flash drive, and will be available at the CSMIP website.

Moh Huang
CSMIP Data Interpretation Project Manager

Appreciation to Members of the Strong Motion Instrumentation Advisory Committee

Main Committee

Chris Poland, Chair, Chris D Poland Consulting Engineer
Norman Abrahamson, Pacific Gas & Electric Company
Anil Chopra, UC Berkeley
Bruce Clark, Leighton & Associates
Martin Eskijian, California State Lands Commission (retired)
Wilfred Iwan, California Institute of Technology
Tom Ostrom, Caltrans
Farzad Naeim, Farzad Naeim, Inc.
Marshall Lew, AMEC
Bret Lizundia, Rutherford + Chekene
Robert Anderson (ex-officio), Seismic Safety Commission

Ground Response Subcommittee

Marshall Lew, Chair, AMEC
Abbas Abghari, Caltrans
Brian Chiou, Caltrans
Geoffrey Martin, Univ. of Southern California
Ben Tsai, Pacific Gas & Electric Company (retired)

Buildings Subcommittee

Farzad Naeim, Chair, Farzad Naeim, Inc.
Lucie Fougner, Degenkolb Engineers
Donald Jephcott, Structural Engineer
David Leung, City of San Francisco
Bret Lizundia, Rutherford & Chekene
Eduardo Miranda, Stanford University
John Robb, Structural Engineer
Chris Tokas, Office of Statewide Health Planning and Development
Chia-Ming Uang, UC San Diego

Lifelines Subcommittee

Martin Eskijian, Chair, California State Lands Commission (retired)
Craig Davis, Los Angeles Dept. of Water and Power
David Gutierrez, DWR Division of Safety of Dams
Marsha McLaren, Pacific Gas & Electric Company
Tom Ostrom, Caltrans

Data Utilization Subcommittee

Wilfred Iwan, Chair, California Institute of Technology
Representatives from each Subcommittee

TABLE OF CONTENTS

SMIP14 SEMINAR ON UTILIZATION OF STRONG-MOTION DATA

October 9, 2014

International House at UC Berkeley
2299 Piedmont Avenue, Berkeley, California

PROGRAM

8:15 am **REGISTRATION**

9:15 am **WELCOMING REMARKS**
Farzad Naeim, Strong Motion Instrumentation Advisory Committee (SMIAC)
John Parrish, State Geologist, California Geological Survey

INTRODUCTION
Anthony Shakal, Manager, California Strong Motion Instrumentation Program
Moh Huang, California Strong Motion Instrumentation Program

Session I

Moderator: *Marshall Lew*, AMEC and SMIAC

9:30 am **Ground Motion Simulations: Validation and Application for Civil Engineering Problems**
Jack Baker and *Lynne Burks*, Stanford University

10:00 am **Accounting for Topographic Effects in Ground Motion Prediction Equations**
Manisha Rai and *Adrian Rodriguez-Marek*, Virginia Polytechnic Institute and State University.

10:30 am Break

Session II

Moderator: *Farzad Naeim*, Farzad Naeim, Inc. and SMIAC

11:00 am **Evaluation of ASCE/SEI 7 Direction of Loading Provisions Using CSMIP Records: An Interim Report**
Reid Zimmerman, *Bret Lizundia* and *Saeed Fathali*, Rutherford + Chekene

11:30 pm **Multi-Component Demands from Instrumental Data: Assessment of Seismic Provisions**
Dinosio Bernal, *Lester Silfa* and *Anshuman Kunwar*, Northeastern University

12:00 pm **Lunch**
Lunch will be provided

Session III

Moderator: *Martin Eskijian*, California State Lands Commission and SMIAC

12:50 pm **Seismic Performance Analysis of Pile-Supported Wharves Subjected to Long-Duration Ground Motion**
Stephen Dickenson, *Songtao Yang*, *Doug Schwarm* and *Matt Rees*, New Albion Geotechnical

1:20 pm **Validation of Finite Element Analysis Techniques Using Loma Prieta Recordings at Lower Crystal Springs Dam**
Vojislav Cvijanovic, Mark Schultz, Ingrid Dittmar and *William Fraser,* Department of Water Resources

1:50 pm Break

Session IV

Moderator: *Wilfred Iwan*, Caltech and SMIAC

2:10 pm **Modeling Sensitivity in Commonly Used Computer Programs - Case Studies of Instrumented Steel Moment-Frame Buildings**
Daniel Swensen and *Sashi Kunnath*, UC Davis

2:40 pm **California Earthquake Early Warning System – Status and Future Directions**
Richard Allen, UC Berkeley

3:10 pm **Highlights of Strong-Motion Data from the M6.0 South Napa Earthquake of August 24, 2014**
Anthony Shakal, Hamid Haddadi , Moh Huang, CGS, and *Christopher Stephens*, USGS

3:40 pm **Adjourn**

FLING IN NEAR-FAULT GROUND MOTIONS AND ITS EFFECT ON STRUCTURAL COLLAPSE CAPACITY

Lynne S. Burks[1] and Jack W. Baker[2]

[1] Sandia National Labs, Livermore, CA
[2] Dept. of Civil & Environmental Engineering, Stanford University, Stanford, CA

Abstract

We evaluate the collapse capacity of a nonlinear single degree of freedom (SDOF) system using ground motion records with varying fling properties, including records with static offsets preserved via baseline correction, records with static offsets removed via filtering, and records with artificial static offsets added. Fling is caused by a permanent static offset of the ground and appears as a ramp function in the displacement time history. Due to baseline errors in many acceleration recordings, these static offsets are typically removed via filtering before ground motion records are added to an engineering database, such as the Next Generation Attenuation (NGA) database. Therefore, fling is neglected by default in many engineering applications even though it may affect the dynamic nonlinear response of structures, extreme nonlinear behavior such as collapse, and structures crossing a fault. Some analysts account for fling by adding artificial static offsets to filtered records, but this method has not been rigorously tested and there has been little study on the effects of fling on nonlinear structural behavior and collapse capacity. We found that the collapse capacity of a degrading nonlinear SDOF is similar for two versions of the same ground motion: one with the static offset preserved via baseline correction and one with the static offset removed via filtering. In most cases, the baseline corrected record and the filtered record result in the same collapse capacity, indicating that filtering preserves the dynamic effect of fling even though the static offset is removed. We also found that adding artificial static offsets to filtered records typically results in a conservative estimate of the collapse capacity. In particular, increased amplitude, or static offset, and decreased period, or duration of fling, cause decreased collapse capacity.

Introduction

Near-fault effects, such as directivity and fling, tend to produce intense structural response because of ground motion amplification at long periods [1]. Directivity is caused by the constructive interference of seismic waves as the rupture propagates along the fault and is strongest in the fault normal direction. Fling is caused by a permanent static offset of the ground and is strongest for strike-slip faults in the fault parallel direction. While directivity has received much attention by structural engineers, fling has been largely ignored because static offsets are typically filtered out of ground motion records before being used for engineering analysis.

This document is reprinted from: Burks, Lynne S., and Jack W. Baker. Fling in near-fault ground motions and its effect on structural collapse capacity. *Proceedings of the 10th National Conference in Earthquake Engineering*, Earthquake Engineering Research Institute, Anchorage, AK, 2014.

Raw seismograms recorded from earthquakes contain errors due to noise and baseline offsets from tilting and transducer response to strong shaking. These errors in acceleration are significantly amplified when integrated twice to compute displacement, so analysts address this by processing ground motion records using filtering and baseline correction (Figure 1). Filtering consists of applying a low- and high-pass filter in the frequency domain, and typically removes the static offset from records [2]. Baseline correction removes baseline offsets by fitting and then subtracting a linear trend from the velocity time history, and preserves the static offset [3,4]. However, because the amplitude of the static offset is highly sensitive to the choice of baseline, and baseline correction has a negligible effect on elastic response spectra [3,5], records are typically filtered rather than baseline corrected before being added to an engineering database, such as the Next Generation Attenuation (NGA) database [6].

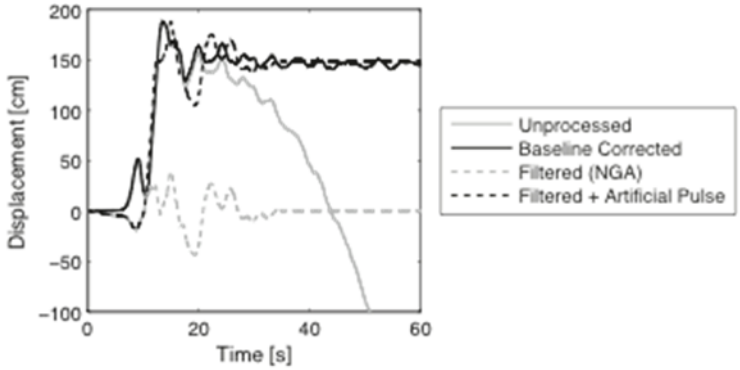

Figure 1. Multiple versions of the displacement time history from the YPT station in the 1999 Kocaeli, Turkey earthquake, including unprocessed (or raw), baseline corrected, filtered (from NGA database), and filtered plus an artificial fling pulse.

Previous studies show that the structural response to near-field and pulse-like ground motions is generally more intense than to far-field ground motions, especially when the pulse period is close to the first or second mode period of the structure, e.g. [7–9]. Some analysts account for this effect by adding artificial fling pulses to filtered ground motions (e.g. Figure 1) [10], but this method neglects the difference in record processing techniques like filtering and baseline correction, which may affect structural response [11]. Also, previous studies do not address the effect of fling on collapse capacity, which is becoming an increasingly important parameter for the assessment of highly nonlinear structures and seismic risk analysis.

Here we compare the collapse capacity of nonlinear SDOF structures using records with static offsets preserved via baseline correction, static offsets removed via filtering from the NGA database, and static offsets included via adding artificial pulses to the filtered NGA record. We find that the baseline corrected record and the filtered record result in similar collapse capacity, and that adding artificial pulses generally decreases the collapse capacity.

Ground Motions

We first consider three types of idealized pulses because though many parametric studies have been done using idealized pulses, e.g. [12–15], none specifically focus on collapse capacity. Then we assess collapse capacity using many variations of three recorded ground motions.

Idealized Pulses

The three idealized pulses are referred to as type *A*, type *B*, and type *C*, where type *A* and type *C* represent fling and type *B* represents a directivity pulse with no static offset (Figure 2). Each pulse is represented by a trigonometric function as follows [15]:

$$a_A(t) = \frac{2\pi D_p}{T_p^2} \sin\left(\frac{2\pi}{T_p}(t - t_1)\right) \quad t_1 \le t < T_p + t_1 \tag{1}$$

$$a_B(t) = \frac{2\pi^2 D_p}{T_p^2} \cos\left(\frac{2\pi}{T_p}(t - t_1)\right) \quad t_1 \le t < T_p + t_1 \tag{2}$$

$$a_C(t) = -\frac{\pi^2 D_p}{2T_p^2} \sin\left(\frac{\pi}{T_p}\left(t - t_1 - \frac{T_p}{2}\right)\right) \quad t_1 \le t < T_p + t_1 \tag{3}$$

where $a_A(t)$, $a_B(t)$, and $a_C(t)$, are the acceleration as a function of time for pulse *A, B,* and *C*, respectively, D_p is the maximum displacement amplitude of the pulse, T_p is the period or duration of the pulse, and t_1 is the arrival time.

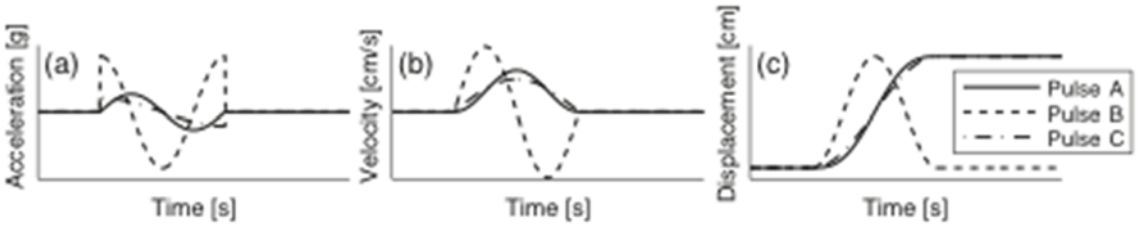

Figure 2. (a) Acceleration, (b) velocity, and (c) displacement time histories of different types of idealized pulses.

We used 40 versions of each pulse type with constant maximum acceleration of the pulse, A_p, and varying T_p (Figure 3). Each set of pulses was also high-pass filtered at a cutoff frequency, f_c, of 0.2 Hz and 0.5 Hz to investigate the effect of record filtering on collapse capacity.

Ground Motion Recordings

We also consider three recorded ground motions: the TCU068-N/S station from the 1999 Chi-Chi, Taiwan earthquake; the GDLC-E/W station from the 2010 Darfield, New Zealand

earthquake; and the YPT-N/S station from the 1999 Kocaeli, Turkey earthquake. These stations have a Joyner-Boore distance of 0, 1.22, and 1.38 km respectively. For each recording, we used a version with static offsets preserved via baseline correction, static offsets removed via filtering from the NGA database [6], and artificial static offsets included via adding pulse *C* with varying fling parameters (displacement amplitude, pulse period, and arrival time) to the filtered version.

For the version with static offsets preserved, we performed baseline correction according to [3] and [4] on raw seismograms from the TCU068 [16], GDLC [17], and YPT stations (Erol Kalkan, personal communication, May 2011). We then fit the functional form for pulse *C* to each baseline corrected displacement time history using global optimization (for more details, see [18]). Fling parameters of the baseline corrected ground motions are shown in

Table 1.

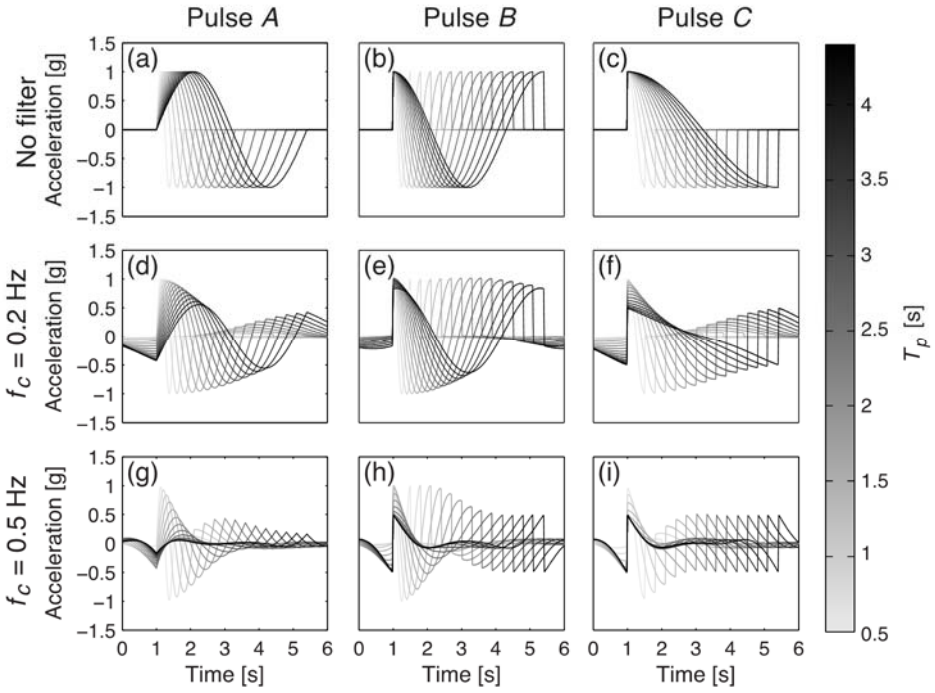

Figure 3. Acceleration time histories of selected pulses used to compute collapse capacity.

Table 1. Fling parameters of the baseline corrected versions of the three ground motion records used in this study, where D_p is displacement amplitude, T_p is pulse period, and t_1 is arrival time.

EQ Name	Year	M_W	Station Name	Orientation	D_p (cm)	T_p (s)	t_1 (s)
Chi-Chi	1999	7.6	TCU068	N/S	551.0	3.19	33.9
Darfield	2010	7.0	GDLC	E/W	134.2	3.37	17.9

Kocaeli	1999	7.5	YPT	N/S	148.4	2.84	10.2

For the versions with artificial static offsets included, we computed many displacement time histories of pulse *C* (using Equation 3) with varying D_p, T_p, and t_1. We varied each fling parameter 40 times while holding the other two parameters constant, resulting in a total of 120 pulse *C* displacements for each recording. We then added the pulse *C* displacements to each filtered NGA recording, representing the way that some analysts add artificial fling to filtered near-fault records [10,19]. Multiple versions of the ground motion from TCU068 with varying D_p are shown in Figure 4. Similarly, T_p and t_1 were also varied for TCU068, and all fling parameters were varied for GDLC and YPT, but figures are omitted here because of space constraints (see [18]).

Structural Analysis

Here we present the results of an incremental dynamic analysis (IDA) performed in OpenSees using ground motions from the previous section. An IDA is performed by incrementally scaling up a single ground motion and computing a structural demand parameter, like interstory drift or floor acceleration, until instability and collapse occurs. The IDA is repeated for a set of ground motions to get a probabilistic description of collapse [20].

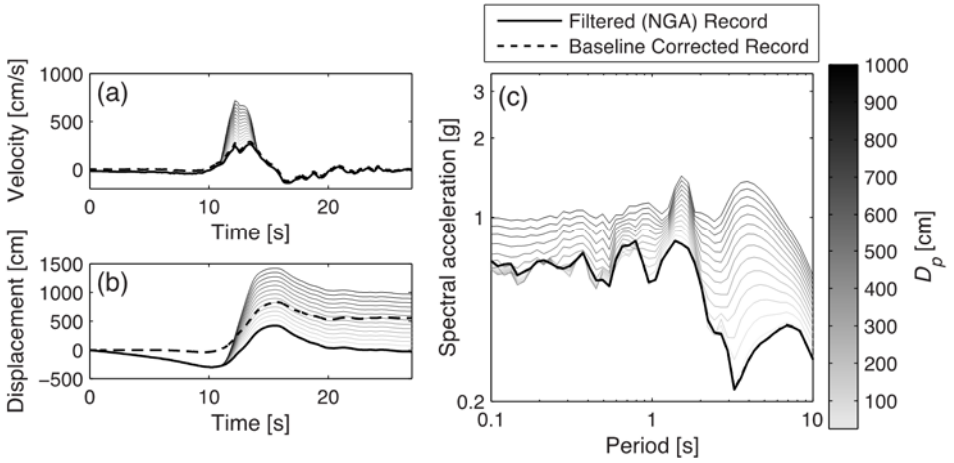

Figure 4. Selected versions of the (a) velocity time history, (b) displacement time history, and (c) response spectra of the ground motion recorded at the TCU068 station during the 1999 Chi-Chi, Taiwan earthquake with varying D_p.

Structures

For this study, we used two nonlinear single degree of freedom (SDOF) structures with different fundamental periods and force-drift backbones which capture the collapse behavior of the structure (Figure 5). SDOF 1 has a natural period of 1.32 s and is based on a SDOF approximation of a 4-story experimental structure [21]. SDOF 2 has a longer period of 3 seconds, which is closer to observed pulse periods from the recorded ground motions. Both SDOFs have a 2% damping ratio and 3% strain hardening ratio.

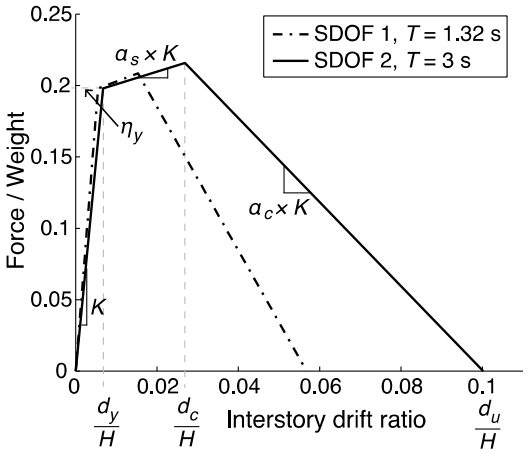

Figure 5. Force-drift backbone of the nonlinear and degrading SDOF structures used in this study, where η_y is yield force normalized by weight, K is stiffness, α_s is strain hardening ratio, α_c is post-capping stiffness ratio, H is SDOF height, d_y is yield displacement, d_c is capping displacement, and d_u is ultimate displacement.

Response to Idealized Pulses

The idealized pulse ground motions were used to perform multiple IDAs on SDOF 1, with ground motions grouped by pulse type and filter cutoff frequency (Figure 6). The filter cutoff frequency of 0.2 Hz has a negligible effect on the collapse capacity for all pulse types, while the cutoff frequency of 0.5 Hz causes an increase in collapse capacity for all pulse types. This increase is likely due to the decrease in energy of the pulses from filtering.

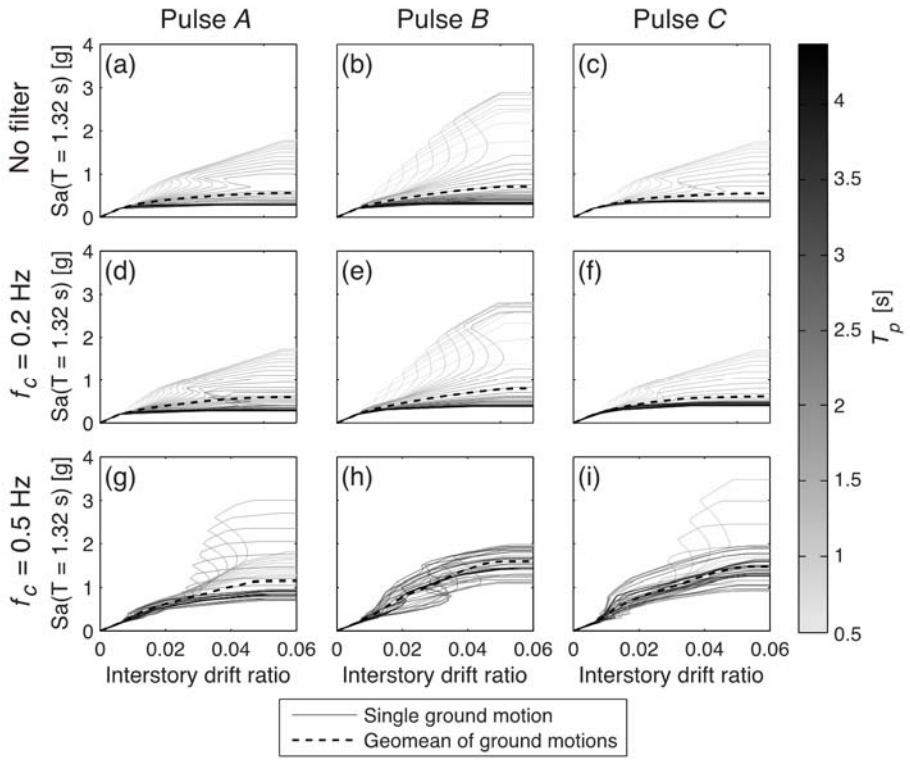

Figure 6. Results of IDA performed on SDOF 1 using idealized pulses with varying filter frequency shown in Figure 3.

Response to Ground Motion Recordings

The collapse capacity of SDOF 1 was computed using all versions of the record from TCU068 (Figure 7), GDLC, and YPT. Because of space constraints, only results from TCU068 are presented here, but the other ground motions show similar trends [18]. For all three records, the version with static offsets preserved via baseline correction and the version with static offsets removed via filtering from the NGA database resulted in similar collapse capacity. This indicates that even though the static offset is removed from the NGA version, the dynamic component of fling is preserved. Also, for most records and fling parameters, adding pulse *C* to the filtered NGA version resulted in decreased collapse capacity. But there were a few notable exceptions where the collapse capacity increased, such as some small displacement amplitudes for the TCU068 record and very short periods for all records.

To investigate possible reasons for the increased collapse capacity, we evaluated the displacement of SDOF 1 as a function of time at varying scale factors until collapse. For the filtered version of the Chi-Chi record, the residual displacement of the SDOF increased with scale factor until collapse occurred in the positive direction (Figure 8a). But when pulse *C* with D_p = 375 cm was added to the filtered version, the residual displacement decreased with scale factor before collapse occurred again in the positive direction, indicating that the pulse pulled the SDOF in the negative direction (Figure 8b). For some ground motions, such as pulse *C* with a very short period of 1 s added to the filtered version, this pull was strong enough to cause collapse in the negative direction (Figure 8c). In this example, we observed that the added pulse

pulled the SDOF in the opposite direction of the filtered record, sometimes causing collapse in the opposite direction, and always increasing the collapse capacity.

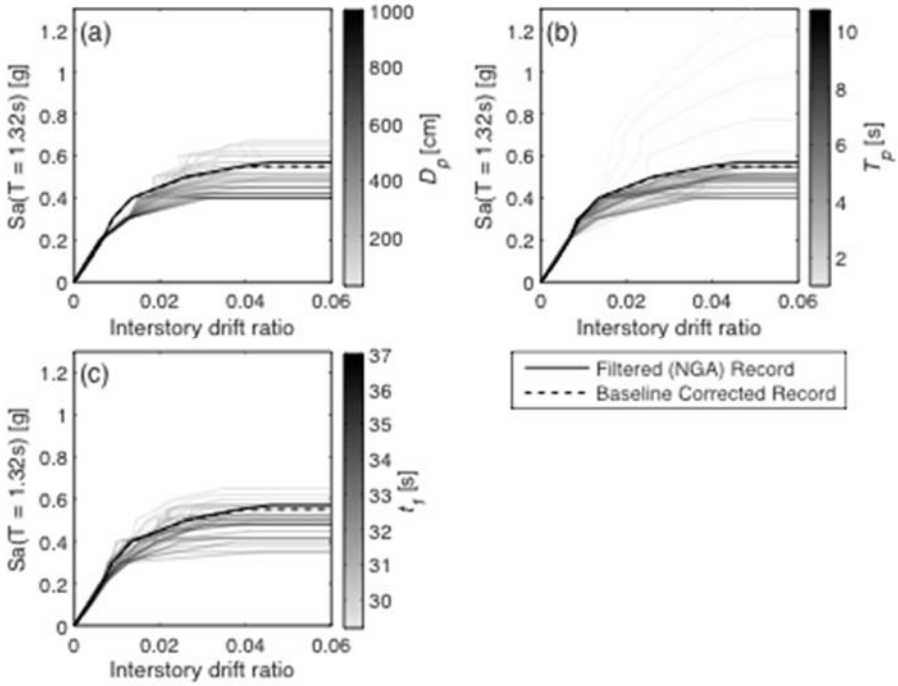

Figure 7. Collapse capacity of SDOF 1 computed using multiple versions of the TCU068 Chi-Chi, Taiwan ground motion, including with static offsets preserved via baseline correction, static offsets removed via filtering from the NGA database, and static offsets included via adding pulse *C* with varying (a) D_p, (b) T_p, and (c) t_1 to the NGA version.

General trends between parameters of the added pulse *C* and collapse capacity were observed. For example, as D_p increased or T_p decreased, the collapse capacity generally decreased, but no such trend was observed for t_1 (Figure 9). For each ground motion with added pulse *C*, we compared the difference between the pulse *C* and baseline corrected fling parameters to the ratio of the collapse capacity from the filtered version with added pulse *C* to the collapse capacity from the baseline corrected version. When the difference between fling parameters (i.e. the x-axis of Figure 9) is zero, we are comparing the baseline corrected version to the filtered version added to pulse *C* with the same fling parameters as the baseline corrected version, and their resulting collapse capacities are not equal. This inequality indicates that adding a fling pulse to the filtered version, even with the "correct" parameters (i.e. parameters same as the baseline corrected version), double counts the effect of fling and causes a conservative estimate of collapse capacity.

We also computed the collapse capacity for SDOF 2 using all versions of the ground motion records, but because the general conclusions are similar to SDOF 1, we only show the results from Darfield in summary form for conciseness (Figure 9). Even though the natural period of SDOF 2 is closer to T_p for all three records, the baseline corrected and filtered versions again result in similar collapse capacity. The versions with static offsets included via adding

pulse *C* to the filtered version nearly always result in decreased collapse capacity. Finally, we again observed that as D_p increased or T_p decreased, the collapse capacity generally decreased.

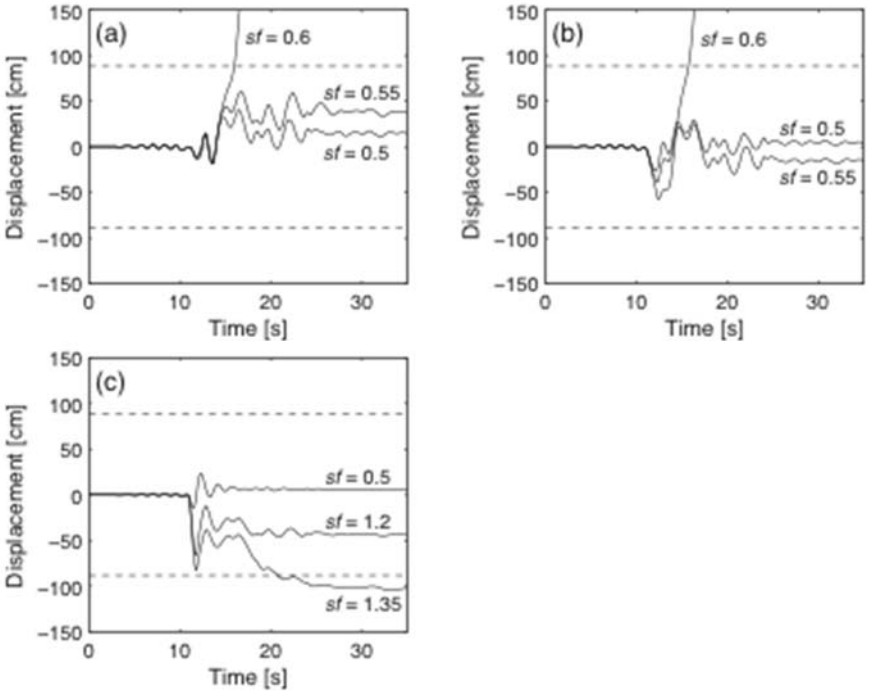

Figure 8. Displacement response of SDOF 1 to multiple versions of the TCU068 Chi-Chi, Taiwan ground motion record scaled at different factors (where *sf* is the scale factor), including (a) the NGA version, (b) pulse *C* with D_p = 375 cm added to the NGA version, and (c) pulse *C* with T_p = 1 s added to the NGA version. Collapse occurs when the displacement of SDOF 1 exceeds the ultimate displacement represented by the dashed line.

Conclusions

We computed the collapse capacity of nonlinear SDOFs using multiple versions of the same ground motion record, including a baseline corrected version with static offsets preserved, a filtered version from the NGA database with static offsets removed, and artificial versions with an idealized pulse added to the filtered record. For all records and two SDOFs with different periods, the baseline corrected and filtered versions resulted in similar collapse capacity. This indicates that even when the static offset is removed via filtering, the dynamic effect of the fling on these structures is preserved. Collapse capacities were considered in this study in order to evaluate fling effects on highly nonlinear structures. Similar conclusions have been drawn for linear SDOFs [5], and these studies indicate that moderately nonlinear structural responses will likely also be insensitive to record processing that removes static fling.

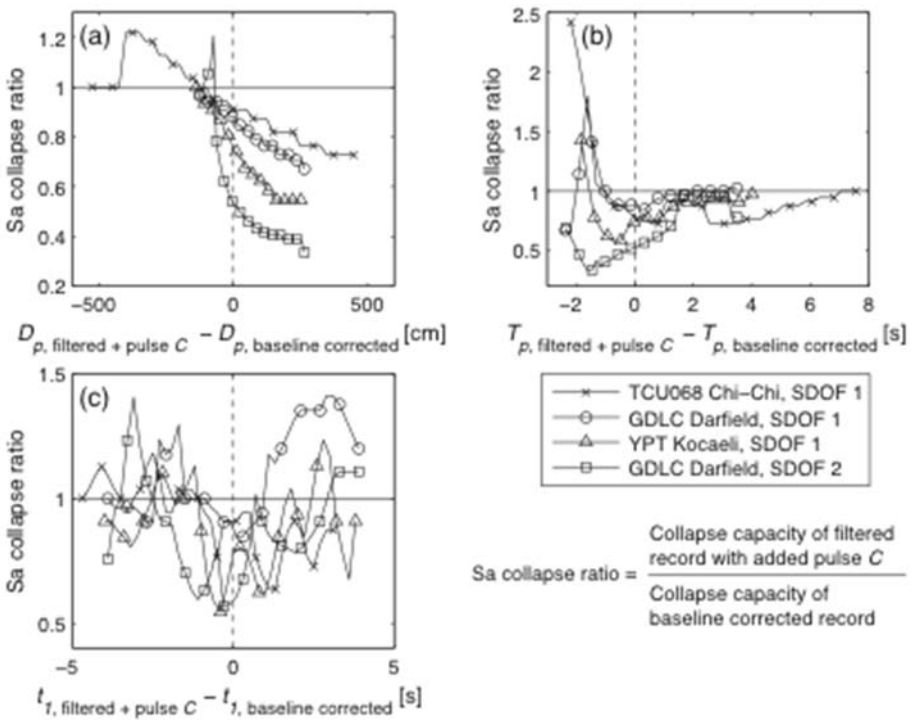

Figure 9. Changes in fling parameter affect the collapse capacity. The x-axis is the difference between (a) D_p, (b) T_p, and (c) t_1 of the filtered version with added pulse C and the baseline corrected version. The y-axis is the ratio of the collapse capacity of the filtered version with added pulse C to the baseline corrected version.

We also evaluated the effect of ground motion filtering on collapse capacity through idealized pulse approximations of fling and directivity. By computing collapse capacities for a range of pulse periods and high-pass filter cutoff frequencies, we concluded that filtering at a low cutoff frequency outside the range of pulse or structural periods has a negligible effect on collapse capacity. But filtering at a high cutoff frequency that approaches the pulse or structural period can increase the collapse capacity, leading to an un-conservative estimate.

By adding artificial fling pulses to filtered records, we observed that as displacement amplitude increased or pulse period decreased, the collapse capacity typically decreased. No such trend was found for the arrival time of the fling pulse. Adding any artificial fling pulse to a filtered record typically resulted in a conservative estimate of collapse capacity. But in a few cases, the artificial fling pulled the SDOF in the opposite direction of the filtered record, sometimes even causing collapse in the opposite direction, and resulted in an un-conservative estimate of collapse capacity.

In conclusion, the collapse capacity of a nonlinear SDOF is similar whether computed with a filtered or baseline corrected version of the ground motion, so either can be used in applications similar to the examples presented here. However, fling may still be important for other engineering applications, such as fault crossings where the main problem is static displacement rather than dynamic response.

References

[1] Somerville PG, Smith NF, Graves RW, Abrahamson NA. Modification of Empirical Strong Ground Motion Attenuation Relations to Include the Amplitude and Duration Effects of Rupture Directivity. *Seismological Research Letters* 1997; **68** (1): 199–222.

[2] Boore DM, Bommer JJ. Processing of strong-motion accelerograms: needs, options and consequences. *Soil Dynamics and Earthquake Engineering* 2005; **25**: 93–115.

[3] Boore DM. Effect of Baseline Corrections on Displacements and Response Spectra for Several Recordings of the 1999 Chi-Chi, Taiwan, Earthquake. *Bulletin of the Seismological Society of America* 2001; **91** (5): 1199–1211.

[4] Wu Y-M, Wu C-F. Approximate recovery of coseismic deformation from Taiwan strong-motion records. *Journal of Seismology* 2007; **11**: 159–170.

[5] Kamai R, Abrahamson N. Are Fling Effects Captured in the New NGA West2 Ground Motion Models? *Earthquake Spectra* 2014; in press.

[6] Chiou B, Darragh R, Gregor N, Silva W. NGA Project Strong-Motion Database. *Earthquake Spectra* 2008; **24** (1): 23–44.

[7] Alavi B, Krawinkler H. Effects of near-fault ground motions on frame structures 2001; Blume Earthquake Engineering Center Technical Report 138; Stanford, CA.

[8] Kalkan E, Kunnath SK. Effects of Fling Step and Forward Directivity on Seismic Response of Buildings. *Earthquake Spectra* 2006; **22** (2): 367–390.

[9] Calugaru V, Panagiotou M. Response of tall cantilever wall buildings to strong pulse type seismic excitation. *Earthquake Engineering & Structural Dynamics* 2012; **41** (9): 1301–1318.

[10] Stewart JP, Chiou SJ, Bray JD, Graves RW, Somerville PG, Abrahamson NA. Ground Motion Evaluation Procedures for Performance-Based Design 2001; Pacific Earthquake Engineering Research Center Technical Report 2001/09; Berkeley, CA.

[11] Ventura CE, Archila M, Bebamzadeh A, Liam Finn WD. Large coseismic displacements and tall buildings. *The Structural Design of Tall and Special Buildings* 2011; **20**: 85–99.

[12] Makris N. Rigidity–Plasticity–Viscosity: Can Electrorheological Dampers Protect Base-Isolated Structures from Near-Source Ground Motions? *Earthquake Engineering & Structural Dynamics* 1997; **26** (5): 571–591.

[13] Makris N, Roussos YS. Rocking response of rigid blocks under near-source ground motions. *Géotechnique* 2000; **50** (3): 243–262.

[14] Makris N, Black CJ. Dimensional Analysis of Bilinear Oscillators under Pulse-Type Excitations. *Journal of Engineering Mechanics* 2004; **130** (9): 1019–1031.

[15] Makris N, Black CJ. Dimensional Analysis of Rigid-Plastic and Elastoplastic Structures under Pulse-Type Excitations. *Journal of Engineering Mechanics* 2004; **130** (9): 1006–1018.

[16] Lee WHK, Shin TC, Kuo KW, Chen KC, Wu CF. CWB Free-Field Strong-Motion Data from the 921 Chi-Chi Earthquake: Processed Acceleration Files on CD-ROM 2001; Central Weather Bureau; Taipei, Taiwan.

[17] CESMD. Center for Engineering Strong Motion Data [Internet]. *Strong Motion Archive* 2014; Available from: www.strongmotioncenter.org

[18] Burks LS. Ground motion simulations: validation and application for civil engineering problems 2014; Stanford University Ph.D. Thesis; Stanford, CA. http://purl.stanford.edu/rr972yp3813

[19] Abrahamson NR. Velocity Pulses in Near-Fault Ground Motions 2002; In: CUREE Symposium; Berkeley, CA.

[20] Ibarra LF, Krawinkler H. Global collapse of frame structures under seismic excitations 2005; Blume Earthquake Engineering Center Technical Report 152; Stanford, CA.

[21] Lignos D, Krawinkler H, Whittaker AS. Prediction and validation of sidesway collapse of two scale models of a 4-story steel moment frame. *Earthquake Engineering & Structural Dynamics* 2011; **40**: 807–825.

ACCOUNTING FOR TOPOGRAPHIC EFFECTS IN GROUND MOTION PREDICTION EQUATIONS

Manisha Rai and Adrian Rodriguez-Marek

Department of Civil and Environmental Engineering
Virginia Tech, Blacksburg, Virginia

Abstract

This paper reviews results from a recent empirical study on the effects of surface topography on earthquake ground motion. Topography is quantified using: (1) terrain-based parameters that are computed using the elevation data around the station, and (2) Finite difference based parameters that are computed by performing a dynamic analysis on 2D meshes generated from the cross-sectional profiles through the stations. Analysis of residuals from Chiou and Youngs (2014) model show that the terrain based parameter can capture some of the bias in the residuals. Moreover, the two kinds of topographic parameters are found to be correlated.

Introduction

The presence of an irregularity on the earth surface has been known to affect ground motions during an earthquake (Bouchon 1973; Boore et al. 1981; Bard 1982). These effects arise from the interactions between the incident seismic waves and the reflected waves near the surface irregularity. These interaction lead to constructive and destructive interference patterns on the earth surface, causing wave amplifications and de-amplification that may change within small distances (Boore 1972). Typically, ground motions amplify on convex features such as hills and ridges, and de-amplify on concave features such as valleys are canyons (Boore 1972; Davis and West 1973; Spudich et al. 1996). The response on a slope is found to be more complicated ranging from amplifications to de-amplifications (Geli et al. 1988). There are numerous case histories where topographic amplifications are believed to be the source of high recorded peak ground accelerations (Trifunac and Hudson 1971; Celebi 1991; Bouchon and Barker 1996) and, in some cases, the cause of localized damage to buildings (Hartzell et al. 1994; Hatzfeld et al. 1995). The problem of topographic effects has been studied in the past in analytical studies (Bouchon 1973), field studies (Boore 1972; Davis and West 1973; Griffiths and Bollinger 1979; Tucker et al. 1984; Kawase and Aki 1990; Spudich et al. 1996) and in numerical studies (Boore 1972, 1973; Bouchon and Barker 1996; Assimaki and Gazetas 2004; Assimaki et al. 2005; Graizer 2009; Assimaki and Jeong 2013). While these studies have improved our understanding of the effects, we still lack a reliable quantitative tool to predict topographic amplifications in the future.

If topographic effects are systematically observed in ground motions, they should also be predictable. Ideally, ground motion prediction equations (GMPEs) would have a term that accounts for topographic effects. This can only be achieved through a family of parameters that quantify the topography at a site. Previous numerical studies have typically investigated the

effects of site geometry on input ground motions through parametric studies on simple parameters (e.g., slope gradient, slope height and width; Boore 1972; Ashford et al. 1997). Any parameter that affects the ground motion at a site is valid parameter that can be potentially included in a GMPE to model topographic effects. However, a good parameter is one that is able to statistically reduce the bias in the prediction of ground motions. In a recent paper (Rai et al 2014) we looked at some parameters derived from the terrain elevation. We found that two of these parameters (relative elevation and smoothed curvature) can reduce the biases in the predictions in GMPEs. In the current work, we will first briefly review these parameters and their effects on reducing bias in GMPEs and then continue to explore another parameter that is based on the results of the finite difference analysis of 2D models based the geometry at the station. The results from these analyses are only preliminary and further study is currently under progress.

Methodology

The current GMPEs do not account for topographic effects. The residuals from these models are thus expected to carry a systematic bias with respect to topography. To test this, we look at the residual component that reflects repeatable site effects (which are obtained by partitioning the residuals), and evaluate trends in these residuals with respect to topographic parameters at each station. The following sections discuss the partition of residuals and the parameterization of topography.

Residual partitioning

The residuals from a GMPE prediction are split into inter-event and intra-event residuals as shown:

$$\Delta = \delta B_e + \delta W_{es} \quad (1)$$

where Δ is the natural log of the observed spectral acceleration (S_a) minus the natural log of the predicted S_a; δB_e is the event term (or inter-event residual) which is the residual component that is common to all the sites recording that event; and δW_{es} is the intra-event residual which is the residual component at a site after removing δB_e from the total residual. The intra-event residuals can be further partitioned as follows:

$$\delta W_{es} = \delta S2S_s + \delta WS_{es} \quad (2)$$

where $\delta S2S_s$ is the site residual and δWS_{es} is the site and event corrected residual. The site term ($\delta S2S$) can be thought of as the average residual at a site after correcting for the event terms. As topographic effects are site effects, topography related bias is expected to be present in the site residuals ($\delta S2S_s$). All the residual components in Eqs. (1) and (2) are assumed to be independent zero-mean normally distributed variables. A description of these residual components and their variances are given in Table 1.

In this study, we use the intra-event residuals from the Chiou and Youngs (2014) NGA West2 ground motion model to obtain the site terms ($\delta S2S_s$). The Chiou and Youngs (2014) ground motion dataset has recordings from 300 earthquakes of magnitude 3 and higher. The

recordings were made at 3208 ground motion recording stations located across California, Alaska, Japan, Taiwan, China, Turkey, Italy, Iran, and New Zealand. To get a good estimate of $\delta S2S_s$ at each station, only stations that have at least three recording are included in the study. Such a filtering should not introduce any systematic bias with respect to topography in the data, as the elimination criterion is independent of topography.

Table 1: Description of residual components

Residual Component	Description	Standard deviation
δB_e	Inter-event residual	τ
δW_{es}	Intra-event residual	ϕ
$\delta \mathrm{S2S}_s$	Site-to-site residual	ϕ_{s2s}
$\delta \mathrm{WS}_{\mathrm{es}}$	Single- site within-event residual	ϕ_{ss}

This constraint resulted in a total of 9,195 ground motions and 798 stations located in California and Japan (Figure 1). The magnitude-distance distribution of the records in this dataset is shown in Figure 2. The dataset consists of ground motion residuals at 105 spectral periods from 0.01 s to 10 s.

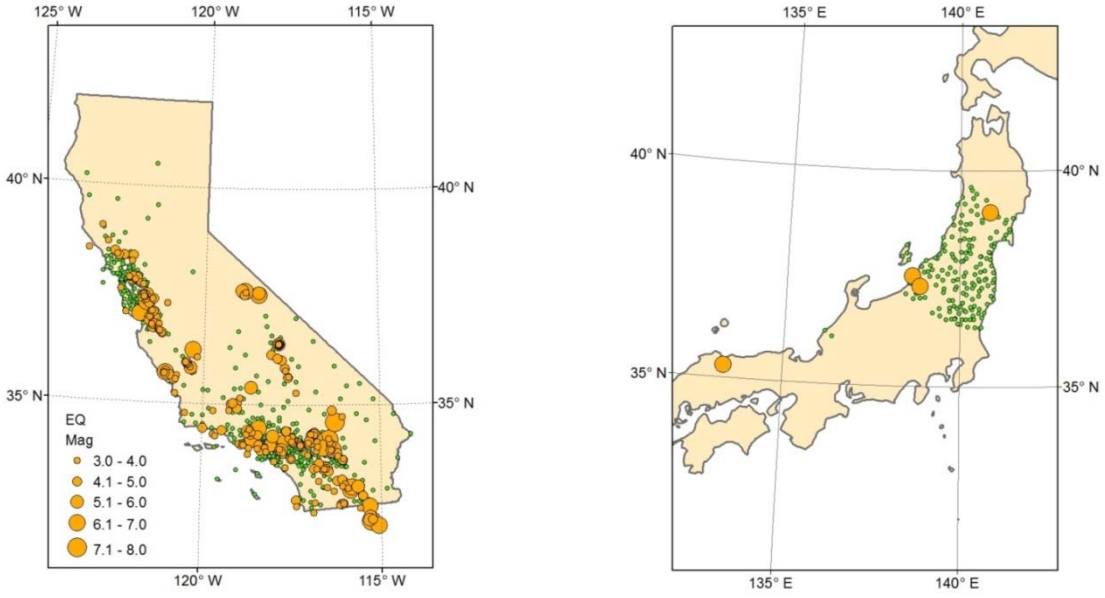

Figure 1: Locations of earthquake hypocenters and recording stations are shown for the ground motions used in the study from California (left) and Japan (right). Only stations with at least 3 recordings are considered. Due to these criteria, only ground motions from California and Japan were selected.

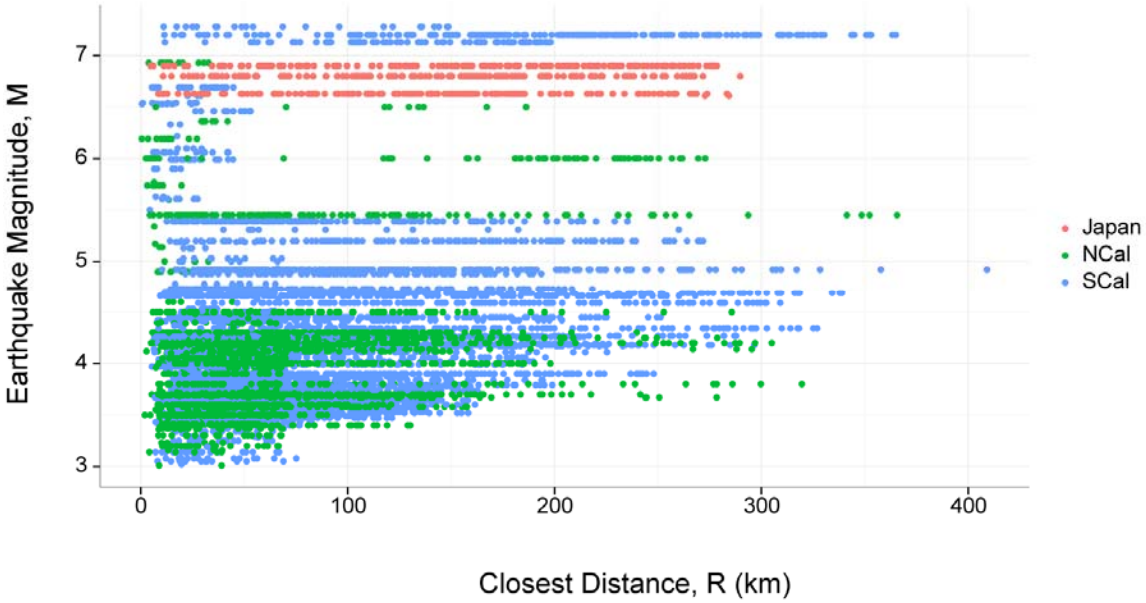

Figure 2: Earthquake magnitudes are plotted with the distance to the recording stations for the ground motions used in the study.

Topographic parameters

In a previous study (Rai et al, 2014), we looked at the topographic parameters that were computed solely using the elevation data around the station. We refer to such parameters as geometry-based parameters. In the current work, we compute another set of topographic parameters that are based on the finite difference analysis. Both these parameters are explained here.

Geometry based parameters

The two geometry based parameters we studied are Relative Elevation and Smoothed Curvature. Both these parameters are computed using the elevation data around the station location. All the computations are done in ArcGIS (ESRI, 2011).

Relative elevation is computed for each cell of the digital elevation model (DEM) by taking the difference of elevation at the cell and the mean elevation of the cells within a neighborhood of the cell. A circular neighborhood is used for computing mean and the diameter of the circle is referred to as the scale parameter. Relative elevation calculated at a scale parameter value of D is referred to as H_D. A positive H_D value means that the elevation of the cell is higher than the mean elevation in the neighborhood; a negative H_D value means that the elevation of the cell is lower than the mean elevation in the neighborhood and a value of zero means that the station is located in a region of uniform slope. For this reason, H_D is effective in highlighting features such as ridges ($H_D > 0$), valleys ($H_D < 0$) and plains/slopes ($H_D = 0$). An example of H_D for D = 500 m, 1000 m and 2000 m is shown in Figure 3.

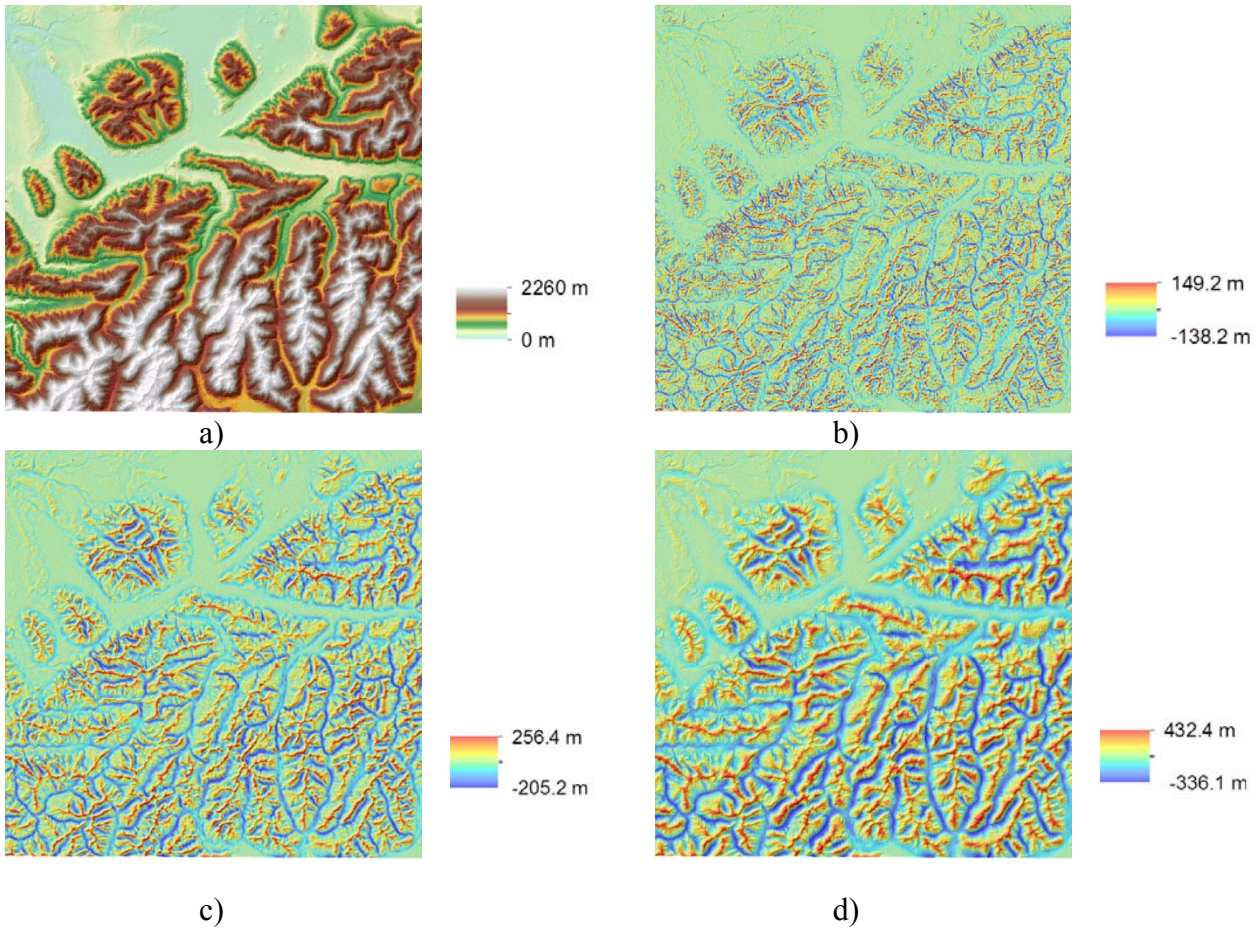

Figure 3: The effect of increasing the scale parameter D on relative elevation is demonstrated. Shown here are a) elevation raster, and relative elevation rasters at a scale of b) 500 m, c) 1000 m, and d) 2000 m. Note that at a scale of 500 m, finer features are visible. As the scale is increased, some of the finer features diminish, and broader features become more prominent.

Smoothed curvature (C) is computed using the curvature tool in ArcGIS. First, the elevation data is smoothed using a certain window size, also referred to as the scale-parameter. This smoothed elevation data is then input into the curvature tool, and the output raster is referred to as the smoothed curvature (C_D). Different scales ranging from 60 m to 600 m were used to study the effects of smoothing on the curvature values.

Finite difference analysis based parameters

The goal of this parameterization scheme is to obtain a set of topographic parameters that are based on the results of numerical analyses conducted using 2D cross-sectional profiles at the station. The output from the analyses will be time-histories at the ground surface. The time history at the location of the station can be used to compute parameters such as the ratio of S_a at the site and S_a at an equivalent site with no topography. Reproducing the exact dynamic response of the site is not a concern as these parameters will be used as independent variables in a prediction exercise where it is advantageous to keep the parameters simple so that they can be

easily computed for any site in the future. For this reason, we only use an elastic soil, with simple soil properties.

For each station in the NGAWest2 dataset, 2D cross-sectional profiles are obtained at azimuths of 0, 30, 60, 90, 120 and 150 degrees from the north, a total of 6 profiles for each station. Multiple sections are used to capture the potential for directional 3D topographic effects. The elevation data for the profile is discretized at 30 m interval to match the approximate 30 m resolution of the DEM. The total length of each profile is 2000 m, and the station is located at the center of each profile (Figure 4). The elevation at the site is subtracted from each of the elevation values in a profile such that in the resulting profile, all the stations are always located at an elevation of 0 m. This step is important because we want to keep all the stations at the same height from the base in the resulting finite different mesh. This will ensure that all the stations have the same 1-D resonant periods, and that we only capture topographic effects in the numerical analysis.

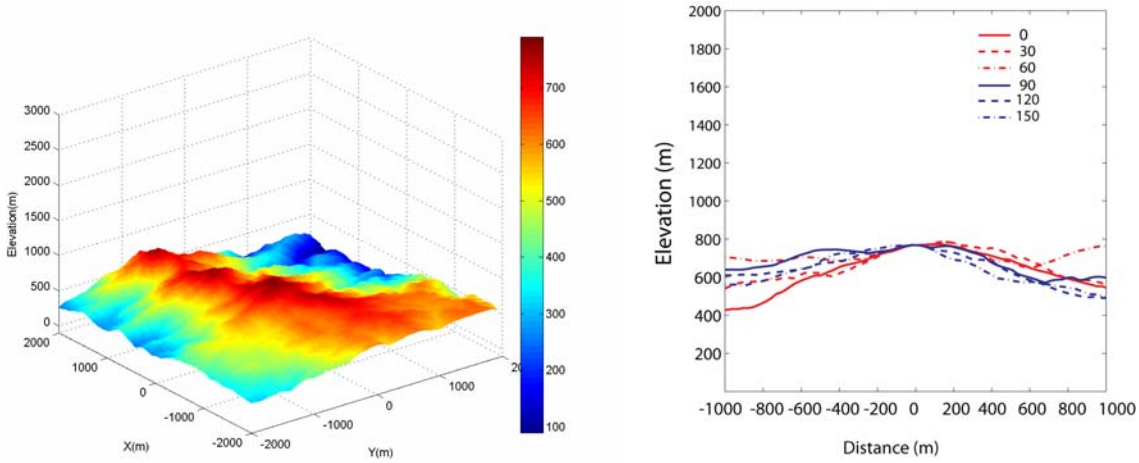

Figure 4: 3D terrain around a site (left) and cross-sectional profiles across the station in 6 different directions (right) are shown. The station is located at x = 0, y = 0.

A 2000 m by 2000 m finite difference mesh is generated in FLAC 5.0 (Itasca Consulting Group, 2005) with a grid size of 25 m in both the x and y directions. The grid is assigned the following soil properties: mass density $\rho = 2$ Mg/m^3, Poisson's ratio $\upsilon = 1/3$, $V_s = 500$ m/s (Bouckovalas and Papadimitriou 2005; Tripe et al. 2013) and a target damping ratio of 5% using Raleigh damping. Once the grid is generated, the top surface of the grid is distorted to fit the shape of the profile. The base of the mesh is treated as infinite and to model it in FLAC, quiet boundaries are applied at the base of each model in both x and y directions. To minimize reflections from the lateral boundaries, free field boundaries are applied to both the lateral boundaries. A schematic illustration of the mesh and the boundary conditions are shown in Figure 5. Note that the resulting depth to the base of the mesh is same for all the stations.

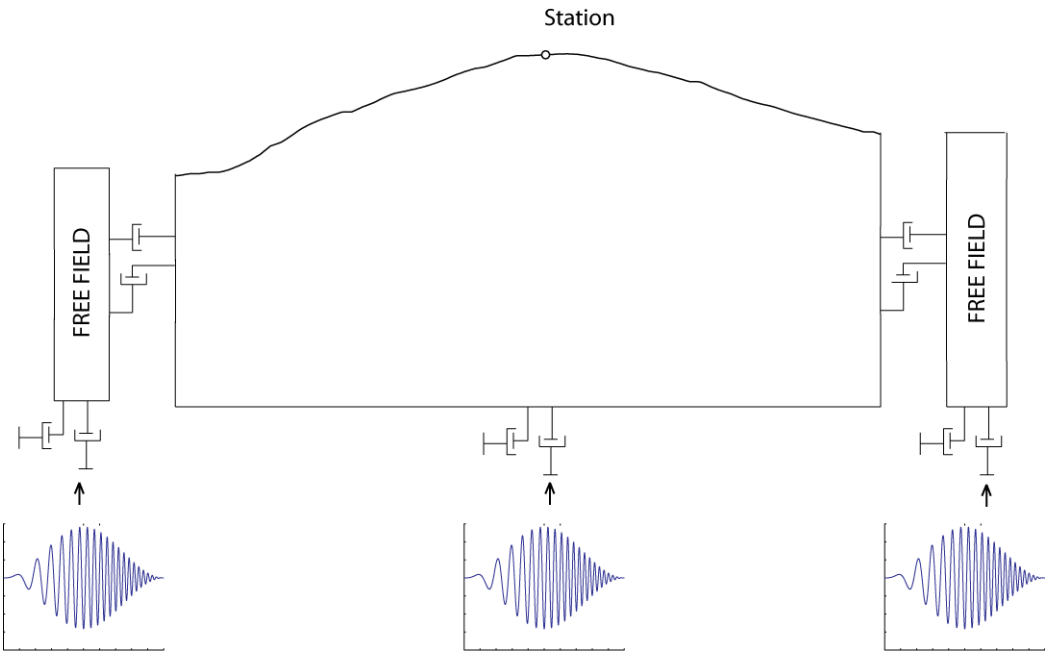

Figure 5: Schematic illustration of the finite difference model used for the analysis at a station. The model uses a realistic topographic cross-section profile at the top. The station is located at the surface, equidistant from both the lateral edges. The height of stations from the base is same for all stations. Free-field boundary condition is applied to the lateral boundaries and quiet boundary conditions are applied at the base.

As the boundaries are quiet, instead of applying accelerations as input, a time history of shear stress is applied (Itasca Consulting Group, 2005). These stresses are a factor of velocity (Itasca Consulting Group, 2005). The input velocity time history used in the study is a tapered sine-sweep wave. The velocity time history is chosen such that the resulting acceleration time history has a PGA of 1 m/s^2 (Figure 6). The input motion consists of frequencies up to 2 Hz .

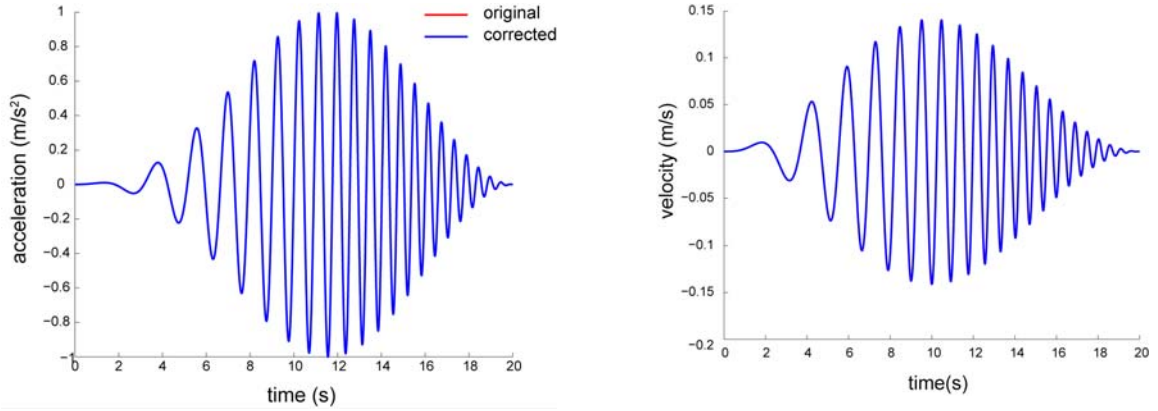

a) b)

Figure 6: Input a) acceleration and b) velocity time histories for the original and base line corrected motion.

The 2 Hz frequency limit is chosen to restrict the number of zones in the mesh (and consequently the computational time) as the maximum mesh dimension is inversely proportional to the highest frequency to be modelled correctly. The total duration of the input motion is 20 s. Output time histories are recorded at each of the grid points on the top surface of the mesh. A similar analysis is conducted using a flat surface at the top (1D analysis), and the results from the 1D analysis (the free field response) is used to normalize the response obtained from the 2D analyses.

Spectral accelerations are computed using the output time histories at the location of the station (x = 0, y = 0) for each of the 6 orientations. These S_a values are normalized with S_a values from the 1D case. The log of minimum, maximum, and average values of the normalized S_a from the 6 orientations are the topographic parameters for the station. We refer to these parameters as Spectral Amplification Ratio (SAR_{min}, SAR_{max}, SAR_{avg}). The relationship between SAR (T = 0.5 s) for all the 6 orientations and H_{1500} for the stations in the dataset is shown in Figure 7.

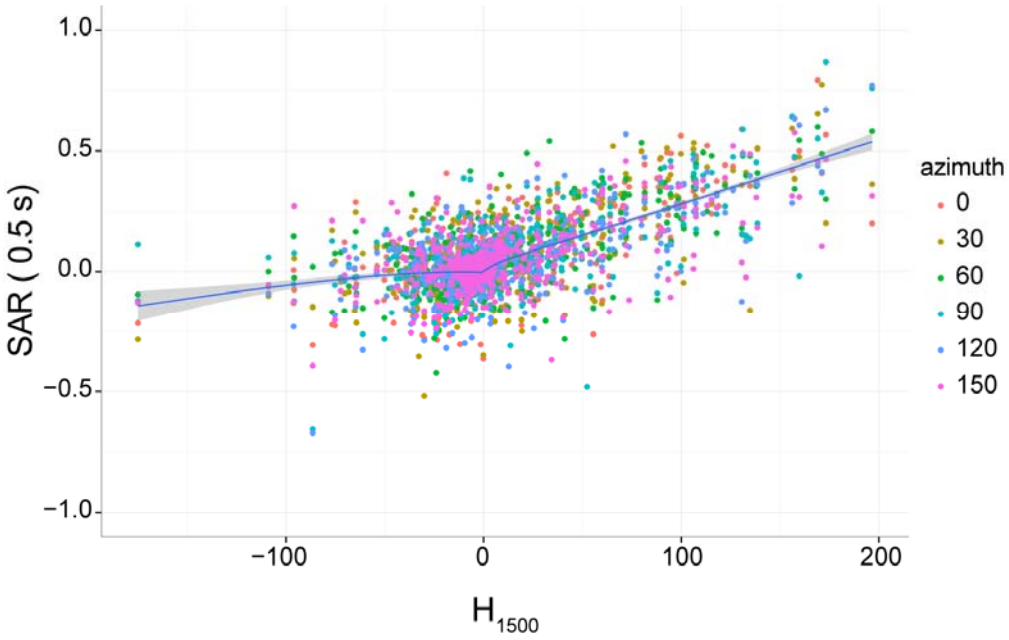

Figure 7: SAR values for T = 0.5 s are plotted with H_{1500} for the stations in the NGAWest2 dataset. A moving average of the SAR terms computed using local regression (loess) is also shown. A high degree of linear correlation is observed between the two parameters.

There is a high linear correlation between the two parameters. At other periods, similar relationship is observed between the two parameters. This is an interesting finding in two ways: first, it validates the usefulness of the H_{1500} parameter to predict topographic effects; second, this might probably imply that a complicated numerical analysis may not necessarily be required to make predictions about topographic effects in future earthquakes. A simple parameter based on elevation data might just be sufficient to estimate the effects.

Results

The site residuals are compared with the topographic parameters obtained in the previous steps. Here we review some of the results from the residual analysis using the geometry based parameters. We will also present some preliminary results from the finite difference analysis.

Geometry based parameters

The site residuals computed using the intra-event residuals (Equation 2) from the Chiou et al. (2014) model are plotted with H_{1500} (Figure 8). The mean site residuals (average of the site residuals for sites in a topographic class) for the three topographic classes are also shown. A threshold of 20 m is used for classification. Mean site residuals at other periods are also shown (Figure 9).

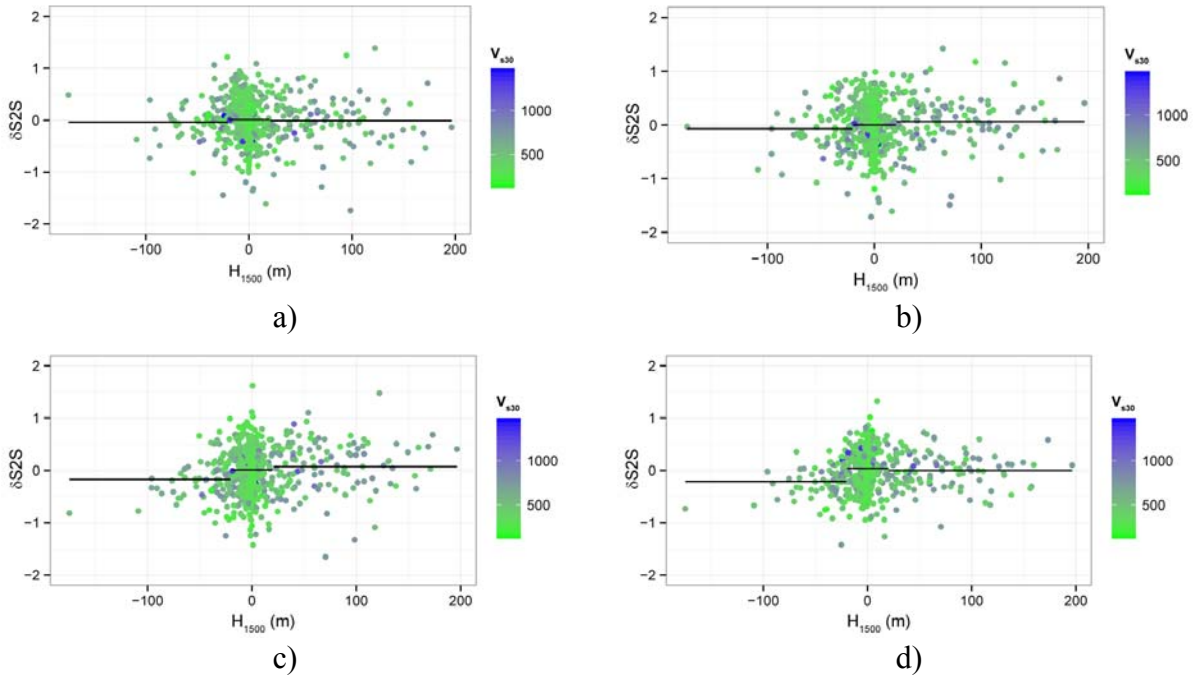

Figure 8: Site residuals ($\delta S2S_s$) are plotted with H_{1500}. The mean site residuals for the three classes: high, intermediate and low are shown with horizontal lines. The plots are shown for periods of a) T = 0.01 s, b) T = 0.3 s, c) T = 1 s, d) T = 3 s.

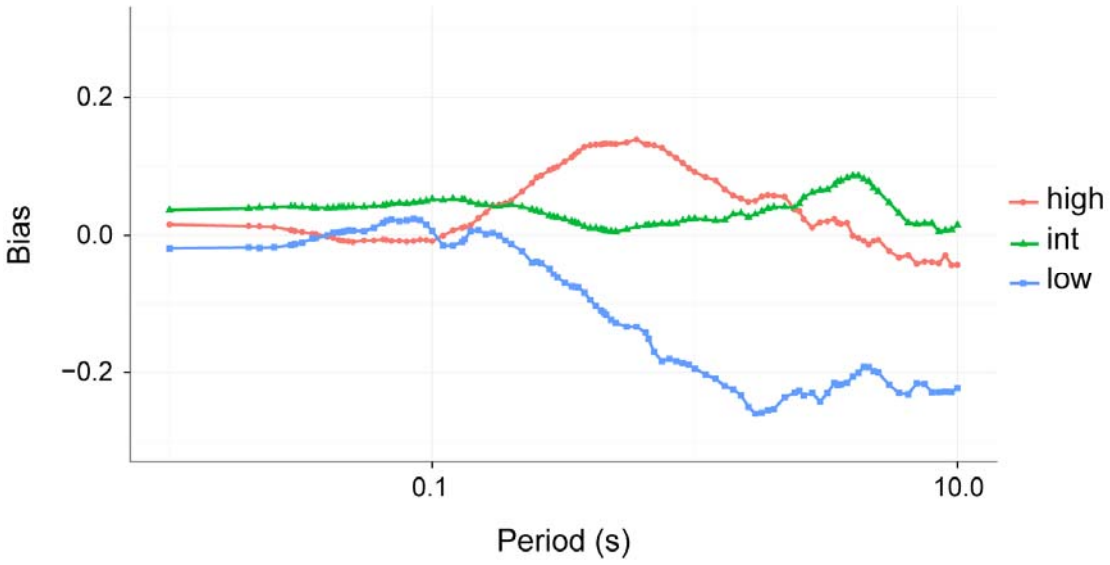

Figure 9: Mean site residual for high, low and intermediate sites are shown at different periods. A scale of 1500 m and a threshold of 20 m were used for the classification.

Analysis of variance (ANOVA) is used to test the statistical significance of differences in the mean site residuals for the three topographic classes. A pair-wise t-test is also performed to test the significance of the difference in mean residual between different pairs of class. A statistical significance is assumed at 95% or for p-values less than 0.05 (i.e., the probability that the differences are due to random chance is less than 5 %). The p-values from ANOVA are below 0.05 levels for periods between 0.32 s and 10 s. The pairwise Tukey's t-tests show that the difference of mean site residual for intermediate and high lying stations is significant only between periods of 0.38 s to 0.75 s, the difference between low lying and high lying stations are statistically significant for periods greater than 0.30 s, and the difference between low and intermediate stations are significant for periods greater than 0.50 s. The analysis showed that the parameter was able to capture the bias in the residuals and that it is possible to come up with parameters that can be included in the GMPE to reduce biases.

Finite difference based parameter

The site residuals computed above are plotted with SAR_{avg} at the same period (Figure 10). To check for bias in residuals with respect to SAR_{avg} values, stations were divided into three classes based on the SAR_{avg} value at the station. A threshold of 0.5σ is used for classification such that station with $SAR_{avg} > 0.5\sigma$ are classified as high, $SAR_{avg} < -0.5\sigma$ are classified as low and the stations with SAR_{avg} in between -0.5 σ and 0.5 σ are classified as intermediate, where σ denotes the standard deviation of the SAR_{avg} values. The plot shows a bias in the residuals with respect to the parameter but the trends are less pronounced than those observed in the case of relative elevation parameter. These results are preliminary and additional research is being done to test the significance of the differences observed. Also, various other finite difference based parameters are currently being studied.

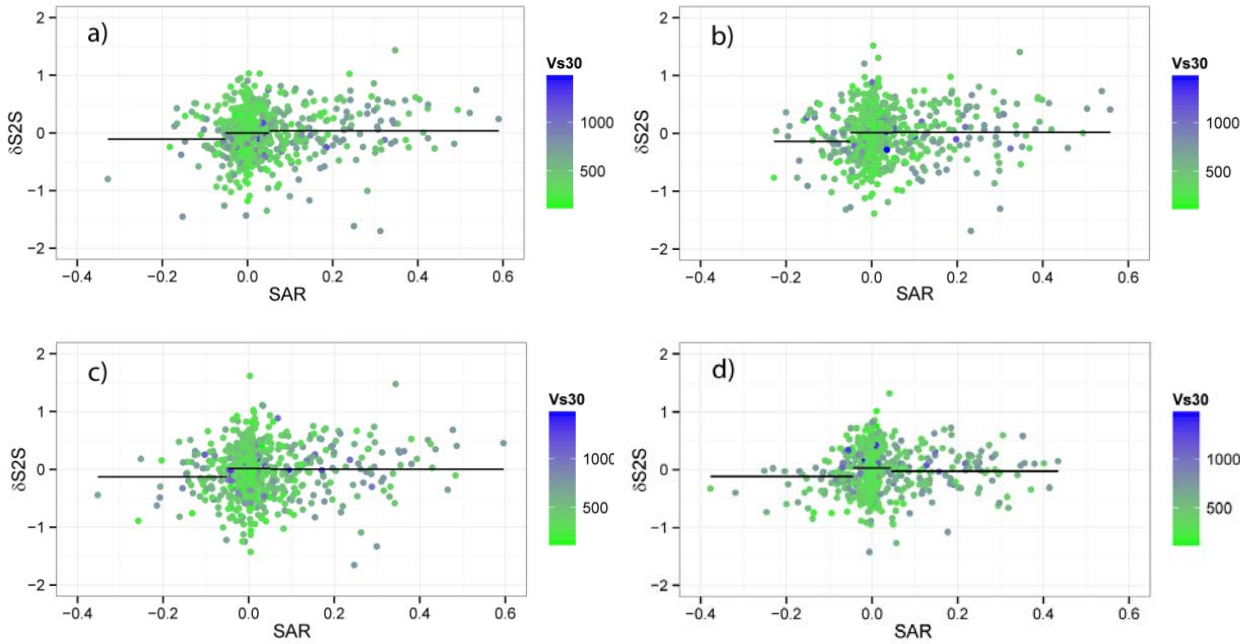

Figure 10: Site residuals ($\delta S2S_s$) are plotted with SAR_{avg} at the same period. The plots are shown for periods of a) T = 0.5 s, b) T = 0.8 s, c) T = 1 s, d) T = 3 s. Plots for periods less than 0.5 s are not shown due to expected numerical distortion of higher frequencies.

Conclusions

The effects of surface topography on earthquake ground motion were studied using the residuals from Chiou and Young (2014) NGAWest2 datasets. The trends in ground motion residuals were evaluated with respect to topographic parameters. Two kinds of topographic parameters were studies; terrain based and finite difference based. Terrain based parameters were computed using the elevation data at the station. Finite difference based parameters were computed using the output time histories at the station from dynamic analyses using finite differences. The analyses were conducted using meshes that were deformed at the surface to fit the shape of the cross-sectional profile at the station and subjecting the mesh to a tapered sine-sweep input motion. For each station, cross-sectional profiles in 6 different directions were used.

We found that the terrain based parameters were able to predict some of the trends in the ground motion residuals and they can potentially reduce biases in GMPEs. We also found a high linear correlation between the terrain based parameter and the finite difference based parameter. This finding validates the usefulness of the terrain based parameter, which might not be an intuitive parameter at first. This also shows that a numerical analysis will not necessarily be required to make predictions about ground motions in future earthquakes. It is important to note that this is a work under progress and that some results are only preliminary.

References

Ashford, S. A., Sitar, N., Lysmer, J., and Deng, N. (1997). "Topographic effects on the seismic response of steep slopes." *Bulletin of the Seismological Society of America*, 87(3), 701–709.

Assimaki, D., and Gazetas, G. (2004). "Soil and topographic amplification on canyon banks and the 1999 Athens earthquake." *Journal of earthquake engineering*, 8(01), 1–43.

Assimaki, D., and Jeong, S. (2013). "Ground-Motion Observations at Hotel Montana during the M 7.0 2010 Haiti Earthquake: Topography or Soil Amplification?" *Bulletin of the Seismological Society of America*, 103(5), 2577–2590.

Assimaki, D., Kausel, E., and Gazetas, G. (2005). "Soil-Dependent Topographic Effects: A Case Study from the 1999 Athens Earthquake." *Earthquake Spectra*, 21(4), 929–966.

Bard, P.-Y. (1982). "Diffracted waves and displacement field over two-dimensional elevated topographies." *Geophysical Journal International*, 71(3), 731–760.

Boore, D. M. (1972). "A note on the effect of simple topography on seismic SH waves." *Bulletin of the Seismological Society of America*, 62(1), 275–284.

Boore, D. M. (1973). "The effect of simple topography on seismic waves: implications for the accelerations recorded at Pacoima Dam, San Fernando Valley, California." *Bulletin of the Seismological Society of America*, 63(5), 1603–1609.

Boore, D. M., Harmsen, S. C., and Harding, S. T. (1981). "Wave scattering from a step change in surface topography." *Bulletin of the Seismological Society of America*, 71(1), 117–125.

Bouchon, M. (1973). "Effect of topography on surface motion." *Bulletin of the Seismological Society of America*, 63(2), 615–632.

Bouchon, M., and Barker, J. S. (1996). "Seismic response of a hill: the example of Tarzana, California." *Bulletin of the Seismological Society of America*, 86(1A), 66–72.

Bouckovalas, G. D., and Papadimitriou, A. G. (2005). "Numerical evaluation of slope topography effects on seismic ground motion." *Soil Dynamics and Earthquake Engineering*, 25(7-10), 547–558.

Celebi, M. (1991). "Topographical and geological amplification: case studies and engineering implications." *Structural Safety*, 10(1), 199–217.

Chiou, B. S.-J., and Youngs, R. R. (2014). "Update of the Chiou and Youngs NGA Model for the Average Horizontal Component of Peak Ground Motion and Response Spectra." *Earthquake Spectra In-Press*.

Davis, L. L., and West, L. R. (1973). "Observed effects of topography on ground motion." Bulletin of the Seismological Society of America, 63(1), 283–298.

ESRI (2011). "ArcGIS Desktop: Release 10." Redlands, CA.

Geli, L., Bard, P.-Y., and Jullien, B. (1988). "The effect of topography on earthquake ground motion: a review and new results." *Bulletin of the Seismological Society of America*, 78(1), 42–63.

Graizer, V. (2009). "Low-velocity zone and topography as a source of site amplification effect on Tarzana hill, California." *Soil Dynamics and Earthquake Engineering*, 29(2), 324–332.

Griffiths, D. W., and Bollinger, G. A. (1979). "The effect of Appalachian Mountain topography on seismic waves." *Bulletin of the Seismological Society of America*, 69(4), 1081–1105.

Hartzell, S. H., Carver, D. L., and King, K. W. (1994). "Initial investigation of site and topographic effects at Robinwood Ridge, California." *Bulletin of the Seismological Society of America*, 84(5), 1336–1349.

Hatzfeld, D., Nord, J., Paul, A., Guiguet, R., Briole, P., Ruegg, J.-C., Cattin, R., Armijo, R., Meyer, B., Hubert, A., Bernard, P., Makropoulos, K., Karakostas, V., Papaioannou, C., Papanastassiou, D., and Veis, G. (1995). "The Kozani-Grevena (Greece) Earthquake of May 13, 1995, Ms = 6.6. Preliminary Results of a Field Multidisciplinary Survey." *Seismological Research Letters*, 66(6), 61–70.

Itasca Consulting Group, Inc. (2005). "FLAC: fast lagrangian analysis of continua". User's manual.

Kawase, H., and Aki, K. (1990). "Topography effect at the critical SV-wave incidence: possible explanation of damage pattern by the Whittier Narrows, California, earthquake of 1 October 1987." *Bulletin of the Seismological Society of America*, 80(1), 1–22.

Rai, M., Rodriguez-Marek, A., and Yong, A. (2014). "An empirical model to predict topographic effects in strong ground motion: Study using the California small to medium magnitude earthquake database." To be submitted to Earthquake Spectra.

Spudich, P., Hellweg, M., and Lee, W. H. K. (1996). "Directional topographic site response at Tarzana observed in aftershocks of the 1994 Northridge, California, earthquake: implications for mainshock motions." *Bulletin of the Seismological Society of America*, 86(1B), S193–S208.

Trifunac, M. D., and Hudson, D. E. (1971). "Analysis of the Pacoima dam accelerogram—San Fernando, California, earthquake of 1971." *Bulletin of the Seismological Society of America, 61(5), 1393–1411.*

Tripe, R., Kontoe, S., and Wong, T. K. C. (2013). "Slope topography effects on ground motion in the presence of deep soil layers." *Soil Dynamics and Earthquake Engineering*, 50, 72–84.

Tucker, B. E., King, J. L., Hatzfeld, D., and Nersesov, I. L. (1984). "Observations of hard-rock site effects." *Bulletin of the Seismological Society of America*, 74(1), 121–136.

STUDYING DIRECTION OF LOADING PROVISIONS IN MODERN CODES: RESEARCH MOTIVATION AND LITERATURE REVIEW

Reid B. Zimmerman, P.E.
Bret Lizundia, S.E.
Saeed Fathali, Ph.D., P.E.

Rutherford + Chekene
Structural and Geotechnical Engineers
San Francisco, CA

Abstract

Direction of loading procedures intend to address the occurrence of earthquake shaking along two principal axes of a building simultaneously. Direction of loading provisions in several modern codes are reviewed, and a comprehensive literature review on the topic is presented. Research to date on direction of loading, based on both linear and nonlinear analysis, indicates potential underestimation of building seismic response. The motivation for an approach to assessing the direction of loading provisions in ASCE/SEI 7-10 using instrumented building data is outlined. Results of this approach will be reported in future publications.

Introduction

Direction of loading is known by many names between different codes, guidelines and published research. In addition to "direction of loading," it is sometimes referred to as orthogonal combination, directional combination, multidirectional effects, or concurrent effects. Regardless, the intent of its consideration is consistent throughout: To capture the occurrence of earthquake shaking along two or more axes of a building simultaneously. Although simplified design procedures often separate seismic shaking into two (or more) demands determined independently for each axis, it is known that earthquake ground motions induce simultaneous acceleration in all six degrees of freedom. Direction of loading provisions in modern codes attempt to approximate this reality through some combination of the demands determined independently for each axis.

The two most common orthogonal combination rules are the 100%+XX% rule and the square-root-sum-of-the-squares (SRSS) rule. The 100%+XX% rule is considerably more often used in modern codes than the SRSS rule and will therefore be the primary focus in this paper. Quantitative descriptions of both the 100%+XX% rule and the SRSS rule can be found in Equations 1 and 2, respectively. Note that when the SRSS and 100%+XX% rules are applied in design, it may be necessary to apply load factors on the individual responses before combination. Load factors can be found in modern codes (e.g. ASCE/SEI 7, ASCE/SEI 41). Some of the notation in Equations 1 and 2 is based on Rosenblueth and Contreras (1977).

$$R_{100\%+XX\%} = R_0 + max\begin{cases} R_1 + \alpha \sum_{i \neq 1} R_i \\ R_2 + \alpha \sum_{i \neq 2} R_i \\ \cdots \\ R_n + \alpha \sum_{i \neq n} R_i \end{cases} \qquad \text{Equation 1}$$

$$R_{SRSS} = R_0 + \sqrt{\sum_{i=1}^{n} R_i^2} \qquad \text{Equation 2}$$

where

$R_i =$ maximum value of the response quantity of interest (e.g., strong axis moment in a column) due to earthquake shaking in degree of freedom *i*

$R_0 =$ maximum value of the response quantity of interest due to non-seismic loads

$n =$ total number of degrees of freedom considered, less than or equal to 6

$\alpha =$ orthogonal combination factor for 100%+XX% rule that varies from 0 to 1 inclusive

In the further simplified form most often seen in modern codes, the 100%+XX% rule is reduced to only the two horizontal translational components of ground shaking and α is taken as 0.3. This is then referred to as the 100%+30% rule. When linear analysis is conducted (i.e., response quantities of interest are linearly related to the applied forces), the 100%+30% rule can be described by two load cases:

1. 100% of the seismic forces in the x-direction and 30% of the seismic forces in the y-direction
2. 100% of the seismic forces in the y-direction and 30% of the seismic forces in the x-direction

The x-direction and the y-direction must be orthogonal and are typically selected as the principal axes of the structure. Note that all combinations of positive and negative values must be considered in the above two load cases, thus expanding them to a total of eight. Further discussion on these cases is provided below under "Characterization of the ASCE/SEI 7-10 Provisions."

It is important to distinguish between directional combination rules and modal combination rules. Confusion concerning the difference between directional combination and modal combination as they appear in modern codes and especially computer software is not uncommon. This is partially owing to the fact that some rules, such as the SRSS procedure, can be applied for both modal and directional combination. Yet directional and modal combination procedures attempt to capture distinctly different phenomena. Modal combination rules approximately account for the total response of a structure due to ground shaking in one degree of freedom (e.g., translation along one horizontal axis) by combining in some way the response due to each mode. Typical modal combination rules include SRSS and Complete Quadratic Combination (CQC) (Menun and Der Kiureghian, 1998). Directional combination rules, on the other hand, are focused on capturing the total response of a structure due to ground shaking in multiple degrees of freedom (e.g., translation about two horizontal, orthogonal axes) by combining in some way the response due to ground shaking in each degree of freedom. Directional combination rules in modern codes, and their adequacy, are the focus of this paper.

Summary of Provisions in Modern Codes

Although many modern codes have adopted a form of the 100%+XX% orthogonal combination rules to approximate concurrent seismic effects, differences do exist in how they are applied and when they are required. This section summarizes direction of loading provisions in four current, nationally recognized codes and standards for seismic design or rehabilitation: ASCE/SEI 7-10 *Minimum Design Loads for Buildings and Other Structures* pertains to new building design; ASCE/SEI 41-13 *Seismic Evaluation and Retrofit of Existing Buildings* pertains to existing buildings; AASHTO *Guide Specifications for LRFD Seismic Bridge Design, 2nd Edition* pertains to new bridge design; and FHWA-HRT-06-032 *Seismic Retrofitting Manual for Highway Structures, Part 1 - Bridges* pertains to existing bridges.

ASCE/SEI 7-10 Provisions

ASCE/SEI 7-10 Section 12.5 contains the current provisions concerning direction of loading which are slightly different for each Seismic Design Category. Seismic Design Categories range from A to F in order of increasing earthquake demand and structural importance with Seismic Design Category A being exempt from ASCE/SEI 7 Chapter 12. For Seismic Design Category B, ASCE/SEI 7 only requires the seismic forces to be applied independently in each of two orthogonal directions and allows orthogonal interaction effects to be neglected. This essentially means that directional combination is not required for Seismic Design Category B. Neglecting directional combination in Seismic Design Category B stems from the fact that seismic forces rarely govern in this category.

Seismic Design Category C structures with lateral force-resisting systems which are not orthogonal must meet more stringent provisions than for Seismic Design Category B. If the equivalent lateral force or modal response spectrum procedures are used, ASCE/SEI 7 requires that the structural "members and their foundations [be] designed for 100 percent of the forces in one direction plus 30 percent of the forces for the perpendicular direction." This is the 100%+30% rule and is attributed to Rosenblueth and Contreras (1977) in the ASCE/SEI 7 commentary. If linear or nonlinear response history analysis is used in the structure's design, ASCE/SEI 7 instead requires that orthogonal pairs of ground motion records be applied simultaneously. It is also permissible to use the 100% + 30% rule with linear response history analysis. ASCE/SEI 7 Chapter 16 contains further guidance on response history analysis.

Seismic Design Category D through F buildings with either non-orthogonal lateral force-resisting systems or shared structural elements, such as corner columns, where the seismic axial demand exceeds 20% of the design strength are required to be "designed for the most critical load effect due to application of seismic forces in any direction." ASCE/SEI 7 further stipulates that this requirement can be met by using either the 100% + 30% combination rule for equivalent lateral force or modal response spectrum analysis, or simultaneous application of ground motion pairs for response history analysis. One could theoretically meet the provisions, however, by analyzing the building under all possible angles of seismic incidence and without using the orthogonal combination rule. This is achievable through application of the lateral forces at each angle with respect to the building axes for the equivalent lateral force or modal response

spectrum procedures. Researchers studying the direction of loading provisions have also sometimes rotated ground motions in nonlinear response history analysis over all seismic incidence angles (MacRae and Mattheis, 2000; MacRae and Tagawa, 2001; Bisadi and Head 2011). The application of earthquake shaking at multiple angles with respect to the building in order to satisfy the direction of loading provisions is rarely, if ever, pursued in professional practice.

ASCE/SEI 41-13 Provisions

Provisions for multidirectional seismic effects appear in Section 7.2.5 of ASCE/SEI 41-13. In contrast with ASCE/SEI 7, ASCE/SEI 41 does not distinguish its direction of loading provisions by Seismic Design Category. It therefore only has one set of "triggers" for consideration of direction of loading. Buildings which have an irregularity either described by a discontinuous lateral force-resisting system (due to a shift either in-plane or out-of-plane from story to story), a lateral force-resisting system with a weak story, or a lateral force-resisting system with a torsional strength imbalance must be assessed per ASCE/SEI 41's multidirectional seismic effects provisions. Additionally, buildings that have one or more columns that form part of two or more intersecting frames must consider concurrent seismic effects.

Consideration of direction of loading, similar to ASCE/SEI 7, is dependent on the analysis procedure. When the linear static or linear dynamic procedures are selected, ASCE/SEI 41 permits the use of the 100%+30% combination rule to satisfy the requirement for considering concurrent seismic effects. This is consistent with provisions in ASCE/SEI 7. When the nonlinear static procedure is selected, ASCE/SEI 41 permits the use of the 100%+30% combination rule but clarifies that the 30% need only be the "forces (not deformations) associated with 30% of the displacements". This establishes consistency with the linear static and linear dynamic procedures which reduce the elastic forces by an *m*-factor to account for ductility and then take 30%. In the nonlinear static procedure, the inelasticity is modeled explicitly and thus directly reduces the elastic forces (i.e. no m-factor is required). The 30% is then taken on those reduced forces. Alternatively, ASCE/SEI 41 permits a nonlinear static analysis of the structure with "100% of the displacements in any single direction that generates maximum deformation and component demands" in place of the 100%+30% rule. The commentary clarifies that for the example of a corner column in a square, regular building, a nonlinear static analysis at a 45 degree angle with respect to the building's principal axes could be pursued.

In addition to the 100%+30% orthogonal combination rule, ASCE/SEI 41 includes language for the linear static, linear dynamic and nonlinear static procedures that states "other combination rules shall also be permitted where verified by experiment or analysis." This provides the engineer with an alternative path to demonstrate compliance with the intent of the concurrent seismic effects provisions. Finally, when the nonlinear dynamic procedure is performed on a 3-dimensional model, ASCE/SEI 41 simply requires that both components of ground acceleration be applied simultaneously.

AASHTO Guide Specifications for LRFD Seismic Bridge Design Provisions

The 2nd edition of the *AASHTO Guide Specifications for LRFD Seismic Bridge Design* addresses the combination of orthogonal seismic displacement demands in Article 4.4. Similar to ASCE/SEI 7 and ASCE/SEI 41, the AASHTO Guide Specifications adopt the 100%+30% orthogonal combination rule. It is, however, applied slightly differently than in ASCE/SEI 7 and ASCE/SEI 41. Because the AASHTO Guide Specifications utilizes a displacement-based, rather than a force-based, design procedure, the 100%+30% rule is applied to displacements rather than forces. ASCE/SEI 41's nonlinear static procedure is similarly a displacement-based procedure. Unlike ASCE/SEI 41's nonlinear static procedure, though, the AASHTO Guide Specifications do not take 30% of the force demands but instead use 30% of the displacement demands. For a highly ductile system, 30% of the displacements could be 100% rather than 30% of the forces in individual structural members.

The AASHTO Guide Specifications does state that for design procedures that require the development of elastic seismic forces "the procedure for development of such forces is the same as that for displacements". Therefore, when a structural member action is required to remain elastic, and is not otherwise controlled by capacity-design requirements, only 100%+30% of the forces need be used. These structural members are therefore designed similarly to the procedures in ASCE/SEI 7 and ASCE/SEI 41.

FHWA-HRT-06-032 Provisions

The provisions for combination of seismic force effects occur in Section 7.4.2 of FHWA-HRT-06-032. It provides two alternatives to demonstrating compliance, the first being the square-root-sum-of-the-squares (SRSS) rule and the second being the 100%+40% rule. The 100%+40% rule is similar to the 100%+30% rule in ASCE/SEI 7 except that the 30% component is increased to 40%. The SRSS rule combines a response quantity of interest (e.g. moment about the strong axis of a column) in a different way than the 100%+XX% rules. In the example of column strong axis moment demand, defined as M_u, instead of taking 100% of M_u due to x-direction shaking and 30% of M_u due to y-direction shaking, the SRSS rule takes the square root of the sum of 100% of M_u due to x-direction shaking and 100% of M_u due to y-direction shaking. In contrast with ASCE/SEI 7, ASCE/SEI 41 and the AASHTO Guide Specifications, FHWA-HRT-06-032 also provides guidance on combination rules for when vertical seismic forces are considered. In the other documents, vertical seismic forces are considered through load combinations.

Literature Review and Background

Brief History of Procedures

Development of orthogonal combination rules for multi-component ground motions was first attempted by O'Hara and Cunnif (1963) while Chu et al. (1972) proposed the use of the SRSS procedure. A class of orthogonal combination procedures known as the 100%+XX% rules first appeared when Newmark (1975) suggested that 100% of response in one direction plus 40% in the other could conservatively capture bidirectional loading. Rosenblueth and Contreras

(1977), based on earlier work by A.S. Velestos and Newmark, proposed the 100% + 30% rule which has gained widespread use in modern codes. More recently, Menun and Der Kiureghian (1998) extended the well-known CQC modal combination rule to a modal and directional combination rule named CQC3 (Complete Quadratic Combination with three components). They also noted that both the SRSS and the percentage rules were simplified or special cases of the CQC3 rule. Hernandez and Lopez (2002) further developed the CQC3 method into the GCQC3 (Generalized Complete Quadratic Combination with three components). While analytically investigating other directional combination procedures, Fernandez-Davila et al. (2000) implemented a method which takes 120% of the demand from a unidirectional analysis and applies it in the most unfavorable direction for each element. Note that all the preceding rules were derived based on linear-elastic theory and often made assumptions about ground motion characteristics. Research since the development of the CQC3 and GCQC3 rules has therefore tended to focus on analysis of linear and nonlinear models under single and multi-component ground motions in assessing the suitability of directional combination procedures. For example, a nonlinear study by Zaghlool et al. (2001) motivated the proposal for a 100% + 45% combination rule while Cimellaro et al. (2014) recommend a 100%+60% combination rule for nonlinear static analysis.

Derivation of the 100%+30% Rule

As the most common orthogonal combination rule in modern codes, the 100%+30% rule is used in the design of most structures today. A derivation of the 100%+30% rule first appeared in Rosenblueth and Contreras (1977), an abbreviated form of which is included here for the case of considering only the two horizontal, translational components of ground shaking. For the complete derivation refer to Rosenblueth and Contreras (1977). Begin by first making several assumptions:

1. Linear behavior of the structure.
2. No non-seismic loads. This can be equivalently stated as $R_0 = 0$ (See Equation 1 for notation).
3. Equal earthquake spectra for both horizontal components and a doubly symmetric structure. This can be equivalently stated as $R = R_1 = R_2$ (See Equation 1 for notation).
4. Responses to earthquake spectra for each horizontal component are not correlated with each other. This permits the use of the SRSS rule to combine responses.
5. The structure has equal capacity along any axis (e.g., a structure composed of one cantilever, round column). This can be equivalently stated as the failure surface is circular.

Then consider two cases representing the maximum error on the safe and unsafe side, respectively, for the 100%+XX% rule. For each case, set the structure's capacity equal to the response predicted by the 100%+XX% rule. The demand is taken as the response due to simultaneous application of earthquake shaking in both directions. The error is defined as the capacity minus the demand divided by the demand.

1. Maximum error on the safe side occurs when the responses due to the ground motion components are perpendicular to each other. Because the responses are perpendicular, the maximum demand has magnitude equal to R. However, Equation 1 requires that

R_1 and αR_2 (and also R_2 and αR_1) be considered simultaneous and therefore the capacity is the vector sum with magnitude equal to $R\sqrt{1+\alpha^2}$.

2. Maximum error on the unsafe side occurs when the responses due to the ground motion components are collinear to each other. The maximum demand is then computed as the SRSS of the responses for each direction. It therefore has a magnitude equal to $R\sqrt{2}$. However, Equation 1 requires that R_1 and αR_2 (and also R_2 and αR_1) be considered simultaneous and therefore the capacity is the vector sum with magnitude equal to $R(1+\alpha)$.

Table 1 summarizes the calculations for the safe side and unsafe side cases as described above. The error is also shown in the far right column. The absolute value of the maximum errors on the safe and unsafe side are equated and α is computed. This results in α = 0.336 and maximum safe and unsafe errors of 5.5%. In Rosenblueth and Contreras (1977), α was then taken as a rounded value of 0.3.

Table 1. Safe and unsafe side cases for derivation of the 100%+30% rule

Case	Demand	Capacity	Error
Safe Side	R	$R\sqrt{1+\alpha^2}$	$\sqrt{1+\alpha^2}-1$
Unsafe Side	$R\sqrt{2}$	$R(1+\alpha)$	$\dfrac{1+\alpha-\sqrt{2}}{\sqrt{2}}$

An applied engineering analogy for the two cases considered in the derivation by Rosenblueth and Contreras (1977), as described above, is now made. For the case of maximum error on the safe side, consider the roof displacement of a square, one-story building. First calculate the roof displacement response due to simultaneous shaking in both horizontal directions. As stated in the assumptions for the safe side case of the Rosenblueth and Contreras derivation, shaking in the x-direction only produces roof displacement in the x-direction and vice versa for the y-direction. As a hypothetical example, the roof x-direction and y-direction displacements could each be equal to 2 inches. Now consider the simultaneous application of x-direction and y-direction shaking. Another assumption made is that the responses due to each direction are not correlated. This can be thought of more practically as that the maximum responses in each direction do not occur simultaneously. Therefore, the 2 inch roof displacement in the x-direction and 2 inch roof displacement in the y-direction will not occur at the same time even when both components of shaking are applied simultaneously. The roof displacement demand can then be considered as 2 inches in the x-direction or 2 inches in the y-direction but not both at the same time. However, the structure's capacity has been determined by the 100%+30% rule. The 100%+30% rule does not recognize that the x-direction and y-direction roof displacements occur at different points in time but instead requires that the structure be designed for the effects of 100% of the maximum response in one direction and 30% of the maximum response in the other concurrently. The vector roof displacement would then be, for the hypothetical numbers described previously, $\sqrt{(2\ inches)^2+(0.3*2\ inches)^2} \cong 2.1\ inches$. Both the demand and capacity are thus shown to be equal to the values represented in Table 1 for the safe side case after substituting R = 2 inches.

For the case of maximum error on the unsafe side, consider the same square, one-story building but designed to a different criteria. Instead of its capacity being set for a roof displacement from the 100%+30% rule, it has been designed for the axial load in a corner column from the 100%+30% rule. A corner column is one which receives axial force from frames in both the x-direction and the y-direction. For the example of a square building, the column would receive axial force due shaking in the x-direction and the same axial force due to shaking in the y-direction. As a hypothetical example, say this axial force is equal to 10 kips from each direction independently. When the ground shaking is applied simultaneously, the maximum of 10 kips from the x-direction and 10 kips from the y-direction will not occur at the same instant in time (just as before for the 2 inch roof displacement considered in the safe side case). However, because the response quantity of interest is now a scalar (i.e., axial force in the column) rather than a vector (i.e., roof displacement which has components both in the x-direction and the y-direction), the maximum demand is no longer limited to the maximum from each direction of shaking independently. Instead, the SRSS rule is used in the Rosenblueth and Contreras derivation. The SRSS rule is known to provide an accurate estimate of the combined response for this condition (Menun and Der Kiureghian, 1998). Thus the axial force demand in the corner column will be equal to $\sqrt{(10\ kips)^2 + (10\ kips)^2} \cong 14.1\ kips$. However, the 100%+30% rule requires instead that the corner column only be designed for $10\ kips + 0.3 * 10\ kips = 13\ kips$. Both the demand and capacity are thus shown to be equal to the values represented in Table 1 for the unsafe side case after substituting R = 10 kips.

Direction of Loading Assessment in the Literature

As mentioned previously, direction of loading has been referenced by many names, and evaluated using various methods. The following is a summary of how other researchers have approached the direction of loading issue.

Hisada et al. (1988) used the ratio of the response spectra computed using both horizontal components of ground motion to the response spectra computed using only one of the two components as a measure of the effect of concurrent seismic effects. The framework of maximum direction ground motions recently introduced in ASCE/SEI 7-10 is closely related to the work in Hisada et al. (1988).

MacRae and Mattheis (2000) assessed the SRSS, 100%+30%, and the Sum-of-Absolute-Values (SAV) rules for a steel moment frame building using nonlinear response history analysis with varying angle of ground motion incidence. The SAV rule takes the absolute value of the maximum response due to each earthquake shaking direction and adds them together. Drifts, rather than forces, were used in their evaluation "because forces do not always change significantly with displacement once the structure yields." This resulted in their reinterpretation of the 1997 UBC provisions as relating to "expected seismic drifts" rather than forces. Evaluation was conducted by first analyzing the model under each ground motion component independently to establish the SRSS, 100%+30% and SAV rules and then with both ground motion components simultaneously to predict the "true" response. They concluded that (1) the SRSS, 100%+XX% and SAV methods were dependent on the reference axes selected (i.e., at what rotation with respect to the principal axes of the building) and (2) all methods unconservatively estimated the frame inelastic story drifts.

Lopez et al. (2001) compared the SRSS, 100%+30% and 100%+40% rules to the CQC3 rule. They defined the critical response, r_{cr}, as that obtained from the CQC3 rule and found that the SRSS, 100%+30% and 100%+40% rules ranged between $1.00r_{cr}$ and $1.26r_{cr}$, $0.92r_{cr}$ and $1.16r_{cr}$, and $0.99r_{cr}$ and $1.25r_{cr}$, respectively. It was also noted that the critical response from the CQC3 method "increases when the vibration periods of the two modes that contribute most in the response to the x- and y-components of ground motion become close to each other. This effect is not taken into account by any of the multicomponent combination rules."

Zaghlool et al. (2001) assessed the 100%+XX% rules using linear and nonlinear response history analysis. Their approach took the response in the x-direction at the time of maximum response in the y-direction. This was then divided by the maximum response in the x-direction and was similarly computed for the y-direction. They describe this ratio as the "percentage activated of the maximum strong-axis response at the time of maximum weak-axis response" and can be interpreted as the XX% component of the 100%+XX% rule. From the results of their analysis, a 100%+45% rule was recommended.

MacRae and Tagawa (2001) considered linear and nonlinear response history analyses of a steel moment frame building with columns that were shared by the lateral force-resisting system in both directions. Similar to MacRae and Mattheis (2000), drifts rather than forces were used to assess the SRSS, 100%+30%, and SAV rules as shown in Figure 1. Linear response history analysis was utilized to define the combination rule envelopes. They found that the actual response for linear analysis was always within the SAV rule but often exceeded the SRSS and 100%+30% rules as seen in Figure 1a. For nonlinear analysis, all combination methods, including the SAV rule, were exceeded as seen in Figure 1b.

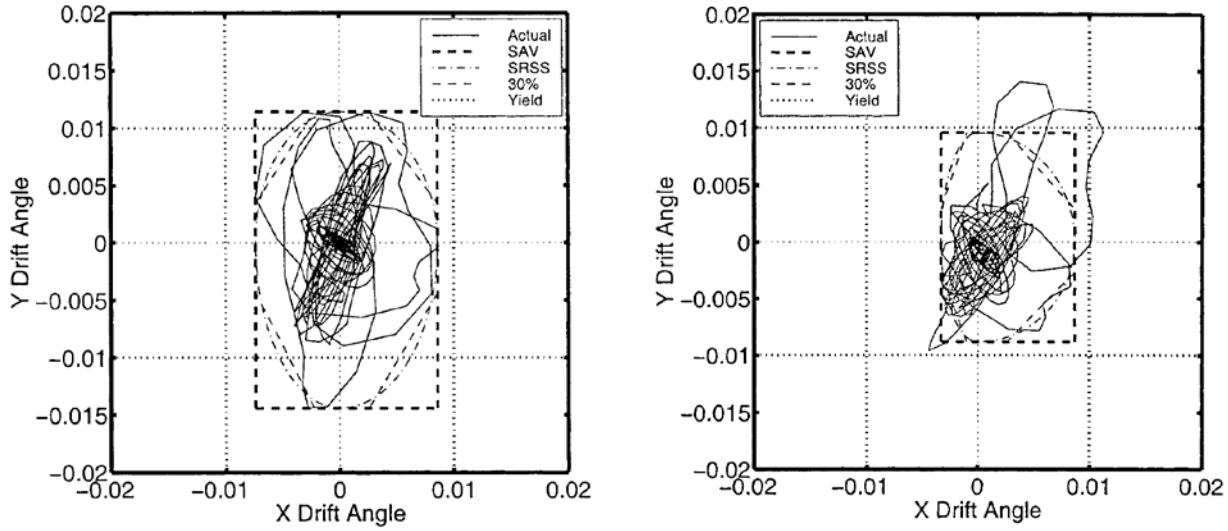

(a) (b)

Figure 1. Results and combination rules for (a) linear and (b) nonlinear response history analysis. Note that (a) and (b) use a different angle of ground motion application to the building which explains why the combination rule envelopes differ. This figure is direct reproductions of Figure 4 and Figure 5, respectively, in MacRae and Tagawa (2001).

Sherman and Okazaki (2010) analyzed buckling-restrained brace frame (BRBF) buildings with columns that were shared by the BRBFs in both directions using nonlinear response history analysis. They used two criteria for designing the shared corner columns: (1) corner columns designed for 100% of the forces due to the capacity of the BRBs in one direction and 30% of the forces due to the capacity of the BRBs in the orthogonal direction, and (2) corner columns designed for 100% of the forces due to capacity of the BRBs in both directions. This is analogous to, but not exactly the same, as the 100%+30% rule in ASCE/SEI 7 because the column forces are based on system capacity rather than lateral design forces. They found that the first design criteria were unconservative in several cases and adequate in others. The second criterion was conservative for all cases, with the degree of conservatism increasing with height of the building due to the lower likelihood that all braces would be yielding simultaneously.

Bisadi and Head (2011) evaluated the 100%+30%, 100%+40% and SRSS rules using nonlinear response history analysis of bridges. They considered two cases: (1) apply only the major component of ground motion, defined as the component having the larger PGA, in each of the longitudinal and transverse directions of the bridge independently and combine responses using the combination rules, and (2) apply major and minor components simultaneously but run one analysis at an application angle of 0 degrees with respect to the bridge axes and another at 90 degrees. Combine the 0 and 90 degree analysis using the combination rules. They then determined the probability of underestimation for each combination rule for each of the two cases considered as shown in Figure 2. Note that the probability of underestimation changes depending on whether displacement demands or force demands are considered.

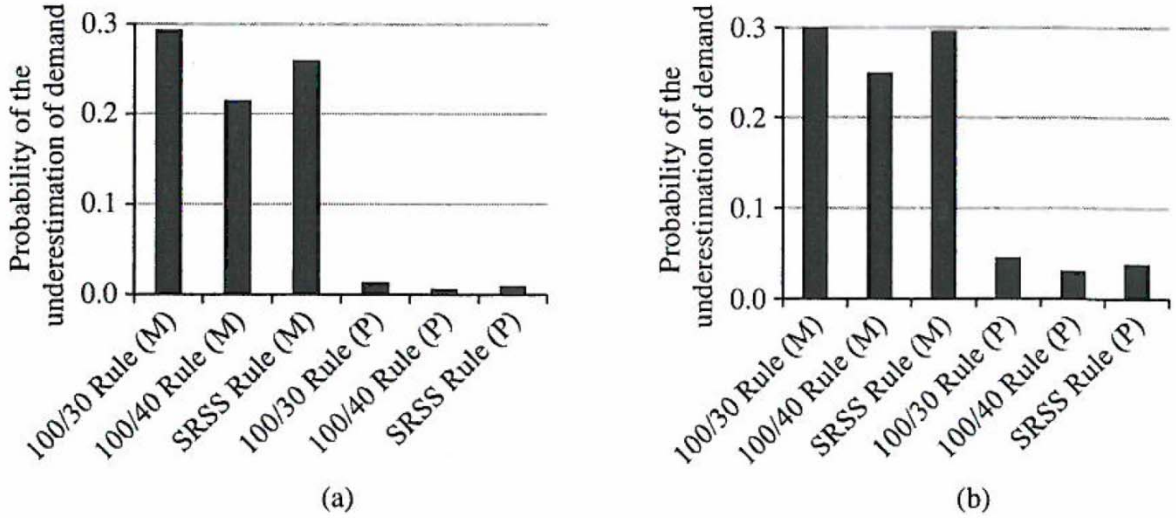

Figure 2. Probability of underestimation of (a) displacement and (b) force demands for SRSS, 100%+30% and 100%+40% combination rules. Letter M denotes only the major component of earthquake was used (Case 1) and letter P denotes that the paired record was used (Case 2). This figure is a direct reproduction of Figure 8 in Bisadi and Head (2011).

Cimellaro et al. (2014) proposed a modified nonlinear static analysis method that utilizes factors of 1.0 and 0.6 on the two orthogonal load patterns, respectively. The value of 0.6, which is different than the typical 100%+30% rule, was arrived at by calibration with nonlinear response history analysis of six highly irregular reinforced concrete frame buildings. They assert

that the difference is a result of considering nonlinear rather than linear response, the latter of which formed the basis for the 100%+30% rule.

Approaches to Assessing Direction of Loading

With a history as long as that of the direction of loading provisions' development - dating back to the 1970s with Newmark (1975) and Rosenblueth and Contreras (1977) - a strong case must be made to effect change in modern codes. Such a case requires that the direction of loading provisions be evaluated in many independent ways using a variety of evaluation techniques. Some of the groundwork has been completed and is documented in the research literature. Stepping beyond that work, the authors are currently pursuing one approach using instrumented data from the Center for Engineering Strong Motion Data (CESMD). Other potential approaches would take advantage of the more explicit collapse safety criteria in modern codes, especially ASCE/SEI 7-10.

Characterization of the ASCE/SEI 7-10 Provisions

Although the direction of loading provisions in ASCE/SEI 7-10 are procedurally fairly straightforward, on further thought, they become quite challenging to interpret conceptually. In implementing the 100%+30% rule in ASCE/SEI 7, the engineer must check eight cases corresponding to all combinations of results for each direction considering positive and negative signs. For example, one case would be 100% of the positive x-direction forces in combination with 30% of the positive y-direction forces while another case would be 100% of the positive x-direction forces in combination with 30% of the negative y-direction forces. While these cases follow directly from implementation of the provisions, it is less clear how these "control points" assure adequate building performance for other regions in the response space. For example, how is the building design expected to perform for loading at a 45 degree angle with respect to the x- and y-direction axes?

Figure 3 illustrates several interpretations of how these control points could be interpolated to capture all regions of the response space. In Figure 3a, a fairly conservative interpretation is applied where only the regions enclosed by the eight control points are considered to be explicitly captured by the 100%+30% provisions. Any response point inside of the cross shape would be considered safe while any point outside may or may not be. A less conservative interpretation of the provisions is shown in Figure 3b. It assumes that satisfying the control points ensures building performance so long as the response stays within an octagon formed by those eight points. Some judgment is required in establishing the interpolation on the diagonal. Although a linear interpolation has been pursued in prior research (MacRae and Tagawa, 2001), the original derivation of the 100%+30% rule assumed a convex "failure surface." One might then conclude that an interpretation of the ASCE/SEI 7 provisions using an elliptical interpolation as presented in Figure 3c may be more appropriate. Note that elliptical interaction reduces to circular interaction under the special case when the response in the x-direction and that in the y-direction are equal.

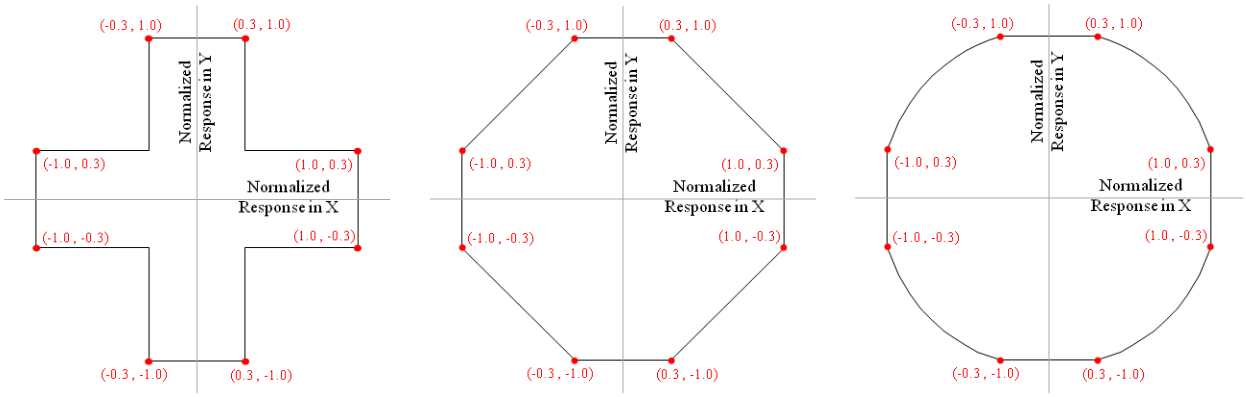

Figure 3. Interpolation of the eight control points in the ASCE/SEI 7-10 direction of loading provisions based on (a) no interpolation on the diagonal, (b) linear interpolation on the diagonal and (c) elliptical interpolation on the diagonal. Control points shown as red dots.

Assessment using Instrumented Building Data

As described in the previous section, all of the existing research on direction of loading appears to have focused on analytical studies. While these approaches are important and can add greatly to the understanding of direction of loading, they are limited by the profession's and academic community's ability to simulate the real response of structures. The existence of the Center for Engineering Strong Motion Data provides an opportunity to explore the response of real buildings during real earthquakes. The authors are currently pursuing a study which capitalizes on the advantage of access to seismically instrumented building data from the CESMD to evaluate the direction of loading provisions in ASCE/SEI 7-10.

The study takes the seismically instrumented building data from the CESMD and evaluates the relative displacement between instrumented levels, the relative displacement between an instrumented level and the ground, and the absolute acceleration of an instrumented level, all considering the simultaneous occurrence of these measures about both horizontal, principal axes of each station under each earthquake. Several metrics are defined to evaluate the 100%+XX% rule based on different evaluation techniques, some of which are conceptually described under "Characterization of the ASCE/SEI 7-10 Provisions," and the probability of exceeding each rule for the full CESMD database is calculated. This research is an ongoing effort by the authors, results of which will be reported in future publications.

The use of data from seismically instrumented buildings to assess the direction of loading procedures has the significant advantage of eliminating many sources of uncertainty by using the response of real buildings during real earthquakes. At the same time, it is also at a disadvantage compared with other, namely simulation-based, approaches. This is because a direct assessment of the direction of loading provisions requires a building to be designed by the provisions and then assessed against the collapse safety goals of the respective standard (e.g. ASCE/SEI 7) under extreme earthquake loading. The instrumented building data approach is limited on two major fronts in comparison against a direct assessment approach. Firstly, it tends to be sparse in the number of buildings which have experienced inelastic response, let alone extreme earthquake shaking. Secondly, the available data provide how a building responded to a specific earthquake

but not what the design parameters would have been if that earthquake were specified for design. The latter would require analytical modeling of the structure and would therefore exist whether or not instrumented building data was available at or near extreme earthquake shaking levels.

Other Potential Approaches

Another approach to assessing direction of loading could be pursued using the FEMA P695 (FEMA, 2009) methodology. With the explicit definition of acceptable probability of collapse for new buildings now in the commentary to ASCE/SEI 7-10, the FEMA P695 procedure could be implemented for buildings designed using the current direction of loading provisions. This would amount to designing many buildings to the current provisions and then subjecting nonlinear analytical models of them to increasing levels of earthquake shaking. In combination with the approach taken by the authors, this further research could make a strong case for changes to the direction of loading provisions in modern codes.

Summary

Research motivations and a comprehensive literature review concerning the direction of loading provisions in modern codes have been enumerated. From a review of modern codes for seismic design and rehabilitation of bridges and buildings, it is observed that the 100%+30% orthogonal combination rule is the most prevalently referenced procedure. Its derivation appears in a 1977 paper by Rosenblueth and Contreras. Since that time, many other orthogonal combination procedures have been recommended by researchers including the SRSS, CQC3 and numerous 100%+XX% methods. In recent years, nonlinear response history analysis has generally demonstrated that the 100%+30% rule underestimates building seismic response. Several studies have emphasized the evaluation of structures thought to be especially susceptible to concurrent seismic effects such as buildings with shared corner columns.

In approaching a systematic evaluation of the direction of loading provisions in a modern code such as ASCE/SEI 7-10, it is discovered that some assumptions must be made as to how the provisions ensure acceptable building performance in all regions of the response space. The authors are currently pursuing a study which uses seismically instrumented building data from the Center for Engineering Strong Motion Data to evaluate the direction of loading provisions in ASCE/SEI 7-10. This research is an ongoing effort, results of which will be reported in future publications. Finally, other potential approaches for assessing the direction of loading provisions are suggested as future research.

Acknowledgements

This paper is based on on-going research funded by the California Department of Conservation, California Geological Survey, Strong Motion Instrumentation Program, Contract 1012-957. However, these contents do not necessarily represent the policy of that agency nor endorsement by the State Government. The authors would also like to recognize the Strong Motion Instrumentation Advisory Committee (SMIAC) - Buildings Committee for their technical input.

References

AASHTO (2011). *AASHTO Guide Specifications for LRFD Seismic Bridge Design, 2nd Edition*. American Association of State Highway and Transportation Officials, Washington, DC.

ASCE (2010). *Minimum Design Loads for Buildings and Other Structures, ASCE/SEI 7-10*. American Society of Civil Engineers, Reston, Virginia.

ASCE (2013). *Seismic Evaluation and Retrofit of Existing Buildings, ASCE/SEI 41-13*. American Society of Civil Engineers, Reston, Virginia.

Bisadi, V., and Head, M., (2011). "Evaluation of Combination Rules for Orthogonal Seismic Demands in Nonlinear Time History Analysis of Bridges," *Journal of Bridge Engineering, Special Issue: AASHTO-LRFD Bridge Design and Guide Specifications: Recent, Ongoing, and Future Refinements*, p711-717.

Chu, S. L., Amin, M. and Singh, S., (1972). "Special Treatment of Actions of Three Earthquake Components on Structures," *Nuclear Engineering and Design*, Vol. 21, No. 1, p126-136.

Cimellaro, G., Giovine, T. and Lopez-Garcia, D. (2014). "Bidirectional Pushover Analysis of Irregular Structures," *Journal of Structural Engineering*, Vol. 140, No. 9, 04014059.

FEMA (2009). *Quantification of Building Seismic Performance Factors, FEMA P695*. Federal Emergency Management Agency, Washington, D.C.

Fernandez-Davila, I., Cominetti, S. and Cruz, E. F., (2000). "Considering the Bi-Directional Effects and the Seismic Angle Variations in Building Design," *Proceedings of 12th World Conference on Earthquake Engineering*, EQC, Auckland, New Zealand, Vol. 435.

FHWA (2006). *Seismic Retrofitting Manual for Highway Structures: Part 1 - Bridges*. Federal Highway Administration, McLean, Virginia.

Hernandez, J. J. and Lopez, O. A., (2002). "Response to Three-Component Seismic Motion of Arbitrary Direction," *Earthquake Engineering and Structural Dynamics*, Vol. 31, p55-77.

Hisada, T., Miyamura, M., Kan, S. and Hirao, Y., (1988). "Studies on the Orthogonal Effects in Seismic Analyses," *Proceedings of Ninth World Conference on Earthquake Engineering*, Tokyo, Japan.

ICBO (1997). *Uniform Building Code*. International Conference of Building Officials, Whittier, California.

Lopez, O. A., Chopra, A. K. and Hernandez, J. J., (2001). "Evaluation of Combination Rules for Maximum Response Calculation in Multicomponent Seismic Analysis," *Earthquake Engineering and Structural Dynamics*, Vol. 30, p1379-1398.

MacRae, G. and Mattheis, J., (2000). "Three-Dimensional Steel Building Response to Near-Fault Motions," *Journal of Structural Engineering*, Vol. 126, Issue 1, p117-126.

MacRae, G. A. and Tagawa, H., (2001). "Seismic Behavior of 3D Steel Moment Frame with Biaxial Columns," *Journal of Structural Engineering*, Vol. 127, No. 5, p490-497.

Menun, C. and Der Kiureghian, A., (1998). "A Replacement for the 30%, 40% and SRSS Rules for Multicomponent Seismic Analysis," *Earthquake Spectra*, Vol. 14, No. 1, p153-163.

Newmark, N.M., (1975). "Seismic Design Criteria for Structures and Facilities - Trans-Alaska Pipeline System," *Proceedings of the U.S. National Conference on Earthquake Engineering*, Ann Arbor, USA, p94-103.

O'Hara, G. J. and Cunnif, P. F., (1963). "Elements of Normal Mode Theory," Report 6002, Naval Research Laboratory, Washington, DC, USA.

Rosenblueth, E. and Contreras, H. (1977). "Approximate Design for Multicomponent Earthquakes," *Journal of the Engineering Mechanics Division*, Proceedings of ASCE, Vol. 103, No. EM5, p 881-893.

Sherman, J. and Okazaki, T., (2010). "Bidirectional Loading Behavior of Buckling-Restrained Braced Frames," *Proceedings of ASCE Structures Congress 2010*, Orlando, Florida.

Zaghlool, B. S., Carr, A. J. and Moss, P. J., (2001). "Inelastic Behavior of Three-Dimensional Structures under Concurrent Seismic Excitations," *Proceedings of 12th World Conference on Earthquake Engineering*, EQC, Auckland, New Zealand.

MULTI-COMPONENT DEMANDS FROM INSTRUMENTAL DATA: ASSESSMENT OF SEISMIC PROVISIONS

Dionisio Bernal, Lester Silfa and Anshuman Kunwar

Civil and Environmental Engineering Department, Center for Digital Signal Processing, Northeastern University, Boston, MA

Abstract

Modal responses from orthogonal ground motion components are found correlated by the relatively short duration of strong motion, even when the so-called principal excitation directions are aligned with the structural axes. Variance error in SRSS (or 30% rule) estimates of axial force in buildings with similar periods in two orthogonal directions are thus higher than the uncorrelated premise anticipates. A related but distinct observation is the fact that the principal ground motion directions, contrary to what is typically assumed, do not appear to be stationary during the strong motion. The term *directivity,* defined as the ratio of the singular values connected with the principal components is introduced to characterize the temporal strength of bi-directionality.

Introduction

It is customarily assumed that the seismic input to buildings can be idealized as the acceleration of a point along three orthogonal axes of a rigid foundation, one of the axes coinciding with the vertical. For design purposes the excitation is typically described by a Response Spectrum (RS) assumed to hold for any horizontal component and vertical effects are considered assuming rigid response. Estimation of peak response requires consideration of the correlation between modal responses for a given input as well as the responses to the various input components. An extension of the traditional RS method to multi-component excitation known as the CQC3 (Smeby and Der Kiureghian 1985) is built on the same assumptions that apply in the standard RS methodology, i.e. stationary response and equal peak factors, but incorporates the additional assumption that there is a set of orthogonal axes for which the input process is uncorrelated. One of the principal directions is always the vertical and in the horizontal plane the directions (for a specific motion) are those for which the temporal correlation

$$\rho_{a,b} = \int_{t_1}^{t_2} \ddot{x}_a(\tau)\ddot{x}_b(\tau)d\tau \tag{1}$$

equals zero, where subscripts *a* and *b* refer two any two orthogonal directions. The angle at which $\rho_{a,b} = 0$, typically referred to as the incident angle, θ, should be understood measured relative to the building axes. Although the assumption of a stationary principal direction has been widely used in stochastic modeling of ground motion (Yeh and Wen 1989; Kubo and Penzien

1979; Heredia-Zavoni and Machicao-Barrionuevo 2004; Menun and Der Kiureghian 1998a, Rezaeian and Der Kiureghian 2011), computations on a 4 second moving window (over the strong motion) for 30 ground motions was not found to support this premise. It's opportune to note that the concept of principal directions for seismic excitation is due to A. Arias (1970), although the reference is typically misplaced to a publication by Penzien and Watabe (1975), who were unaware of Arias work at the time of writing.

Seismic codes have traditionally addressed the question of multi-component excitation by requiring that (for some conditions) structures be capable of withstanding the maximum effects in one direction plus some fraction, β, of the maximum effects in the orthogonal one, a procedure known as the 30% or the 40% rule. Adequacy and/or conservatism of the 30% and 40% rule has been the source of discussion and, as noted by Menum and Der Kiureghian (1998a), also of significant confusion, as aspects related to the design of elements that depend on vector valued response quantities are often mixed with the issue of predicting the peak of scalar quantities.

This paper begins with an investigation on the correlation of a system mode responding to a multi-component excitation. In this regard it shows that the ratio of the true response to the SRSS prediction has a variance that is significantly higher than the theoretical expectation and that the reason is duration related. The paper examines the definition of earthquake principal direction and quantifies the strength of the bi-directionality as the *directivity*, defined as the ratio of the singular values of a matrix that has, as its rows, the selected segment of the measured components. Examination on the time evolution of the principal directions casts doubt on the usefulness of the idea of principal directions in seismic analysis. The paper contains a section describing an acceleration reconstruction scheme used to compute story wise force demands and, after discussing an approach used to define resistance contours, summarizes results on Demand to Capacity Ratios (DtCR) computed for 30 ground motions. A concluding section with critical commentary concludes the paper.

Single Mode Correlation to Multicomponent Excitation

A building considered viscously damped and elastic subjected to a bi-directional excitation on a foundation that is treated as rigid leads to set of equations that, under the assumption that the damping distribution is classical, are decoupled by the eigenvectors of the matrix $D = M^{-1}K$ where M and K are the mass and stiffness matrices respectively. Using subscripts "a" and "b" to refer to directions of analysis in the horizontal plane one finds that the amplitude of the j^{th} mode satisfies the SDOF equation

$$\ddot{Y}_j(t)+2\omega_j\xi_j\dot{Y}_j(t)+\omega_j^2Y_j(t)=\Gamma_{j,a}\ddot{x}_a(t)+\Gamma_{j,b}\ddot{x}_b(t) \tag{2}$$

where ω_j and ξ_j are the radial frequency and the ratio of critical damping of the j^{th} mode and

$$\Gamma_{j,\ell} = \phi_j^T M r_\ell \quad \ell = a,b \tag{3}$$

are the participation factors with ϕ_j as the j^{th} mass normalized eigenvector and r_ℓ is the pseudo static displacement vector associated with motion in the ℓ direction. Since the *rhs* of eq.2 for

different modes are not proportional the standard RS scheme does not apply and one is forced to treat each of the input components separately, opening the question of how to combine the resulting peaks. The accuracy of any approach can, however, always be quantified by examining how well its predictions match the result from eq.2. We examined this matter using the set of 30 bi-directional components listed in Appendix I. Since no attempt to classify the motions is made the results obtained apply loosely to what could be considered typical CA motions. Eq.2 can be written as

$$\ddot{Y}_j(t) + 2\omega_j\xi_j\dot{Y}_j(t) + \omega_j^2 Y_j(t) = \Gamma_{j,a}\left(\ddot{x}_a(t) + \alpha\cdot\ddot{x}_b(t)\right) \tag{4}$$

where the definition of α is evident. Modes significantly affected by bidirectional input have $|\alpha| \le \kappa$ where we take $\kappa = 3$. Once a value of α is fixed eq.4 can be solved for a set of periods at constant damping to obtain the "Response Spectrum" of the bidirectional motion for the particular ratio of participation factors considered. Let $\Im_\alpha(T,\xi)$ be this response spectrum, and $\Im_a(T,\xi)$ and $\Im_b(T,\xi)$ the spectra when only the motion in the "a" or the "b" direction act. With these definitions the SRSS estimate of the multi-component response of mode j is

$$\Re_{SRSS}(T,\xi,\alpha) = \Gamma_{j,a}\sqrt{\left(\Im_a(T,\xi)\right)^2 + \left(\alpha\cdot\Im_b(T,\xi)\right)^2} \tag{5}$$

where $\Re$ may be $Y, \dot{Y}, or \ddot{Y}$ and that the ratio of the true result to the SRSS prediction is

$$\vartheta_{SRSS}(T,\xi,\alpha) = \frac{\Im_\alpha(T,\xi)}{\sqrt{\left(\Im_a(T,\xi)\right)^2 + \left(\alpha\cdot\Im_b(T,\xi)\right)^2}} \tag{6}$$

Spectra for ϑ were obtained at 491 periods uniformly spaced between 0.1 and 5 seconds for the 30 bi-directional motions of Appendix I for $\alpha = \{-3,-2,-1,1,2,3\}$ and 2% damping. The mean and the standard deviation of the results at each period (for all α values) were computed and are show in fig.1. Note that the average of the standard deviation in the period band between 1.5 and 3.5 seconds is around 0.21, indicating that SRSS predictions in this band as high as 1.42 times or as low as 0.58 times the correct result were not that unusual (using 2σ under the simplified Gaussian premise).

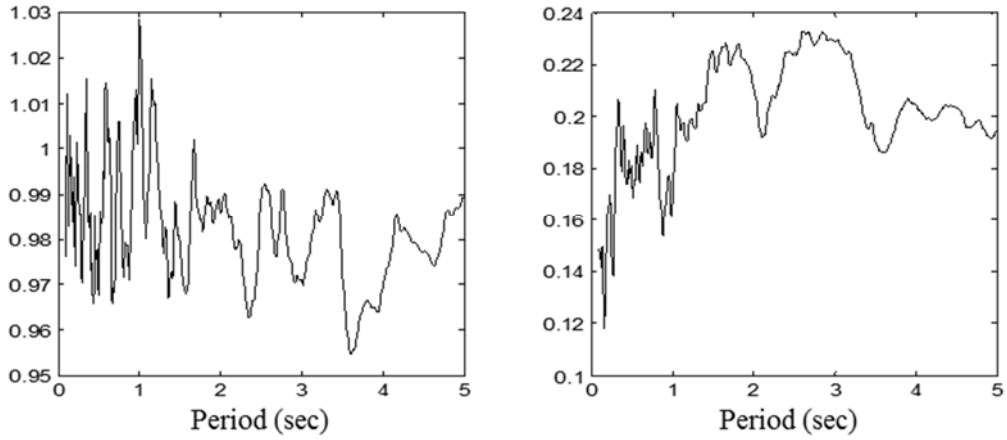

Fig.1 Ratio of exact solution to SRSS estimation vs period for 2% damping (left): mean, (right) standard deviation.

The results in fig.1 provide strong indication that the SRSS rule is not a very accurate mixer of the response of a single mode to two components of motion. Inspection suggests that the likely source of most of the error is the short duration of the strong motion. To test whether deviation from whiteness played an important role we repeated the computations by replacing each of the records with a segment of white noise with duration equal to the strong motion and repeated the simulations five times. Fig.2 compares the results from fig.1 with those from the five simulations (each with 30 motions). As can be seen, the realization for the real records is quite close to the results obtained with the noise segments, illustrating that deviation from whiteness is not an important contributor to the high variance, or to the observed bias.

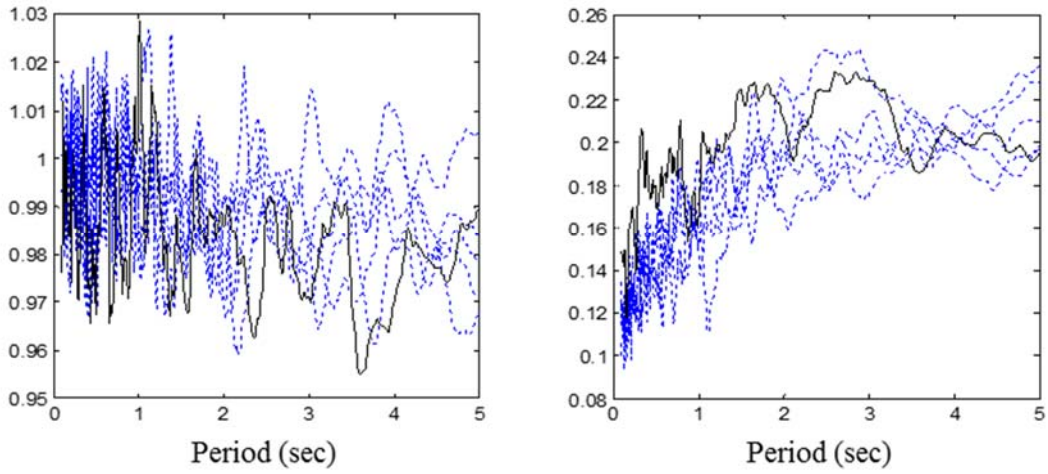

Fig.2 Comparison of result of fig.1 with those from equal duration white noise segments (continuous line is result from fig.1).

The contention that the error in the SRSS is duration related was tested by repeating the analyses with durations taken 4 times larger than the real records. The results, depicted in fig.3, clearly show how the increased duration improves accuracy.

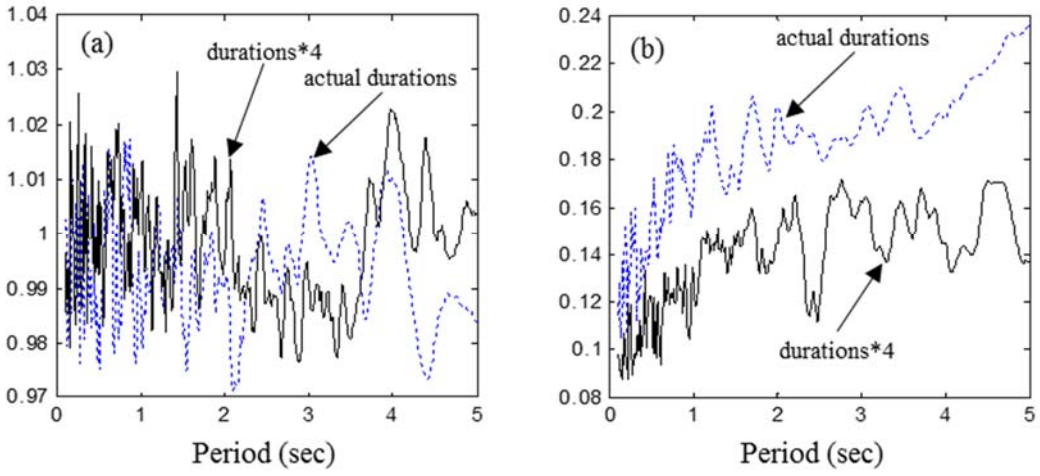

Fig.3 Results as in fig.2 computed for two durations of the white noise inputs.

Principal Directions and Seismic Directivity

Directivity

In seismology directivity is a qualitative term that refers to the focusing of wave energy along the fault in the direction of rupture. In electromagnetics the term has a precise quantitative definition as the fraction of the total power that an antenna has in its strongest direction. Here we use the term to define the relative strength of the motion along two principal components. Namely, with s_1, and s_2 as the largest and the smallest singular values of the data matrix times its transpose in some window we define directivity as

$$\gamma = 1 - \sqrt{\frac{s_2}{s_1}} \tag{7}$$

where $\gamma = 1$ for single component motion (independent of orientation) and $\gamma = 0$ if the variance is the same in all directions.

Principal Directions

The principal directions are the directions of axes where projection of the data for some selected window leads to maximum and minimum variance. If the data is essentially Gaussian within the window, and this is the case in acceleration data, the principal directions are the axis of the smallest ellipse that tightly contains the data. These directions and the dimensions of the axes can be extracted from the singular value decomposition of the matrix

$$C_{n_1}^{n_2} = \left(\frac{1}{n_2 - n_1 + 1} \right) \Upsilon_{n_1}^{n_2} \cdot \left(\Upsilon_{n_1}^{n_2} \right)^T \tag{8}$$

where $\Upsilon_{n_1}^{n_2} \in R^{2x(n_2-n_1+1)}$ contains the *as-measured* ground accelerations in the horizontal plane with n_1 and n_2 select the desired window . With $U \in R^{2x2}$ as the left singular vectors of the matrix in eq.8 the orientation of the principal direction is

$$\theta = \cos^{-1}(U_{1,1}) \tag{9}$$

and the ratio of the small to the large axis of the ellipse is

$$\eta = \sqrt{\frac{s_2}{s_1}} \tag{10}$$

from where it follows that $\gamma = 1 - \eta$.

Stationarity

Principal directions have been used to derive modal combination rules for multi-component excitation (Smeby and Der Kiureghian, 1985), to obtain expressions for the

directions that maximize scalar response quantities (Smeby and Der Kiureghian 1985; Lopez and Torres 1997), to develop envelopes of seismic response vectors (Menum and Der Kiureghian 2000) and to generate synthetic multi-component records (Rezaeian and Der Kiureghian 2010, 2012). However, permeating all of these applications there is the assumption that appears to be on shaky grounds, namely, that the principal directions can be treated as stationary during the strong ground motion. Whether this is true or not matters little when the directivity is low (e.g., $\gamma < 0.25$) but is likely relevant when directivity is significant. The window duration over which stationarity is relevant for the response at time t is $t-\tau$, where τ is some "effective duration" of the impulse response for the mode in question. Since no systematic study could be found we examined the issue of stationarity by computing the angle of incidence at time t and the directivity using a lagging window of duration τ for the suite of 30 bi-directional records in this study. A typical result computed using $\tau = 4$ secs is depicted in fig.4.

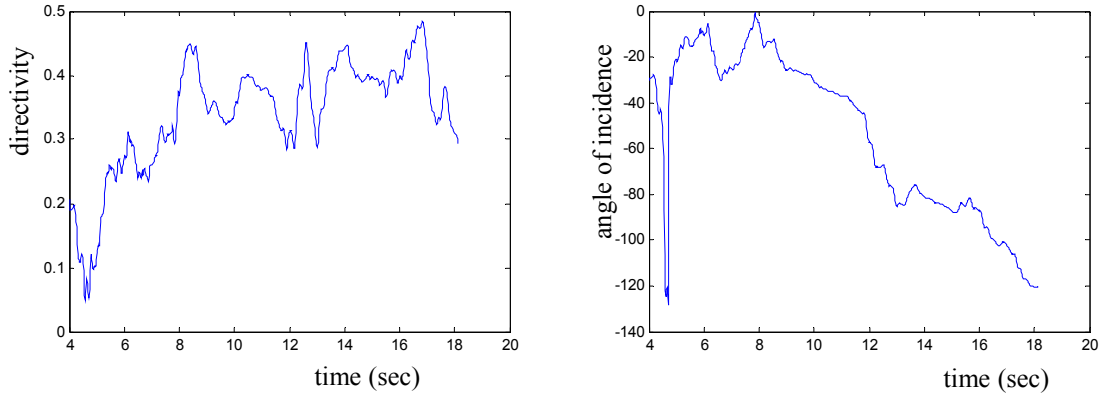

Fig.4 a) Directivity at CSMIP station 14311 during the Whittier earthquake b) angle of incidence (both computed for $\tau = 4$ secs)

As can be seen, during the early part of the strong motion the directivity is very low and the principal angle actually shifts 90 degrees at around 4.5 secs since the data is basically circular. As time passes the directivity increases but the principal direction, contrary to the typical assumption, does not stabilize. To illustrate further fig.5 depicts the data for 4 secs in two different windows, one located from 6 to 10 secs and the other from 12 to 16 secs. From inspection of fig.4a one gathers that the ellipses that contain the data for these two windows will have very close aspect ratios and this is what is observed. The angle of incidence, however, as can be seen and is anticipated from fig.4b, is very different in the two windows. To conclude this illustration, data in the window from t = 0 to t=4 secs, where the directivity is very low, is plotted in fig.6, as can be seen, the ellipse in this case is close to a circle.

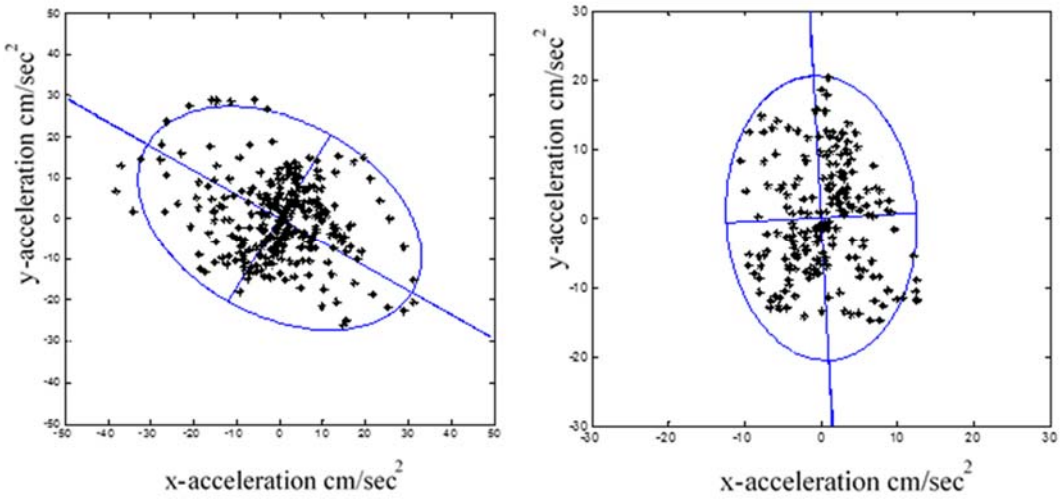

Fig.5 Accelerations, principal directions and inscribing ellipses for CSMIP station 14311 during the Whittier earthquake a) window from 6-10 secs b) window from 12-16 secs.

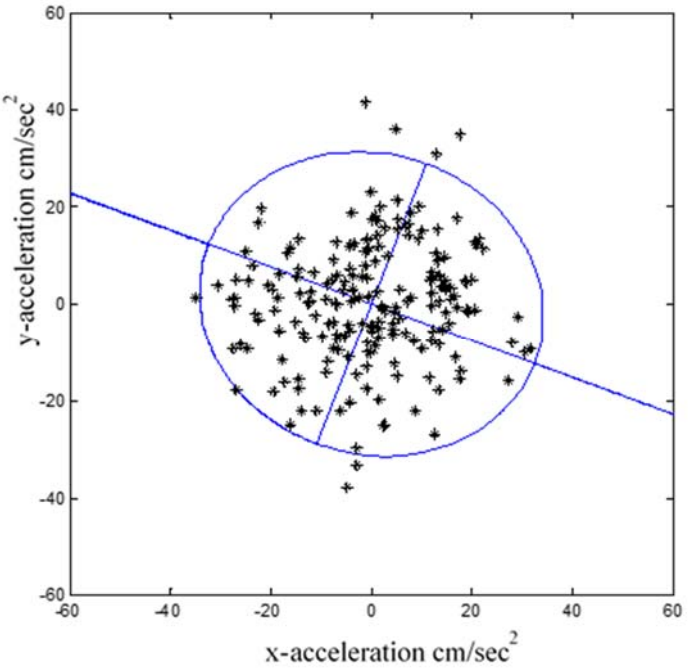

Fig.6 Accelerations, principal directions and inscribing ellipse for CSMIP station 14311 during the Whittier earthquake for the window from 0-4 secs.

Appendix I summarize the results on directivity and principal directions for the 30 motions considered in this study. The results do not support the assumption that the principal directions can be taken as stationary.

Seismic Provision for Multi-Component Excitation

The provisions on multicomponent excitation in IBC 2009, the SEAOC blue book, the NEHRP-1997 guidelines and the ASCE 7-05 code, are identical. The provisions are specified

conditional on Seismic Design Categories (SDC) that span from A to F, with A the least stringent; B next, and so on. In a language slightly less formal than that used in the codes the provisions state the following:

- For structures in SDC A and B it is sufficient to show that the structure can withstand the earthquake loading acting independently in each of the two principal directions.

- Buildings in SDC C or higher, which have non-parallel lateral load resisting systems (Irregularity Type 5) must be shown capable or resisting 100% of the loading in one direction plus 30% of the loading in the orthogonal one (as well as the 30% - 100% alternative).

- Columns of buildings in SDC D or higher, which are part of more than one lateral load resisting system and whose axial force from seismic excitation exceeds 20% of the design load have to be designed accounting for axial forces that consider the multi-component nature of the excitation using the 100-30 (30-100) rule, or the SRSS approach.

Vertical Excitation: Vibration modes in the vertical direction are typically high frequency so codes consider the vertical component of motion by requiring that the dead load induced forces be multiplied by a scalar proportional to the short period spectral acceleration.

In the discussions that follow we focus on the computation of demands accepting linear behavior. It is well-recognized, of course, that performance depends on the full force displacement relationships.

On the Relation between SRSS and the 30% (or 40%) Rule

When considering seismic combinations for design it is essential to keep in mind whether one is trying to estimate the peak of a scalar quantity or the combination of responses that a member must be able to withstand. This is particularly important when contrasting the SRSS or CQC3 rule and the 30% or 40% rule which, in a certain sense, is more general. To illustrate consider the case of a column in a structure with orthogonal frames. Assuming the structure is symmetric and neglecting torsional effects let the SRSS of the responses to the N-S and E-W earthquake action be $P_{N\text{-}S}$, $M_{N\text{-}S}$, $M_{E\text{-}W}$ etc. To bring the point across with the least clutter we neglect signs and note that the design combinations using the 30% rule would be

$$\begin{Bmatrix} P_{EW} + 0.3P_{NS} \\ M_{EW} \\ 0.3M_{NS} \end{Bmatrix} or \begin{Bmatrix} 0.3P_{EW} + P_{NS} \\ 0.3M_{EW} \\ M_{NS} \end{Bmatrix} \tag{11}$$

while the SRSS combination is

$$\begin{Bmatrix} \sqrt{P_{EW}^2 + P_{NS}^2} \\ M_{EW} \\ M_{NS} \end{Bmatrix} \tag{12}$$

The simultaneous action of the bidirectional moments on the columns required by the SRSS combination is in this case unreasonably conservative. A more detailed discussion on this issue can be found in Menun and Der Kiureghian (2000, 1998b).

Demand to Capacity Ratios (DtCR)

One of the objectives of this project was to investigate the issue of story wise capacity to demand ratios and how seismic provisions on multi-component motion may affect it. These calculations have two components: 1) estimation of the demands and 2) estimation of the capacities. The following two sections outline the approach used.

Story-Wise Demands

Reconstruction of the story-wise demands from measured data can be easily done from inertial forces if the accelerations of every level (assumed to act as a rigid diaphragm) are measured. In practice, however, not all floors are measured and there is a need, therefore, to estimate the unmeasured levels. The degree of refinement with which the reconstruction is carried out can vary significantly, depending on how much information, not included in the data itself, is called upon (Kalman 1960, Gelb 1974). A summary of the results of a project on reconstruction carried out by the writer for CSMIP in 2008 can be found in Bernal and Nasseri (2009).

Basis Fitting

As background to the approach that will be used in this project we outline the basis fitting scheme. Let subscripts *m* and *u* indicate measured and unmeasured coordinates respectively, Z be a vector of generalized amplitudes and ε a residual. With A as the vectors in the projection space and $Y \in R^{mxL}$ the data matrix with *m* = number of sensors and L = number of time steps, one has

$$\begin{Bmatrix} Y \\ y_u \end{Bmatrix} = \begin{bmatrix} A_m \\ A_u \end{bmatrix} Z + \varepsilon \tag{13}$$

so

$$Y = A_m Z + \varepsilon_m \tag{14}$$

and

$$y_u = A_u Z + \varepsilon_u \tag{15}$$

where y_u are the responses at the unmeasured coordinates. Neglecting the residual in eq.14, solving for the generalized amplitude Z and substituting in eq.15 the basis fitting predictions are

$$y_u = A_u A_m^{-*} Y \tag{16}$$

where -* stands for pseudo-inversion.

Adaptive Principal Component Reconstruction (APCR)

Let the data matrix be factored as

$$Y = USV^T \tag{17}$$

where $U \in R^{mxm}$ are the left side singular vectors and $S \in R^{mxL}$ has the structure

$$S = \begin{bmatrix} s_1 & & & 0 & . \\ & . & & 0 & . \\ & & s_m & 0 & . \end{bmatrix} \tag{18}$$

where $s_1 \geq s_2 \geq .. s_m$ are the singular values and $V^T \in R^{LxL}$ are the right side singular vectors. The p-dimensional projection that retains as much of the variance as possible is

$$Y_p = U_p B \tag{19}$$

where the projection amplitudes are

$$B = U_p^T Y \tag{20}$$

and U_p are the first *p*-columns of U. The numerical effort to compute the singular vectors can be drastically reduced by noting that these vectors are the same as those of the empirical covariance of the data matrix. Namely, one has

$$Q = YY^T = USV^T VSU^T = US^2U^T \tag{21}$$

so U can be computed by performing a SVD factorization of the matrix $Q \in R^{mxm}$. It is worth emphasizing that the vectors in U are determined entirely by the data. The number of singular vectors to retain ($p \leq m$) can be selected by inspection of the singular values, i.e. one can keep the singular values that are no less than, say 1% of the first or, if all values satisfy this criterion, one can take p = m-1 to give some room for the noise and the truncated space. The singular vectors U_p provide the matrix A_m in eq.13 so what remains to complete the reconstruction is a way to expand these vectors to the unmeasured coordinates.

We perform the expansion as follows: Let K be the stiffness matrix of some nominal (rough) model of the structure where the coordinates of all the floors (assuming a rigid diaphragm) are ordered so the ones that are monitored appear first. Let U_p be treated as imposed displacements and take the displacements at the unmeasured coordinates as the expansion. The partition U_u can thus be computed from

$$\begin{bmatrix} K_{mm} & K_{mu} \\ K_{mu}^T & K_{uu} \end{bmatrix} \begin{Bmatrix} U_p \\ U_u \end{Bmatrix} = \begin{Bmatrix} F \\ 0 \end{Bmatrix} \tag{22}$$

from where one gets

$$U_u = -K_{uu}^{-1} K_{mu}^T U_p \tag{23}$$

The APCR prediction of the response at the unmeasured coordinates is thus

$$y_u = -K_{uu}^{-1} K_{um} U_p U_p^T Y = U_u U_p^T Y \tag{24}$$

Note that if a projection in identified modes is extrapolated in the same way as in eq.24 the prediction at the unmeasured coordinates is

$$y_u = -K_{uu}^{-1} K_{um} \phi_p \phi_p^{-*} Y \tag{25}$$

where ϕ_p is the matrix with the identified modes at the measured coordinates (which, for uniqueness must be tall). Mathematically the difference between APCR and a modal projection resides, therefore, in the difference between $U_p U_p^T$ and $\phi_p \phi_p^{-*}$. The primary advantage of APCR is the fact that U_p is easily computable from the data and avoids the need to perform identification.

Story Shear Limit State Contour

Given a structure and a distribution of lateral forces in the height the story shear strength contour at any desired limit state e.g., first yield or ultimate can be estimated from a 3D nonlinear model using incremental static analysis where the angle of the applied load is varied (fig.7).

3D Pushover Analysis

To gain some insight into the shapes of the story shear contours we computed the strength envelopes for the first story shear capacity on two buildings, one concrete and one steel, both shown in fig.8. The buildings where modelled using distributed plasticity and results were computed for a uniform distribution of the lateral load along the height; a pattern chosen because studies reported in Bernal (1992, 1998) show that this distribution leads to mechanisms that are in good accord with the mechanism that controls failure during strong motion. The results obtained for the base shear capacity contour, normalized to the unidirectional results are depicted in fig.9

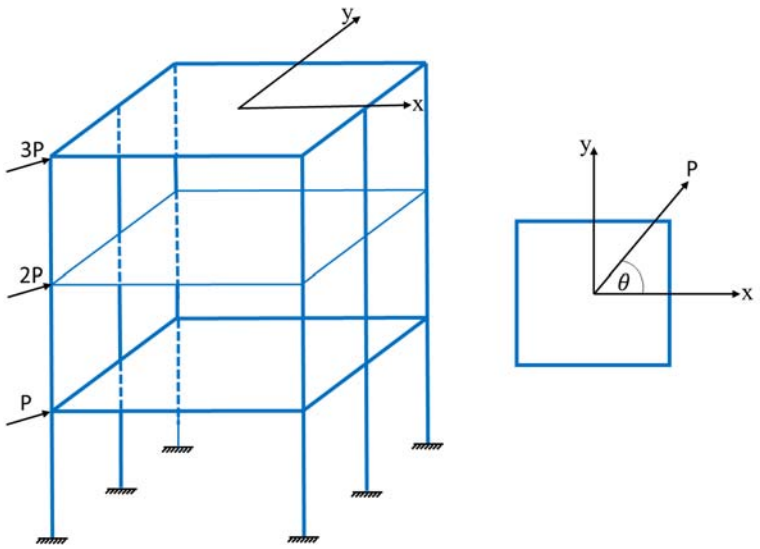

Fig.7 Schematic Illustration of 3D Pushover

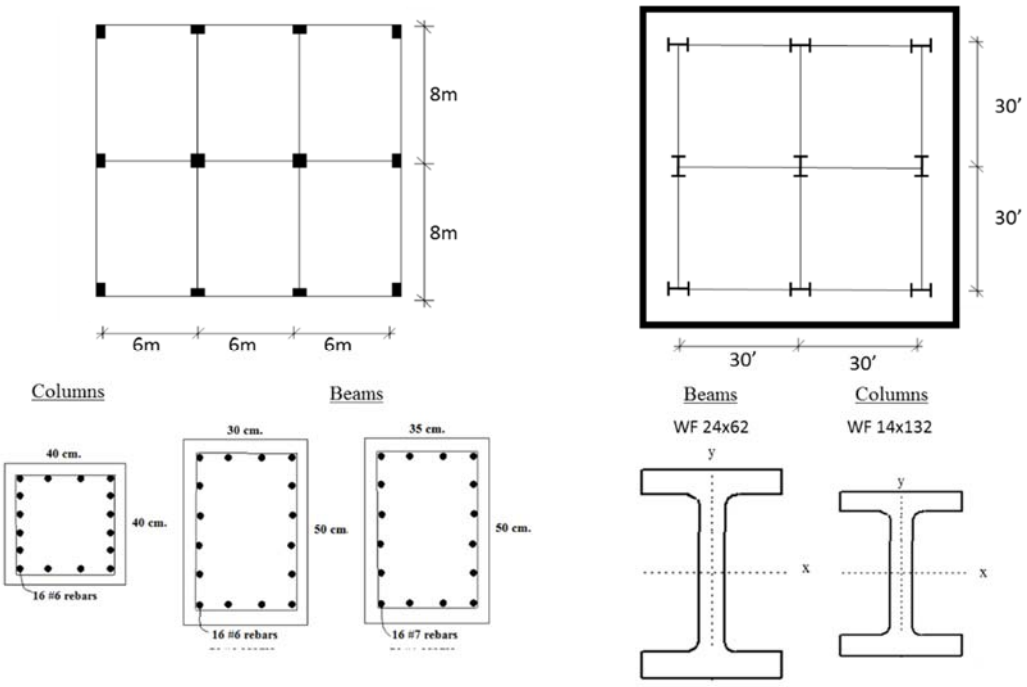

Fig.8 Two buildings used to compute the story shear strength contour.

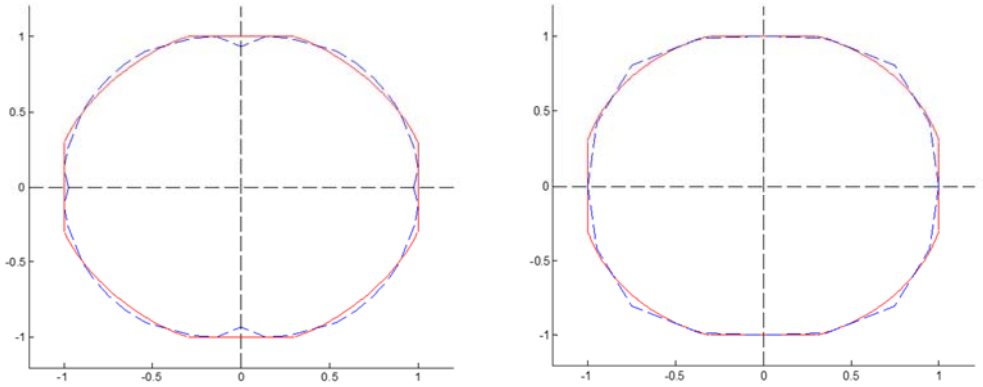

Fig.9 Normalized story shear strength contour a) concrete building b) steel building (broken line is the true normalized capacity and the solid lines are results from a parameterized resistance envelop governed by β and η presented next).

Normalized Envelope

If the strength of a story in shear is determined by the flexural capacity of columns it is reasonable to expect that the shape of the strength contour will reflect the biaxial bending interaction diagram of the individual columns. These interaction diagrams have shapes that depend on whether one is dealing with wide flange steel sections or with reinforced concrete as well as on the details of the geometry. A very common expression used on the premise that the axial force is constant is

$$\left(\frac{M_x}{M_{px}}\right)^{\alpha}+\left(\frac{M_y}{M_{py}}\right)^{\alpha}=1 \qquad (26)$$

where a determines the shape of the interaction. Concrete column design is typically carried out on the premise that $1.15 \pounds a \pounds 1.55$ (Bresler, 1960) while steel design guides often use $a = 1$. A theoretical examination shows, however, that these selections can be very conservative, as is apparent from inspection of fig.10, which shows results for a wide flange section (Santasathaporn and Chen 1968).

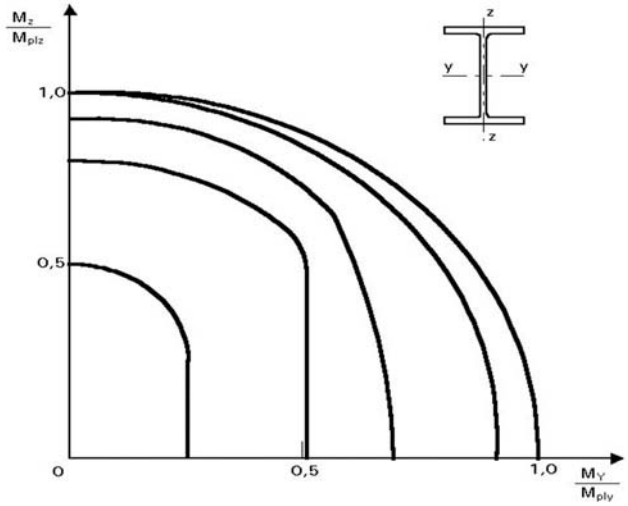

Fig.10 Interaction diagram for biaxial bending at constant axial load for a steel shape

Observation

If the lateral load resisting planes are orthogonal and there are no shared columns bi-directionality issues are not relevant. We focus on the common situation where the resisting planes are orthogonal but there are shared columns. In this instance it appears reasonable to assume that the shear strength of a story is similar in shape to the sum of the interaction diagrams for all the individual columns. Nevertheless, if the columns are conservatively designed so that plasticity is essentially restricted to beams then the strength contour will tend to approach a square.

Construction

The contour used for the computations of DtCR is constructed as follows: assume that a set of seismic provisions requires that the building be checked using a load combination that includes full loading in one direction plus β times the full loading in the other. This implies that points (1,β) and (β, 1) are inside the safe region so we take them, conservatively, to be on the capacity plot. In the schematic illustration in fig.11 the two noted points are labeled as A and B. The next control point, C, is on the 45 degree line (in the first quadrant) and is specified in terms of two auxiliary points a_1 and a_2. As the figure illustrates, the two auxiliary points are also on the 45 degree line, the first is at the intersection with the straight line that joints A and B and the second is on a circle that passes through A and B. The control point C is taken to lie $n\times\Delta$ away from a_1 in the direction of a_2, where $n \geq 0$ and Δ is the length of the a_2-a_1 segment.

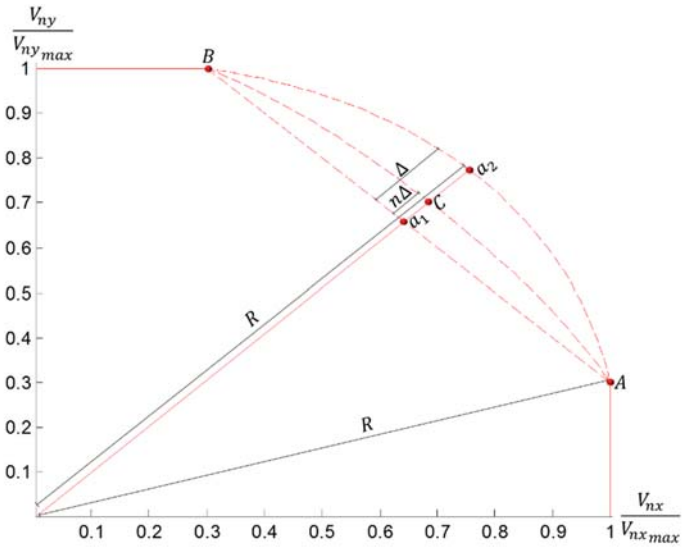

Fig.11 Schematic illustration of the normalized resistance envelope

The definition of the DtCR is shown in fig.12. Namely, it is the ratio of the demand at any time to the capacity anticipated under a monotonic load that produces a response having the same orientation of the demand. During most of the response DtCR is less than one but there are instances, as is the case in the point shown in the figure, where DtCR may exeed unity and what we're interested in is determining what are the statistics of these values, given the assumed

stregth contour. In discussions that follow, when we refer to the probability of exeeding a certain DtCR, only values that are greater than one are considered.

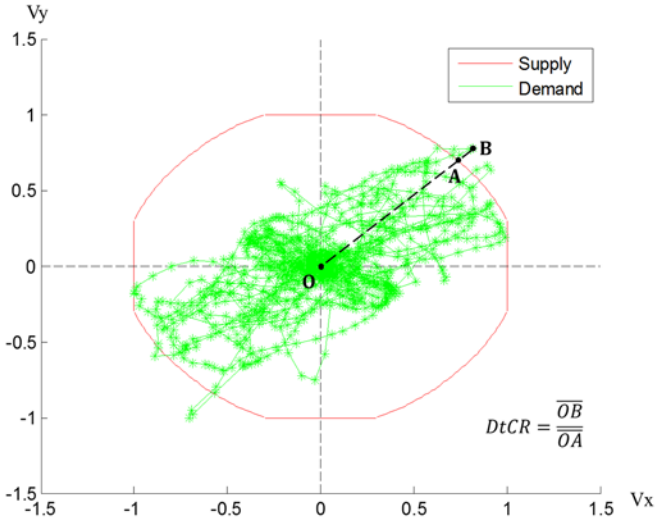

Fig12. Normalized story shear supply-demand

Results

The first question inspected was whether there was justification for treating concrete and steel buildings in two different categories. We did not anticipate that this should be the case since multicomponent excitation issues are not building material related and examination of results showed that this was in fact the case. The next issue was what values of β and η to use to formulate the normalized resistance contours. In the end it was decided that seven values of β from 0 to 0.4 and two values of η, 0.25 and 0.75 would provide adequate coverage. What was done can be outlined as follows:

- For each of 30 cases compute the story shear demand (in all levels)
- Select a β , η pair
- Compute the DtCR
- Extract the values that are larger than one and place them in the vector $\Gamma(\beta,\eta,story)$

Obtain

$$\left\{\Gamma_{\gamma} = \Gamma_{\beta,\eta} \middle| \Gamma_{\beta,\eta} > \gamma\right\} \tag{27}$$

- Compute

$$p(\gamma) = \frac{length(\Gamma_{\gamma})}{length(\Gamma_{\beta,\eta})} \tag{28}$$

- Plot γ vs p(γ).

The results of the steps listed are presented in fig.13 and 14 in the first level for the two η values considered.

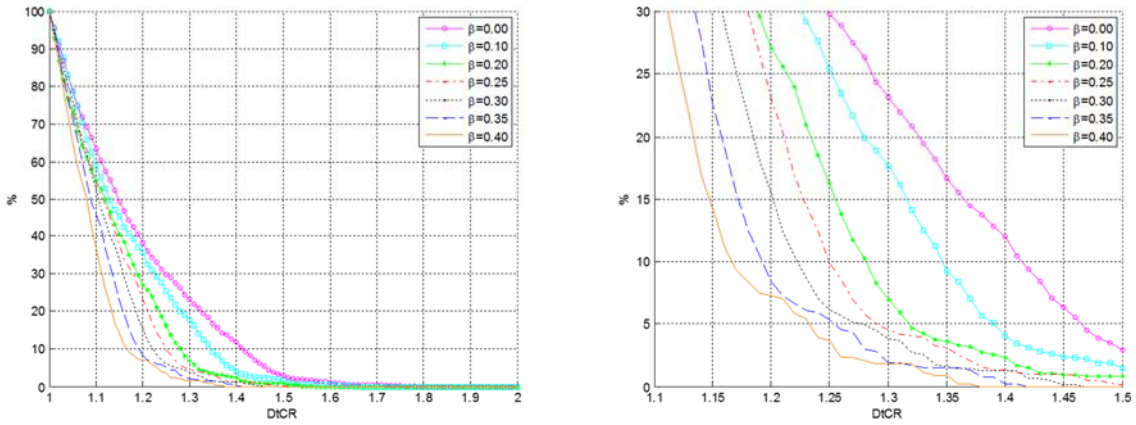

Fig.13 Result of eq.28 (in %) vs DtCR for η = 0.25

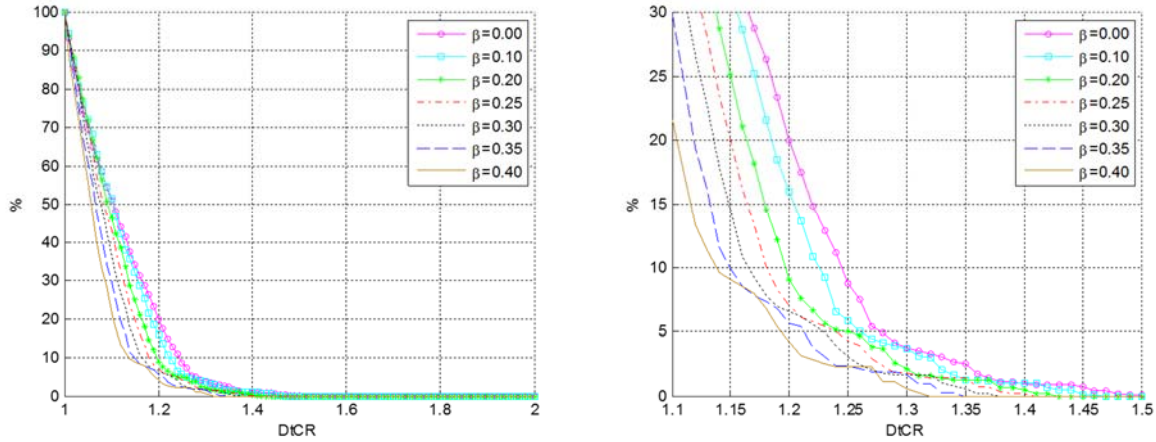

Fig.14 Result of eq.28 (in %) vs DtCR for η = 0.75

Another item we focused on was the number of times that any γ level was exceeded. The results for the average number are presented in figs. 15 and 16.

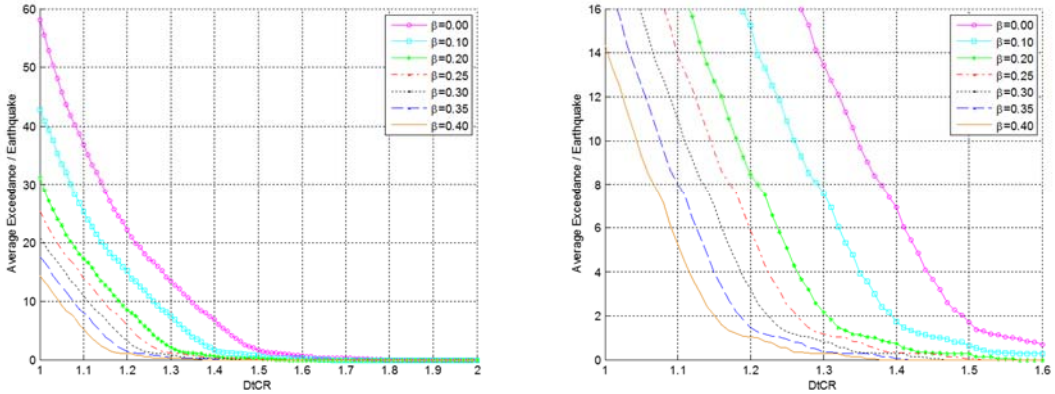

Fig.15 Average number of times that a given DtCR is exceeded for η=0.25

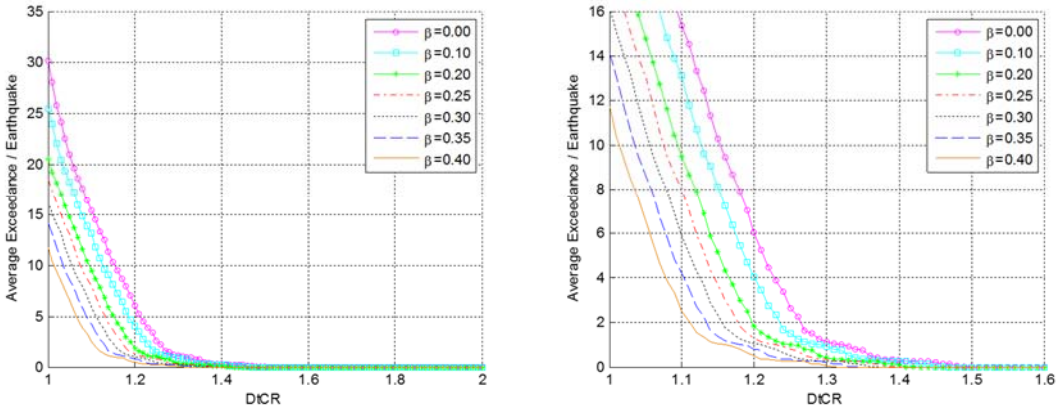

Fig.16 Average number of times that a given DtCR is exceeded for η=0.75

Biaxial Effects on Inelastic Response

Albeit only exploratory, a final item examined was how bi-directionality affected local inelastic demands. For this purpose the steel structure previously shown in fig.8 was subjected to the two components of Chinohills whose maximum accelerations are (.0503 and .0362 g's). The motions were scaled progressively and the maximum strain in fibers that yielded was recorded. The structure was then loaded only by the x-component and the same results tracked. The summary presented in fig.17 shows some modest increase in the inelastic demands in columns and negligible effect, as expected, in the beams.

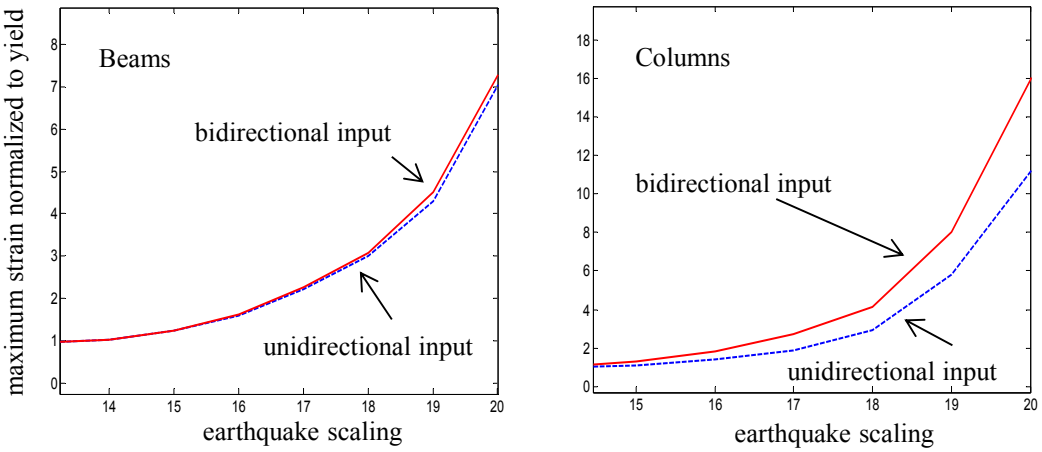

Fig.17 Comparison of inelastic demands in the steel structure of fig.8 subjected to the Chinohills earthquake.

Concluding Comments

Examination shows that the responses of a mode to two uncorrelated components are correlated. The correlation decreases with effective motion duration but for typical durations is significant in a large part of the relevant bandwidth. Worthy of restating is the fact that the assumption of stationarity on the principal direction, assumed for various purposes in earthquake engineering, was not supported by results obtained for the 30 motions in Appendix I. Implication

of the results for story wise demand to capacity ratios are not easily made since over-strength and inelastic behavior play a critical role in performance. Keeping this mind, however, one may note that for $\beta = 0$ and $\eta = 0.25$ the DtCR at 10% probability of exceedance was slightly larger than 1.4 with an average number of overshooting of around 6 times per record. The strategy of the codes to require the 30% rule (or the SRSS) to protect columns that are heavily loaded is well placed. Whether or not the relatively large variance of the estimation should be explicitly considered remains to be examined.

Acknowledgment

The research reported in this paper was carried out with support from the California Strong Motion Instrumentation Program (CSMIP) through standard agreement 1016-956. This support is gratefully acknowledged.

References

Smeby, W. and Der Kiureghian, A. (1985), "Modal Combination Rules for Multicomponent Earthquake Excitation." Earthquake Engineering and Structural Dynamics, 13: 1-12.

Yeh C. H. and Wen Y. K. (1990), "Modeling of Non-stationary ground motion and Analysis of Inelastic Structural Response." Structural Safety, 8(1-4): 281-298.

Kubo, T. and Penzien, J. (1979), "Analysis of three-dimensional strong ground motions along principal axes, San Fernando earthquake." Earthquake Engineering and Structural Dynamics, 7(3): 265-278.

Heredia-Zavoni, E. and Machicao-Barrionuevo, R. (2004), "Response to orthogonal components of ground motion and assessment of percentage combination rules." Earthquake Engineering and Structural Dynamics, 33(2): 271-284.

Menun, C. and Kiureghian, A. (2000), "Envelopes for Seismic Response Vectors. I: Theory." Journal of Structural Engineering, 126(4): 467-473.

Rezaeian, S. and Der Kiureghian, A. (2012), "Simulation of Orthogonal horizontal ground motion components for Specified earthquake and site characteristics." Earthquake Engineering and Structural Dynamics, 41(2): 335-353.

Arias, A. (1970), "A measure of earthquake intensity in seismic design for nuclear power plants: R. J. Hansen, ed., MIT Press, p. 438-483.

Penzien, J. and Watabe, M. (1974), "Characteristics of three dimensional earthquake ground motions." Earthquake Engineering and Structural Dynamics, 3(4): 365-373.

Menun, C. and Der Kiureghian, A. (1998a), "A Replacement for the 30%, 40% and SRSS Rules for Multicomponent Seismic Analysis." Earthquake Spectra, 14(1): 153-156.

Menun, C. and Der Kiureghian, A. (1998b), "Response to J. J. Hernandez and O. A. Lopez 'Discussion of "A Replacement for the 30%, 40% and SRSS Rules for Multicomponent Seismic Analysis"." Earthquake Spectra, 14(4): 717-718.

Lopez, O. A. and Torres, R. (1997), "The Critical Angle of Seismic Incidence and the Maximum Structural Response." Earthquake Engineering and Structural Dynamics, 26: 881-894.

Rezaeian, S. and Der Kiureghian, A. (2010), "Simulation of synthetic ground motions for specified earthquake and site characteristics." Earthquake Engineering and Structural Dynamics. 39:1155-1180.

Kalman, R. E. (1960), "A New Approach to Linear Filtering and Prediction Problems." Journal of Fluid Engineering, 82(1): 35-45.

Gelb, A. editor (1974), "Applied Optimal Estimation." MIT press, Cambridge, MA.

Bernal, D. and Nasseri, A. (2009), "Instrumental Assessment of the Predictive Capability of Nonlinear Static Analysis Procedures for Seismic Evaluation of Buildings." Improving the Seismic Performance of Existing Buildings and Other Structures: 731-740.

Bernal, D. (1992), "Instability of Buildings subjected to Earthquakes." Journal of Structural Engineering, 118(8): 2239-2260.

Bernal, D. (1998), "Instability of Building during Seismic response." Engineering Structures, 20(4-6): 496-502.

Bresler, B. (1960), "Design Criteria for Reinforced Columns under Axial load and Biaxial Bending." Journal Proceedings, 57(11): 481-490.

Santathadaporn, S. and Chen, W. F. (1968), "Interaction Curves for Sections under Combined Biaxial Bending and Axial Force." Fritz Engineering Laboratory Report No. 331.3.

Appendix I – Motion ensemble and its characterization

						τ= 4 sec.			
Station	Component	$\frac{(Max\ acc.)}{g}$	$t_{0.9}$	θ	γ	σ_θ	θ_{max} / θ_{min}	γ_{max} / γ_{min}	t_0
02160(IV)	W-E	0.238	11.54	115.96	0.31	29.48	0.00	0.50	16.82
	N-S	0.299					-131.72	0.01	
12284(BS)	W-E	0.053	24.59	88.53	0.27	28.01	-0.02	0.50	52.27
	N-S	0.080					-131.72	0.01	
12284(C)	W-E	0.048	35.23	154.34	0.30	27.20	-0.18	0.50	78.18
	N-S	0.035					-131.72	0.01	
12284(PS)	W-E	0.069	24.00	84.11	0.26	20.42	-0.11	0.66	28.28
	N-S	0.101					-134.55	0.01	
14311(CH)	N-S	0.050	23.49	147.63	0.25	28.08	-0.14	0.48	47.49
	W-E	0.036					-105.53	0.10	
14311(W)	N-S	0.052	18.18	146.20	0.18	27.06	-0.06	0.48	23.26
	W-E	0.044					-129.25	0.05	
23285(SB)	N-S	0.025	4.72	167.68	0.38	29.33	0.00	0.50	28.28
	W-E	0.015					-131.72	0.01	
23515(L)	W-E	0.068	41.20	48.68	0.03	29.05	-0.02	0.53	51.12
	N-S	0.088					-131.72	0.01	
24288(CH)	W-E	0.048	16.43	135.40	0.49	34.57	-0.06	0.62	41.56

	N-S	0.066					-131.72	0.00	
24370(SM)	N-S	0.118	10.10	79.90	0.14	30.45	-0.03	0.53	13.54
	W-E	0.102					-132.57	0.01	
24370(W)	N-S	0.214	7.04	170.83	0.31	30.40	-0.03	0.53	10.94
	W-E	0.161					-131.72	0.01	
24385(SM)	W-E	0.054	3.22	67.15	0.37	29.59	-0.03	0.53	3.86
	N-S	0.068					-131.72	0.01	
24385(W)	W-E	0.184	6.28	177.98	0.35	30.29	-0.03	0.53	10.22
	N-S	0.116					-131.72	0.01	
24514(W)	W-E	0.064	13.78	164.71	0.21	29.59	-0.03	0.53	20.02
	N-S	0.047					-131.72	0.01	
24571(L)	N-S	0.039	24.96	136.12	0.20	30.56	-0.42	0.63	33.14
	W-E	0.033					-131.72	0.01	
24571(N)	N-S	0.191	10.51	164.04	0.68	31.40	0.00	0.53	16.69
	W-E	0.156					-131.72	0.01	
24571(SM)	N-S	0.237	3.18	165.35	0.68	29.05	-0.02	0.53	4.88
	W-E	0.096					-131.72	0.01	
24629(CH)	W-E	0.057	17.41	132.51	0.39	33.15	-0.01	0.62	35.22
	N-S	0.059					-133.02	0.01	
24629(N)	W-E	0.092	35.24	129.76	0.20	31.58	-0.06	0.52	46.46
	N-S	0.067					-114.83	0.02	
24652(N)	W-E	0.121	17.74	135.45	0.13	25.44	-0.27	0.52	29.01
	N-S	0.206					-127.75	0.02	
47459(LP)	W-E	0.359	8.82	160.91	0.46	27.87	-0.05	0.52	12.10
	N-S	0.262					-123.79	0.02	
58261(LP)	N-S	0.138	13.40	176.69	0.37	31.59	-0.18	0.55	23.34
	W-E	0.124					-120.83	0.01	
58348(LF)	N-S	0.047	6.51	148.47	0.16	33.75	0.00	0.56	33.39
	W-E	0.054					-124.97	0.02	
58348(LP)	N-S	0.063	18.48	64.33	0.23	35.50	0.00	0.56	26.70
	W-E	0.110					-118.55	0.02	
58364(LP)	N-S	0.359	8.82	160.91	0.18	27.87	-0.05	0.52	12.10
	W-E	0.262					-123.79	0.02	
58394(LP)	W-E	0.110	12.72	137.99	0.35	27.39	-0.27	0.52	20.64
	N-S	0.121					-131.90	0.01	
58462(LP)	N-S	0.081	20.60	179.57	0.35	29.56	0.00	0.52	29.58
	W-E	0.103					-133.36	0.02	
58503(E)	W-E	0.030	4.13	98.19	0.04	29.56	0.00	0.52	30.62
	N-S	0.035					-133.36	0.02	
58503(LP)	W-E	0.048	11.38	55.74	0.07	28.58	-0.01	0.52	23.24
	N-S	0.053					-133.36	0.01	
58506(LP)	N-S	0.083	22.04	92.18	0.40	32.05	-0.07	0.52	36.36
	W-E	0.094					-133.62	0.01	

t_0= start of strong ground motion, $t_{0.9}$ = effective duration , σ_θ,= mean of std of θ on a running window of 4 secs, γ_{max}, γ_{min} , θ_{max},θ_{min} maximum and minimum values over the strong motion computed on a 4 sec running window.

SEISMIC PERFORMANCE ANALYSIS OF PILE-SUPPORTED WHARVES SUBJECTED TO LONG-DURATION GROUND MOTIONS

Stephen Dickenson[1], Songtao Yang[2], Doug Schwarm[3], and Matt Rees[2]

[1] New Albion Geotechnical, Inc., Reno, NV
[2] CH2M Hill, New York, NY
[3] Atlas Geotechnical, Inc., Santa Cruz, CA
[4] CH2M Hill, Swindon, UK

Abstract

The impact of long-duration, design-level ground motions on the seismic performance of a pile-supported wharf has been evaluated using a practice-oriented 2D geomechanical model validated with case history data and supplemented with results from large-scale tests on representative pile-deck connections and pile-rockfill interaction. The modeling focuses on a wharf at Pier 400 Port of Los Angeles, the location of an extensive CGS SMIP strong motion instrumentation array. This paper provides a synthesis of modeling considerations and summary of the computational results for a subset of motions used in the investigation. The modeling has highlighted the impacts of pile kinematic loading due to foundation deformations associated with long-duration seismic loading. The phasing of inertial and kinematic loading on the pile foundations has been a primary consideration as well as approximate thresholds for pile damage due to displacement demand.

Introduction

This investigation addresses the effects of long-duration ground motions on the Soil-Foundation-Structure-Interaction (SFSI) and seismic performance of pile supported wharves in California. While pile supported wharves have been considered rather simple structures, dynamic SFSI of pile-supported wharves represent a complex geotechnical and structural interaction problem. The combination of inertial loading and kinematic effects due to seismically-induced ground displacement (i.e. displacement demand) imposes foundation loads that are commonly out-of-phase and quite variable depending on vertical and lateral location relative to the sloping face of terminal wharves. Observed failures to wharf foundations are often associated with geotechnical failures (liquefaction, cyclic degradation, slope instability). Field reconnaissance and inspection at ports after moderate to large earthquakes routinely finds that damage to waterfront structures and associated loss of operations are directly related to permanent ground deformation and large displacement demand on pile foundations, cutoff walls and anchor systems, and appurtenant structures (ASCE TCLEE 1998, PIANC WG34 2001, ASCE/COPRI 2014a).

In order to simulate the global movement of the waterfront slope, pile deformation, and possible wharf displacement in a coupled manner the 2D numerical dynamic SFSI modeling has been performed using the commercially available program FLAC, a geomechanical model

wherein the soil profile is modeled as a continuum and the wharf, deck, and pile foundation are modeled using relatively simple structural elements. This program has been selected for application due to the wide usage in port engineering practice (e.g., Roth et al. 2003; Roth and Dawson 2003; Arulmoli et al. 2004; Dodds et al. 2004; Moriwaki et al. 2005, Yan et al., 2004) and the experience of the project team with this code for port and waterfront applications. The effort has included both the calibration of a practical dynamic SFSI modeling procedure and the application of the validated model for evaluating the impact of long-duration motions on the seismic performance of a modern wharf structure.

The adoption of performance-based seismic design provisions at major ports and marine oil terminals in California necessitates the reliance in engineering practice on numerical models for simulating dynamic SFSI of wharf and embankment structures. Recent investigations of the seismic performance of pile supported wharves have developed enhanced methods of analysis (e.g.; Chiaramonte et al., 2011; Shafieezadeh et al. 2012); however, the lack of well-documented, instrumented field case histories has precluded thorough validation of analysis methods for simulating dynamic SFSI of these structures. Berth 404 at Pier 400, Port of Los Angeles provides an extremely valuable test bed for this investigation. The wharf represents recent design and construction practices, and constitutes a very important terminal at the port. The wharf and embankment configuration is similar to other major terminals at the Port of Los Angeles and the adjoining Port of Long Beach, yet the Pier 400 site is particularly valuable due to the following;

1. Extensive CSMIP strong motion array along a portion of the wharf, as shown in the Figure 1. CSMIP stations #14284 and #14256 provide 3 free-field and 15 structural accelerometers, respectively.
2. The type and configuration of the piles (24" octagonal prestressed concrete piles; seven piles per bent) are consistent with contemporary port design in California.
3. Large-scale structural modeling of representative pile-deck connections has been performed (Restrepo et al., 2007; Krier et al., 2008). The Force-Displacement and Moment-Rotation behavior of the pile-wharf deck connection has been very well characterized.
4. Large-scale modeling of pile-rockfill interaction (Kawamata, 2009) has been performed for conditions very similar to that at Pier 400. This work has provided very useful data for Force-Displacement and p-y behavior of piles in rockfill.
5. A geophysical investigation (MASW, ReMi) performed as a portion of this investigation has provided shear wave velocity profiles through zones of unimproved hydraulically-placed backland fill and in zones of fill treated with stone columns (Dickenson et al, 2013).
6. An extensive regional PSHA and port-wide ground motion characterization has been completed (EMI, 2006).
7. Ground motion data has been obtained at the instrumentation array for short-duration, weak to moderate motions recorded during the M_w 4.7 May 17, 2009 Inglewood Area Earthquake (PGA ≈ 0.10g in free-field and ≈ 0.20g on the edge of the wharf deck). These motions have been useful for validation of elastic properties used in FLAC.

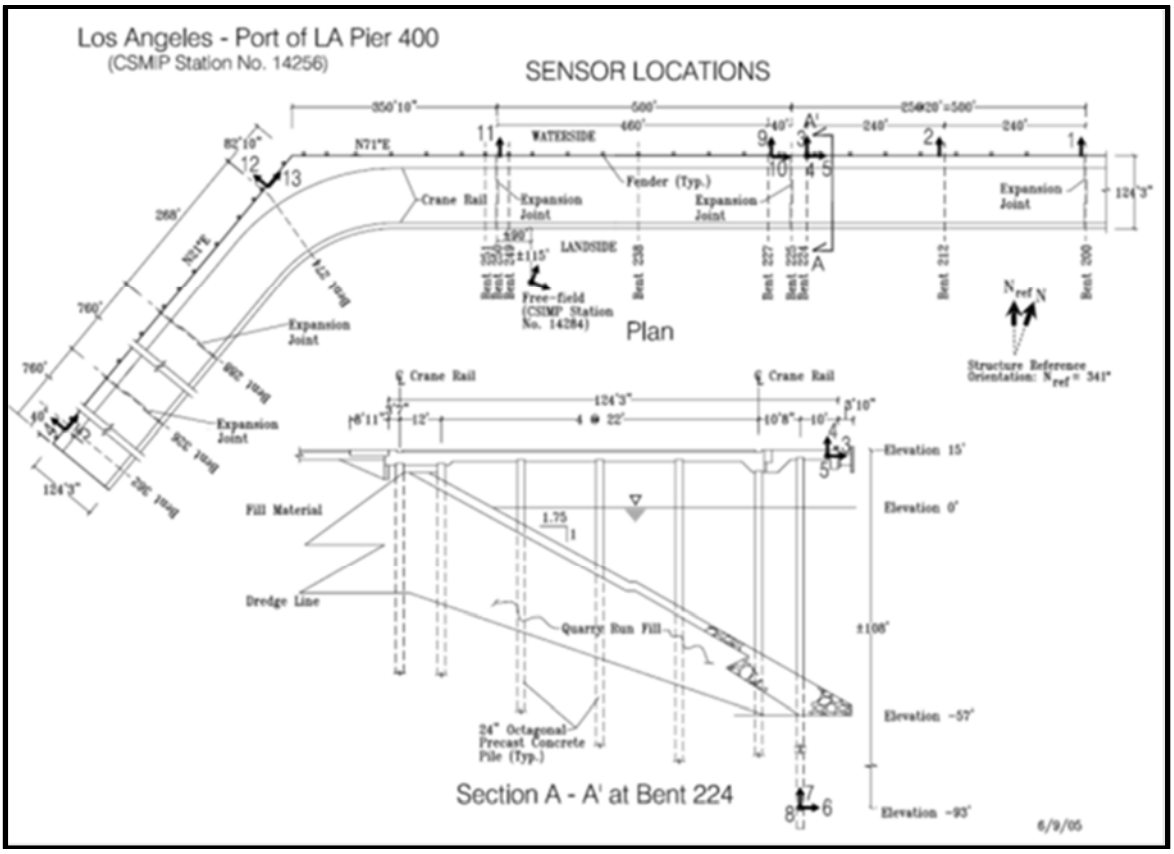

Figure 1: CSMIP Instrumentation Array at the Port of Los Angeles Pier 400 (CGS - CSMIP Station 14256), Center for Engineering Strong Motion Data (CESMD)

In order to validate the numerical model a major effort has been undertaken to collect supporting information and data required for robust nonlinear SFSI modeling. This has included; port reports on geotechnical site characterization, dynamic soil properties, geotechnical interpretation and design (Fugro West 2001a, b, c), structural seismic design and detailing (Priestley 2000, Weismair et al 2001), construction materials and methods (Degen et al. 2005, Fugro West 2004), as-built drawings (POLA 2002), and large-scale physical model testing of pile-wharf deck connections (Krier et al. 2008, Lehman et al. 2013, Restrepo et al. 2007) and pile-rockfill interaction (Kawamata 2009). The first phase of this project focused on the synthesis of geotechnical, structural, and strong motion data at three port sites instrumented by CSMIP. Background on the initial efforts and model validation has been presented by Dickenson and others (2013). A summary of pertinent aspects of the site characterization and considerations for modeling of Berth 404 are provided as follows.

Geotechnical Site Characterization

The geologic cross section and structural configuration at Berth 404 are provided in Figure 2. As defined by Fugro West (2001a, b, c); from youngest to oldest the soil profile consists of;

1. Hydraulic fill consisting of predominantly silty sand, with layers of sandy silt and silt with clay balls. The construction sequence associated with dredging, characteristics of fill based on borrow area, and the influence of placement techniques on density are addressed by Fugro West (2001a, b) and Foxworthy et al. (1998). A review of post-construction

boring logs in the area adjacent to the strong motion arrays at Berth 404 indicates that the SPT penetration resistances of the sand portions of the fill vary with location due to the cumulative influence of; fines content, method of placement, and deposition above or below water level). In the unimproved fill the 33-percentile $(N_1)_{60}$ above the water level (elevation 15 ft to 0 ft) is roughly 23 blows/ft, while the corresponding value below the water level (elevation 0 ft to -34 ft) is 13 blows/ft, indicative of sand vulnerable to liquefiable at design level ground motions.

2. A thin layer of soft harbor bottom sediments (Unit 1 – Harbor Bottom Sediments).
3. An approximately 15- to 35-ft thick layer of generally fine sand and find sand with silt of alluvial deposition (Unit 2 – Younger Channel Sands).
4. An approximately 15- to 20-ft thick layer of sand with silt or silty fine sand of marine deposition (Unit 3 – Marine Sands).
5. A 30- to 35-ft (maximum) thick sequence of paleochannel infill (Unit 4 – Older Paleochannel Infill) composed of very silty fine sand (Unit 4a) overlying silt and clayey silt.
6. A thick, highly layered (sands, silts, clays) sequence of transgressive marine deposits (Unit 7 – Undifferentiated Deposits).
7. An 80- to 100-ft thick sequence of alluvial fine to medium sand with gravel (Unit 8 – Older Allluvial Deposits) that correlates with the onshore Gaspur Aquifer.

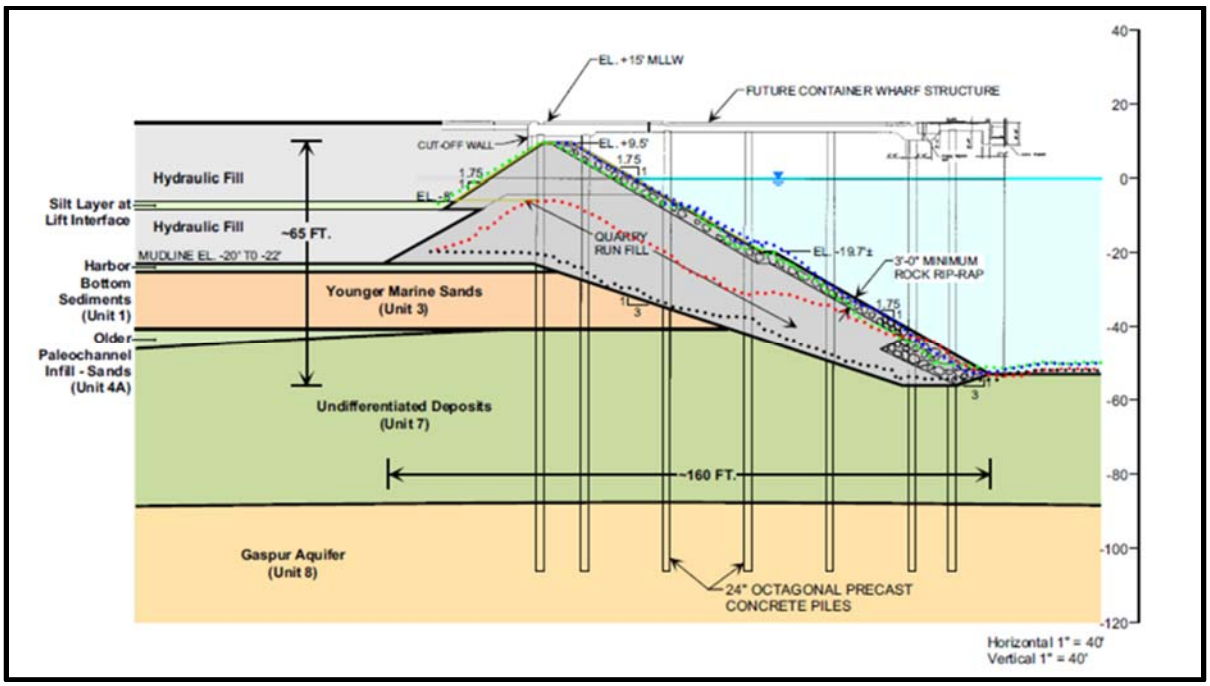

Figure 2: Geologic and structural section at Berth 404, Pier 400, Port of Los Angeles Los Angeles (Fugro West, 2004).

Geophysical Investigation at Berth 404

The research team, in partnership with POLA, CSMIP, and GEOVision, conducted a geophysical investigation using active and passive surface wave techniques (MASW, SASW, and ReMi) to develop the V_s profile across Berth 404 and in close proximity to the CSMIP free-

field strong motion instrument station 14284. The geophysical survey provided useful data for seismic site characterization ($(V_s)_{30} \approx 207$ m/sec) and provided an opportunity to evaluate the V_s profiles through both unimproved fill and zones of fill treated with stone columns. The latter was considered a worthwhile effort for measuring "composite" low-strain behavior of the treated soil mass. The orientation and configuration of the surface wave arrays and results are provided by Dickenson and others (2013).

The results of the surface wave investigation are plotted in Figure 3. The agreement in the V_s profiles through native soils beneath the hydraulic fill layers is very good. The V_s trends in the unimproved and improved fill are highlighted in Figure 9a. As expected the "composite" V_s values are greater in the zone of treated soil, although the difference in the values is only roughly 7% to 12%. It is noted that the ground treatment was implemented in 2 zones adjacent to the waterfront each zone having a different spacing of stone columns and Area Replacement Ratio (ARR). Based on post-construction documentation the approximate average ARR values in the two zones were 14% and 18%, although the diameter of the stone columns was noted to change significantly between the sandy fill and layers of silt-rich soil (Degen et a 2005; Fugro West 2004).

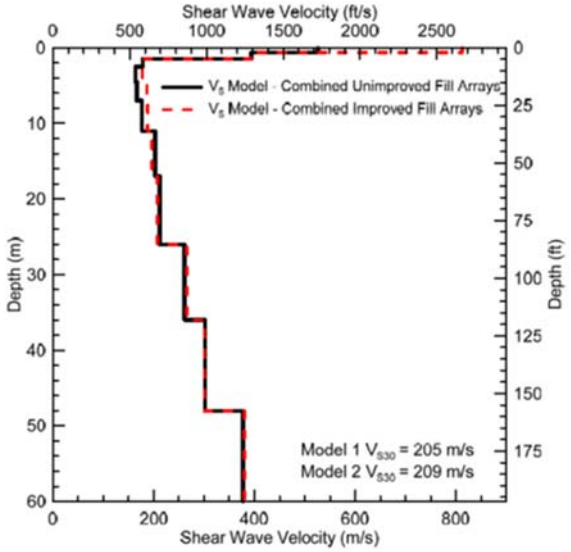

Figure 3: Comparison of shear wave velocity profiles across the Berth 404 site (GEOVision 2013).

Overview of Modeling Parameters and Considerations

The 2D FLAC model has been used for nonlinear, coupled effective stress modeling. The stress-strain behavior of all soil units except for the submerged, untreated sand fill have been modeled using the Mohr-Coulomb constitutive model. The saturated, loose to medium dense sand fill layers (i.e., FILL 3 and FILL 4) have been modeled using the UBCsand model (Beaty 2009). The strength and low-strain stiffness values are provided in Table 1. Several modeling notes are provided as background;

1. The rockfill (quarry run and armor/rip-rap) have been modeled using a stress-dependent friction angle, which provides greater shearing resistance at low confining stress.
2. It is acknowledged that modeling large particles in rockfill dikes, rubble mound structures, and sloping armor layers using the Mohr-Coulomb relationship in a geomechanical continuum model has potentially significant limitations. Issues related to particle size to layer thickness, strength at low confining stress, and the interlocking behavior of the rockfill mass are not well replicated with the simple Mohr-Coulomb model. A practice-oriented model that accounts for the interlocking behavior of rockfill has been developed (Kawamata 2009); however, this material has been modeled using a simplification wherein interlocking is approximated using an artificial, or "pseudo-cohesion" as described by Martin (2005) and Dickenson and McCullough (2006). The shearing resistance of the rockfill has therefore been modeled with both the stress-dependent friction angle and the pseudo-cohesion. The influence of the pseudi-cohesion decreases rapidly with depth as the frictional strength of the rockfill dominates the mass behavior.
3. The stress-strain-strength behavior of the sand fill has been modeled on the basis of the 33-percentile $(N_1)_{60}$ values obtained for post-construction conditions. The percentile value was selected with consideration of mass behavior, generation of excess pore pressure in the submerged, untreated fill, and the variability in N-values (also CPT Qc trends) observed at Berth 404.
4. The static undrained shear strength of the fine-grained soil units was estimated using the stress-normalized relationship for loading in Direct Simple Shear;

   $$(Su)_{DSS} = 0.25 \times (\sigma_v') \times (OCR)^{0.8}$$

   The cyclic shearing resistance mobilized during seismic loading was increased to account for rate effects, as demonstrated in large-scale centrifuge tests by Brandenberg and others (2014). A multiplier of 1.35 was applied to account for rate effects.
5. The zones of sand fill treated with stone columns were modeled using a simple, mass "average" friction value and low-strain stiffness obtained in the surface wave geophysical investigation (with the geophone arrays aligned longitudinally along the zone of improved soil). It is acknowledged that the 2D continuum model cannot replicate the 3D nature of the interaction of stone columns in the layered sand and silt (Rayamajhi et al 2013). The influence of this approximation on the global embankment-wharf behavior can be evaluated by way of sensitivity analyses.

Table 1: General soil properties for modeling

UNIT	φ' (deg)	c' (psf)	S_u (psf)	$(V_s)_{avg}$ (fps)
A.C. Paving & C.M.B.	45	0	n/a	1725 to 2670
Compacted subgrade	45	0	n/a	1290
FILL 1: Emergent sand fill (untreated)	34	0	n/a	560
FILL 1: Emergent sand fill (treated)	40	0	n/a	600
FILL 2: Fill lift interface silt	n/a	n/a	[a]	545
FILL 3: Submerged sand fill (intermediate)	38	0	n/a	545
FILL 4: Submerged sand fill (base)	38	0	n/a	580
Quarry Run Fill (rock)	52[b]	250[c]	n/a	855
Armor/Rip-Rap (rock)	52[b]	250[c]	n/a	715
UNIT 1: Harbor bottom sediment (silt)	n/a	n/a	[a]	600
UNIT 3: Marine sands	38	0	n/a	666
UNIT 4A: Paleochannel fill sand	38	0	n/a	680
UNIT 7: Undifferentiated deposits (fine-grained)	n/a	n/a	[a]	696 to 776
UNIT 8: Gasper aquifer	40	0	n/a	865 to 1120

[a] Su (DSS) = $(1.35)(0.25)(\sigma'_v)(OCR)^{0.8}$

[b] Stress-dependent friction angle (Charles and Watts 1980, Duncan 2004)

[c] Interlocking behavior of rockfill approximated with a "pseudo-cohesion" (Martin 2005, Dickenson and McCullough 2006)

The near-surface, lateral pile-soil response reflects the characteristics of the piles, nature of the inertial loading provided by the wharf deck and contributing loads, the embankment slope, and the nature of the soil and/or rock fill along the upper portion of the pile. Pile embedment through rock armor layers and quarry run fill presents issues related to particle size effects on pile-soil p-y behavior. Physical modeling studies of piles in rock fill have demonstrated the limitations of continuum models for lateral pile response (Boland et al 2001a, 2001b; McCullough 2003; Kawamata 2009). Two straightforward methods have been applied to model the dynamic p-y behavior of piles embedded in rockfill:

1. Kawamata (2009) describes the use of a simple constitutive relationship for the interlocking behavior of rockfill. The method has been calibrated in large-scale tests of instrumented piles in rockfill with very good agreement between computed and observed pile behavior (pile head deflection versus load and trends with depth of pile rotation, deflection, and curvature). The results of the investigation also demonstrated the applicability of practice oriented procedures for developing p-y curves with empirical adjustment. For the piles and rockfill used (POLA Pier 400 simulation) it appears that the use of the API procedures with φ = 38° and a p-multiplier of 2.0 to 3.0 provides results that are considered worthwhile for practical applications.
2. A simple, practice-oriented procedure for modeling pile response in rockfill includes a nominal "pseudo-cohesion" for the rock to account for the individual rock particle interaction with the pile elements (McCullough 2003; Martin 2005; Dickenson and McCullough 2006). The approximation of φ = 45° with an artificial cohesion of 200 to 300 psf provided reasonably good agreement for trends of pile bending moment and deflection with depth. The p-y behavior of the piles (i.e. normal spring stiffness) was modeled using the "pseudo-cohesion" procedure.

The structural detailing of the 24-inch octagonal concrete piles used at Berth 404 varies with row. The common terminology used to describe the piles is “seismic pile” and “non-seismic pile” based on the ductility demand imposed during seismic loading and the necessary design detail for the piles and pile-deck connections. The concept is illustrated in Figure 4 for the wharf configuration at POLA Pier 400. Large scale structural testing of the pile-deck connection (Restrepo et al. 2007, Krier et al. 2008) has been extremely useful for modeling the force-displacement and moment capacity of the piles. The results of a lateral load test on a “seismic pile” are provided in Figure 5. The moment capacity of the piles have been modeled on the basis of the large-scale testing test as; 550 k/ft for seismic piles in Rows F & G, and 400 k/ft for non-seismic piles in Rows A to E.

The mass of the gantry cranes has been incorporated in the modeling. While this investigation has not focused on the dynamic response characteristics of the crane a range of dynamic loads on the wharf representing the cranes has been evaluated. The range of loads used reflects the weight and dimensions of the cranes, as well as the number of cranes used along the wharf during operations. For example, at the time of the 2009 Inglewood Earthquake there were seven gantry cranes working along the vessel Columbine Maersk (approx. 1,200 ft long), which was at Berth 404. The Noell gantry cranes operating at Berth 404 weigh approximately 2,700 kips each and have a width between trolleys of 82 ft. A line load on each rail of roughly 17 k/ft represents a single crane. Alternatively, the wharf has been built with expansion joints spaced at 500-ft intervals. Three cranes can operate along this length of wharf therefore an equivalent line load of roughly 8 k/ft is applied on each rail. Five percent of the crane mass is added to the wharf in the dynamic analysis following the provisions of the POLA seismic code (2010).

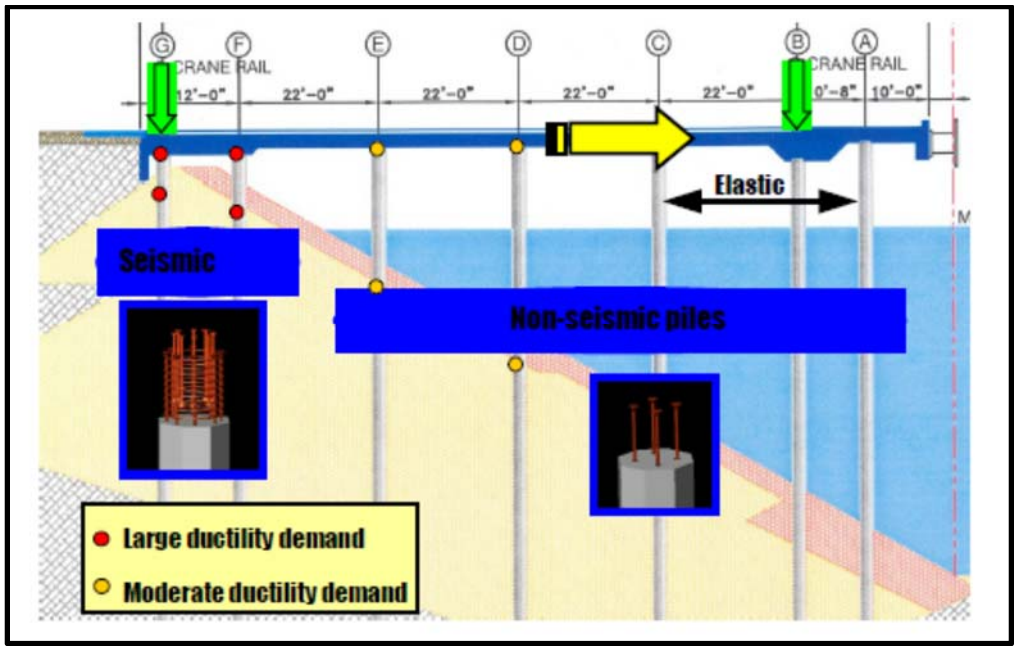

Figure 4: Schematic illustration of a pile-supported container wharf at POLA Pier 400 showing pile types and potential plastic hinge locations (Restrepo et al., 2007).

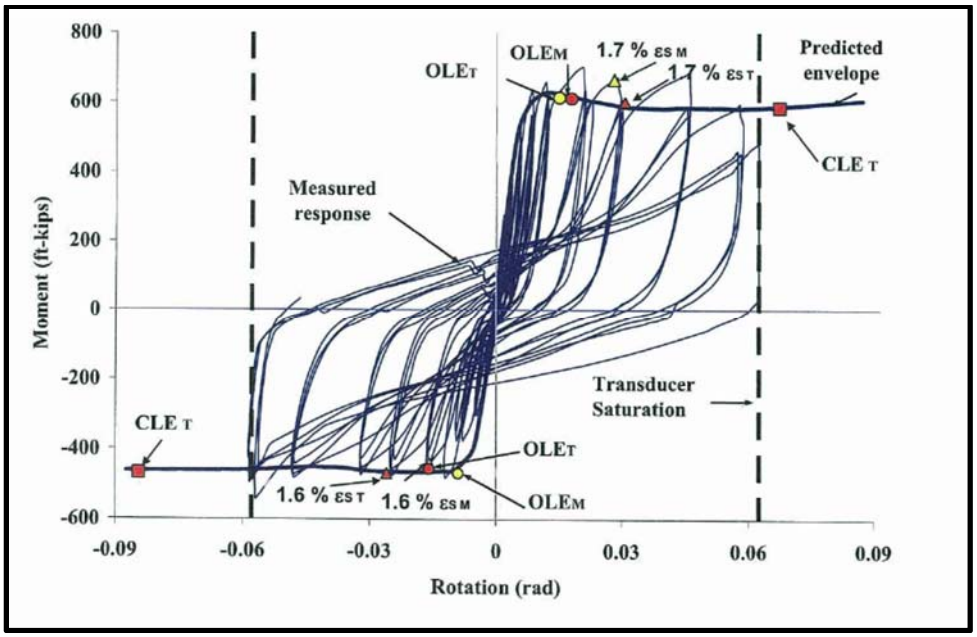

Figure 5: Moment-rotation hysteretic response for a test specimen of a "seismic pile" at POLA Pier 400 (Krier et al. 2008).

Ground Motions

The ground motions used in this investigation reflect the multi-level seismic design requirements provided in the POLA seismic code (2010) and recommendations presented in the "Port-Wide Ground Motion and Palos Verdes Fault Study, Port of Los Angeles, California" (EMI 2006). Three levels of site-specific ground motions are determined for the design of wharf structures as defined in Table 2.

Table 2: Basis for Ground Motions used in Design at the Port of Los Angeles

Earthquake	Probability of Exceedance	Return Period (years)	PGA (g)[a]	Magnitude[c]
Operating Level Earthquake (OLE)	50% in 50 years	72	0.23	6.5
Contingency Level Earthquake (CLE)	10% in 50 years	475	0.52	7.0
Design Earthquake Level (DE)	"Design Earthquake" as defined in ASCE 7-05 Section 11.2[b]			

a Peak Ground Acceleration for "firm ground condition" having Vs = 1,000 ft/sec.

b Refer also to ASCE/COPRI Standard 61-14 Seismic Design of Piers and Wharves (2014).

c Magnitude of the dominant source identified in PSHA deaggregation.

The port-wide ground motion investigation included the development of a collection of ground motions for the firm base condition (V_s 1,000 ft/sec) spectrally-matched to the OLE and CLE Uniform Hazard Spectra. The UHS for various return periods is provided in Figure 6. This investigation has focused on the OLE and CLE ground motion levels, consistent with port design

requirements. The modeling proceeded with baseline analyses performed for lower ground motions levels, specifically;

1. Ground motions recorded at, and in proximity, to the Berth 404 array during the M_w 4.7 May 17, 2009 Inglewood Area Earthquake, and
2. One OLE motion from the EMI (2006) collection (Set 5, 1979 Imperial Valley Earthquake, Calexico Fire Station, Fault Normal).

Subsequent analyses were then performed using a collection of the motion spectrally-matched to the CLE UHS (Figure 6). This included motions from the EMI investigation (2006) and long-duration motions spectrally-matched to the CLE UHS. For the sake of brevity this paper summarizes the results of the modeling for a subset of the motions used in the investigation. The time histories include;

3. Two CLE motions from the EMI (2006) collection (Set 1, 1999 Hector Mine Earthquake, Hector Station, Fault Normal; Set 4, 1999 Duzce Earthquake, Lamont 1059 Station, Fault Normal).
4. Two long-duration motions obtained from subduction zone sources (1985 Michoacan Earthquake, La Union Station, E-W component; 2011 Tohoku Earthquake, TCG005 Station, E-W component).

It must be noted that the subduction zone motions are being used as "seed motions" for evaluating the influence of long-duration motions on the test bed wharf structure (i.e., representative of design and construction at the Port of Los Angeles). Although the long-duration motions have been spectrally-matched to the CLE UHS they are not considered representative of ground motions associated with the regional seismic hazard due to their Significant Durations ($T_{95} - T_5$) and Arias Intensities (La Union 19.6 sec and 8.9 ft/sec; TCG005 70.8 sec and 36.1 ft/sec, respectively). These analyses are therefore conducted to provide an "index" of possible performance at various ground motion levels and not intended to be indicative of predicted performance during an earthquake generating motions at, or exceeding, the CLE at the Port of Los Angeles. Again, the motions are being used to support the primary research goals of; examining the influence of long-duration motions on inertial and kinematic loading, and evaluating the relationship between ground motion characteristics across a broad range of motions with damage thresholds for a pile supported wharf.

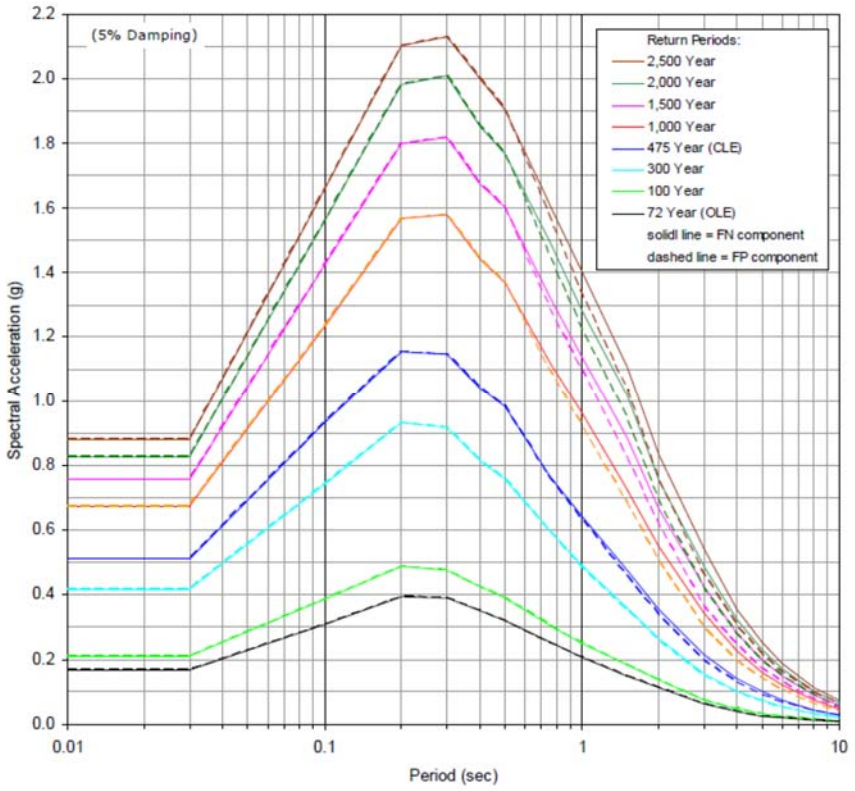

Figure 6: Comparison of firm-ground UHS for various return periods (EMI 2006).

Summary of Modeling Results

The FLAC model geometry is provided in Figure 7. The baseline analyses at lower ground motion levels provided very useful calibration of the model. The OLE analysis resulted a maximum ground displacement of 0.7 ft, with equivalent displacement of the piles and wharf deck. No plastic hinge development in any of the piles was indicated in the analysis.

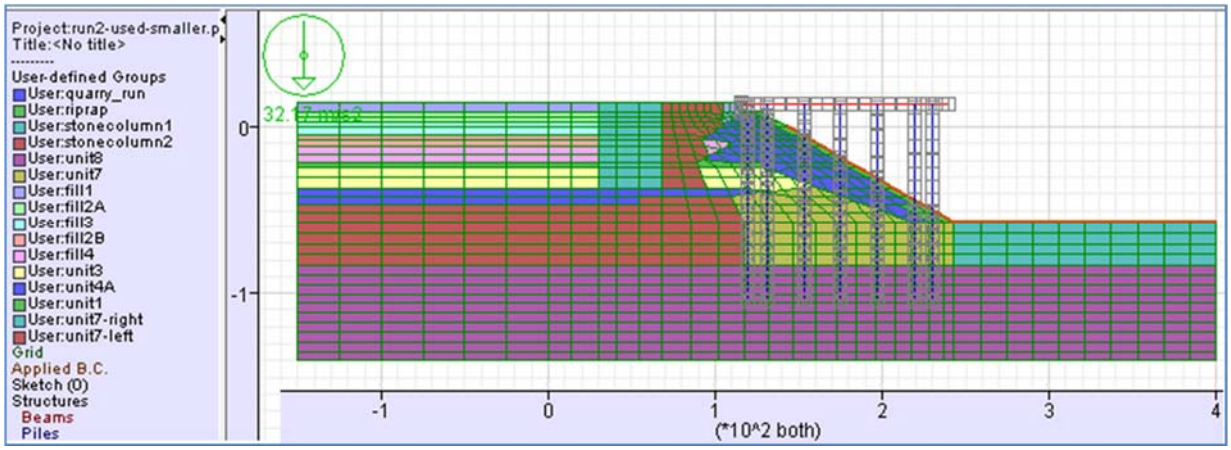

Figure 7: FLAC model geometry for POLA Berth 404 (Pier 400).

The analyses performed for CLE motions resulted in permanent deformations of the rock dike and wharf ranging from 2.3 ft to 3.3 ft. The computed ground deformation pattern is illustrated in Figure 8. The slope movement is largely associated with shear band development in the undifferentiated fine-grained deposits (Unit 7) underlying the rock fill. The localization of deformation at the top and bottom of Unit 7 has resulted in greater displacement demand within several pile diameters of the interfaces and the formation of plastic hinge development at these elevations, as illustrated in Figure 9. The location and extent of the pile hinge development was similar for both CLE analyses. The timing of the pile hinge development can be most directly linked to the concurrent, progressive increase in permanent horizontal displacement. These trends are plotted in Figure 10. The displacement time histories (Figure 10b) of two soil nodes correspond to; (i) a node at ground surface and approximately 30 ft behind the stone column improved zone, and (ii) a soil node located approximately 25 ft below the ground surface and directly behind the rock dike.

It is important to note that the pile moment development adjacent to the pile-deck connection is related to both the inertial loading and the displacement demand (pile head rotation), although this two components of loading do not act in phase with each other. The computational results demonstrate that the progressive increase in moment is closely related to the cumulative increase in the horizontal soil movement. The relative influence of the transient inertial loading and cumulative soil displacement for pile moments in the Row G “seismic pile” is illustrated in Figure 11.

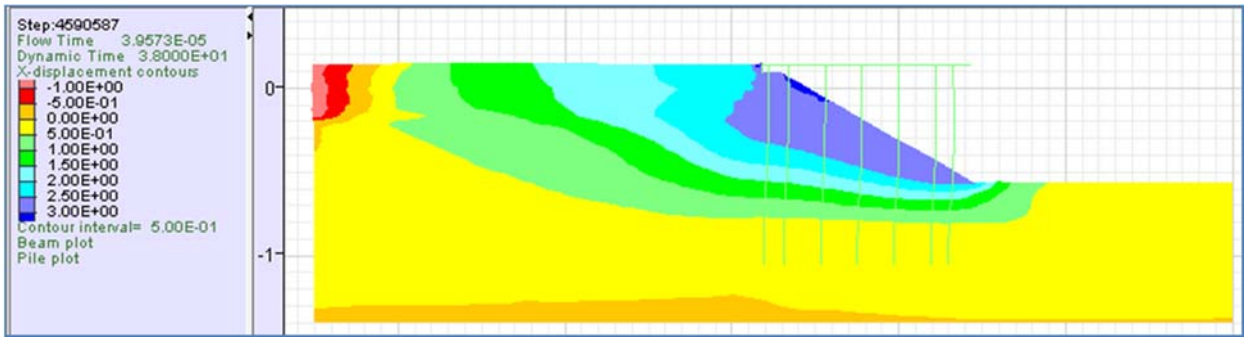

Figure 8: Horizontal displacement contour at the end of shaking using the CLE Set 1 motion (Units of ft).

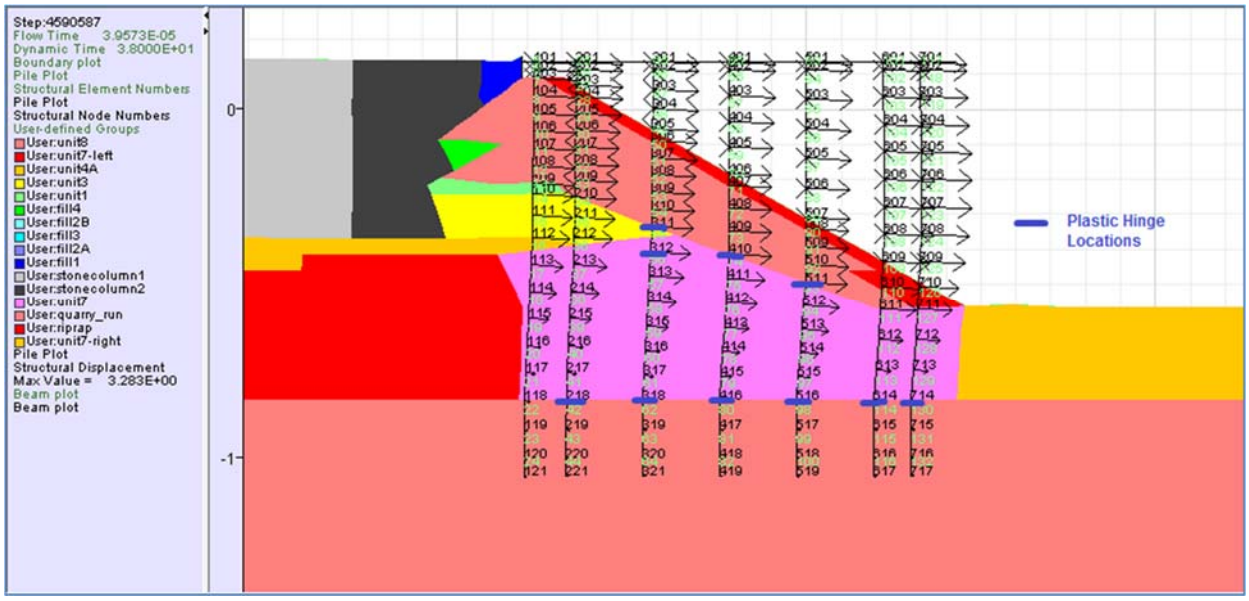

Figure 9: Location of plastic hinges in piles due to CLE motions (note: the black numbers represent the pile node numbers, and light green numbers represent the pile element numbers).

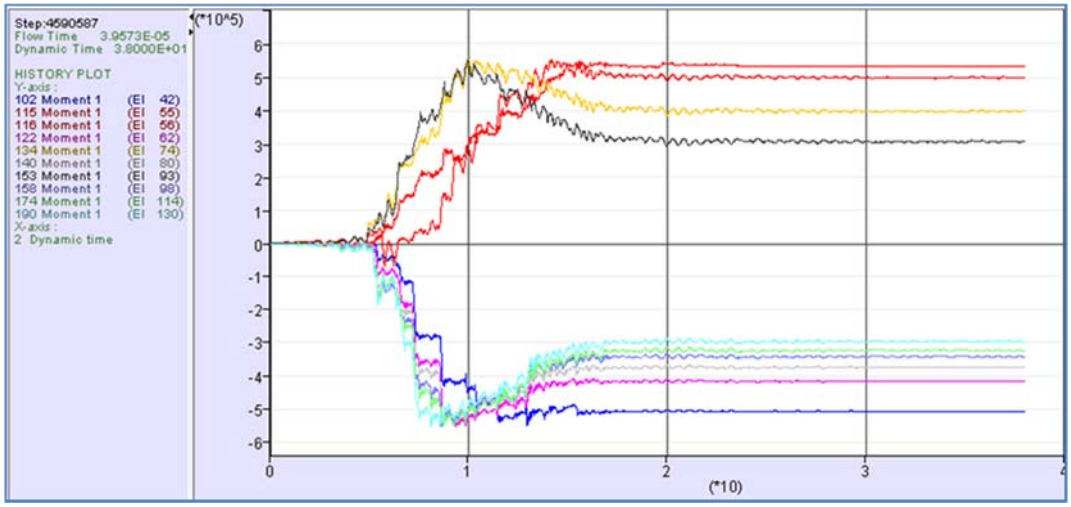

Figure 10a: Moment time history illustrating the occurrence of the plastic hinges in piles during a CLE motion. (X-coordinate: Second; Y-coordinate: Moment in lb-ft)

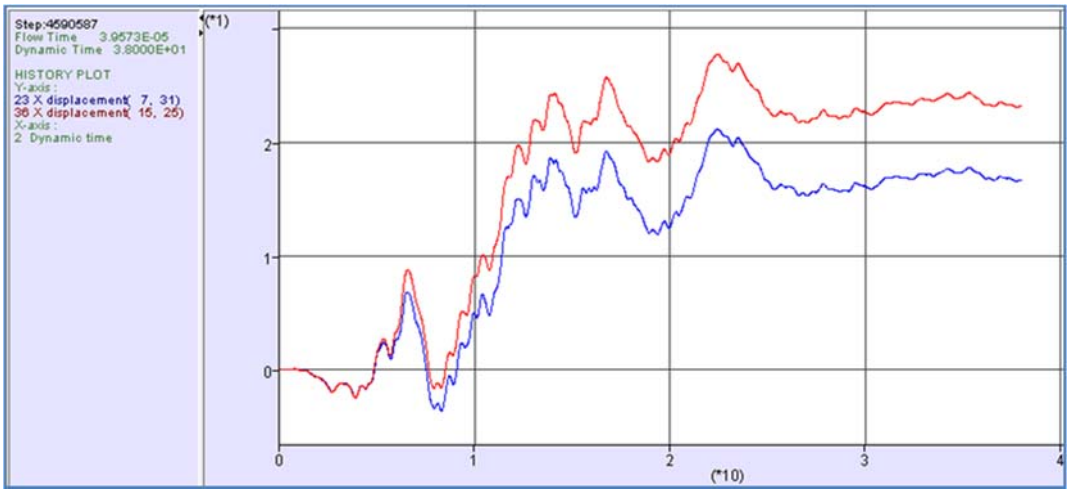

Figure 10b: Time history of horizontal soil displacement due to a CLE motion. (X-coordinate: Second; Y-coordinate: ft)

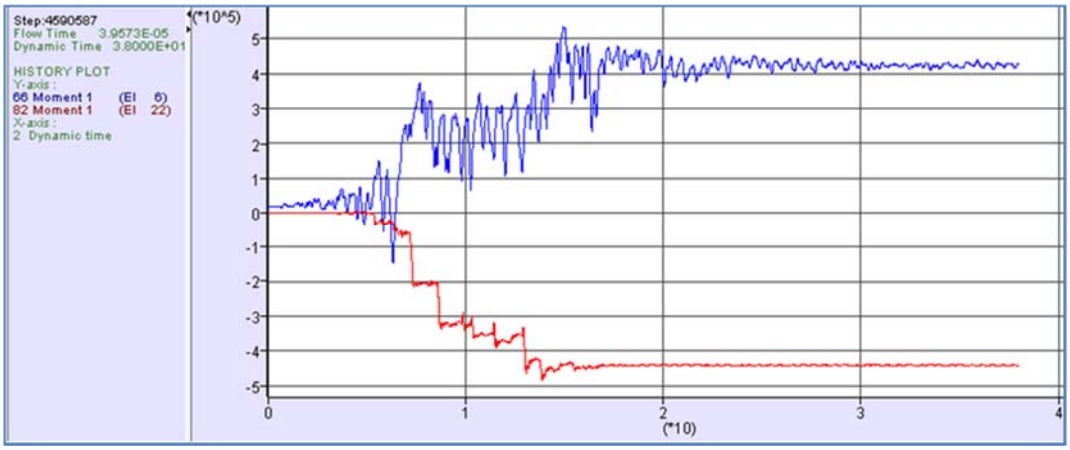

Figure 11: Time history of pile moment in Row G at the pile-deck connection and at the bottom elevation of Unit 7. (Units: ft-lb, sec; blue line is moment at pile-deck connection; red line is moment at bottom elevation of Unit 7)

The analyses performed for long-duration motions (spectrally-matched to the CLE UHS) resulted in permanent deformations of the rock dike ranging from 3.3 ft to 7.0 ft, for the La Union and TCG005 motions, respectively. At 7 ft of displacement the analysis terminated due to excessive deformation and numerical instability. In both models the permanent pile and deck displacement was roughly 85% to 90% that of the global slope movement. The moment development, extent and location of plastic hinges, and permanent deformations computed using the La Union time history was quite similar to the results of the CLE Set 1 analysis. In this case the relatively small increase in Significant Duration and Arias Intensity was not sufficient to induce additional ground deformations and pile damage. Conversely, the TCG005 motion (which is considered an extreme case) resulted in considerably more damage to the piles. It is interesting to note that much of the damage was experienced in the "non-seismic" piles due to ground deformation at layer interfaces, and that the unsupported lengths of the piles remain undamaged.

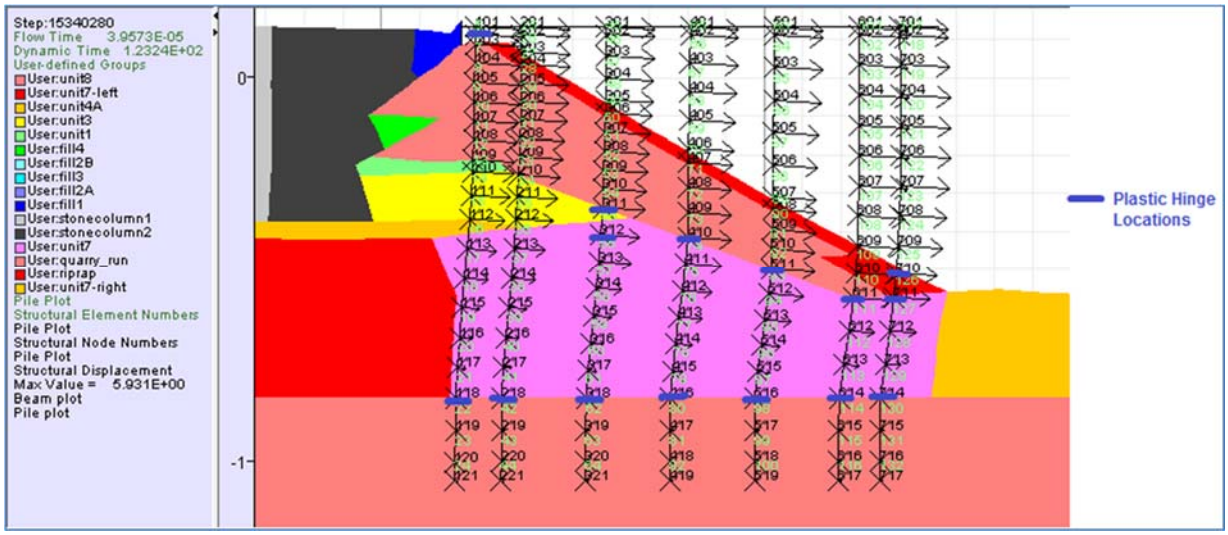

Figure 12: Location of plastic hinges in piles due to a long-duration, CLE motion.

Conclusions

This project is examining the effectiveness of current seismic design codes and performance-based provisions (ASCE/COPRI Standard 61-14, 2014; CSLC MOTEMS, 2010; POLA, 2010; POLB, 2012) for achieving the defined performance requirements for large magnitude earthquakes that generate long-duration ground motions. The topic is important because: (a) recent experience demonstrates that loss of serviceability at port terminals is strongly correlated with permanent ground deformations, and (b) long-duration ground motions have much greater potential for generating damaging wharf and embankment deformations at lower force levels relative to stronger, but brief, seismic loading. Several practical observations and considerations have been made regarding 2D numerical modeling of wharf structures, including:

1. The 2D geomechanical model, using practice-oriented procedures and approximations, have been demonstrated to provide representative seismically-induced permanent deformations, accelerations, and excess pore pressure generation for the low- to moderate-levels of shaking experienced in the validations performed in this investigation (Dickenson et al. 2013).
2. Pertinent aspects of the cyclic lateral behavior of piles in sloping rock fill can be well modeled using a 2D continuum model provided that following considerations are made;
   a. The interlocking nature of the rock fill is accounted for in the model.
   b. The influence of rock fill size on lateral pile behavior (scale effects) is modeled.
   c. The difference between upslope and downslope SSI spring stiffness (p-y behavior) is accounted for in the model.
3. Specific aspects of analysis that warrant consideration for long-duration motions include; (a) fatigue, plastic hinge development, and hinge softening models for the post-yield hysteretic behavior in both the “seismic” and “non-seismic” piles, (b) stress concentrations at pile-wharf deck connection, and (c) patterns of deformation in the rockfill embankment and foundations soils.

4. It is clear that large pile moments develop at depth due to permanent deformation even at moderate soil displacement (≈ 1.0 ft). These pile moments are only predicted through the use of analysis methods that have the capability to model the global wharf-embankment-foundation system.
5. As has been demonstrated in numerous applications involving pile foundations the relative contributions of the inertial loading and kinematic loading to the total demand on structural elements is a complex function of; the characteristics of the time history, timing and pattern of ground deformations, and structural response characteristics. These two primary modes of loading are not in phase and attempts to assign weighting factors to determine the total load should be used with great caution.

The following limitations in the application of 2D continuum models and avenues for continuing investigation have been identified;

1. Limitations in structural characterization due to the pile segment length in the model and plastic hinge length required for assessing curvature and loads at the pile-deck conection.
2. Accurate characterization of pile-deck connection in the model. The model segment should optimally be a fraction of the pile diameter, which is computationally difficult for the continuum model.
3. Hysteretic models should incorporate both; (i) strength and stiffness deterioration of the piles, and (i) pile-soil interaction at large deflections.
4. The data from the surface wave investigation is being evaluated to determine the possible influence of geophysical modeling assumptions (plane waves) and 3D nature of the stone column improvement on the "composite" V_s values provide. This is a valuable data set that is also being used to assess strain-compatibility concepts as applied for the dynamic behavior of stone column treated soils. Modeling the mass behavior in 2D plane-strain of a zone of sand treated with vibrocompaction and or stone columns requires gross approximation that warrants additional refinement.

Acknowledgements

The authors gratefully acknowledge the significant and on-going contributions made by the following individuals. Collectively, these individuals have provided technical documentation, access to projects archives, acceleration time histories, and research results pertinent to the project. The research team has benefitted from active communication addressing nuances of the analysis and design, construction, and post-construction history at the project sites.

Tony Gioiello, Peter Yin and Hugo Cisneros; Port of Los Angeles
Matt Pollard, Cornelia Dean and Danya Pollard; Fugro West, Inc. (Ventura, CA)
Imee Osantowski and Steve Low; Port of Oakland
Tony Martin; GEOVision (Corona, CA)
Nason McCullough; CH2M Hill (Corvallis, OR)
Arul Arulmoli; Earth Mechanics, Inc. (Fountain Valley, CA)
Luke Leffingwell; APM Terminals Los Angeles
Moh Huang, Shirley Rowley and Tony Shakal; CSMIP (Sacramento, CA)
Dawn Lehman; University of Washington (Seattle, WA)
Jose Restrepo; University of California (San Diego, CA)

References

Arulmoli, K., Martin, G.R., Gasparro, M.G., Shahrestani, S., and Buzzoni, G. (2004). Design of Pile Foundations for Liquefaction-Induced Lateral Spread Displacements, *Proc. Geo-Trans 2004; Geotechnical Engineering for Transportation Projects*, Vol. 2, 1673-1680, ASCE Geotechnical Engineering Special Publication No. 126, July, Los Angeles.

ASCE/COPRI (2014a). Seismic Design of Piers and Wharves, ASCE Standard, prepared by the ASCE Standards Committee on Seismic Design of Piers and Wharves.

ASCE/COPRI (2014b). Tohoku, Japan, Earthquake and Tsunami of 2011; Survey of Port and Harbor Facilities, Northern Region, prepared by the ASCE-COPRI Port and Harbor Facilities Survey Team, ASCE, Reston, VA.

ASCE TCLEE (1998). Seismic Guidelines for Ports, Werner, S. (ed.), TCLEE Ports Lifeline Committee, TCLEE Monograph #12, ASCE, Reston, VA.

Beaty, M. (2009). Summary of UBCSand Constitutive Model, Versions 904a and 904aR, Beaty Engineering, LLC, prepared for the short course *Seismic Deformation Analyses of Embankment Dams considering Liquefaction Effects*, Sept. 22 – 24.

Boland, J.C., Schlechter, S.M., McCullough, N.J., Dickenson, S.E., Kutter, B.L., and Wilson, D.W. (2001a), Data Report: Pile-Supported Wharf Centrifuge Model (SMS02), Dept., Civil, Construction & Environmental Engineering, Oregon State Univ.

Boland, J.C., Schlechter, S.M., McCullough, N.J., Dickenson, S.E., Kutter, B.L., and Wilson, D.W. (2001b), Data Report: Pile-Supported Wharf Centrifuge Model (JCB01), Dept., Civil, Construction & Environmental Engineering, Oregon State Univ.

Brandenberg, S.J., Stewart, J.P., and Afacan, K.B. (2014). Influence of Liquefaction on Earthquake Ground Motions, final report for USGS Award Number G12AP20098.

Center for Engineering Strong Motion Data (CESMD). On-line archive for strong motion data.

POLA Pier 400 Berth 404; **http://www.strongmotioncenter.org/cgi-bin/CESMD/stationhtml.pl?stacode=CE14256&network=CGS**

Charles, J.A., and Watts, K.S. (1980). "The influence of confining pressure on the shear strength of compacted rockfill," Geotechnique, 30(4), 353 – 367.

Chiaramonte, M.M., Arduino, P., Lehman, D.E., and Roeder, C.W. (2011). Seismic Analyses of Conventional and Improved Marginal Wharves, *Jrnl. Earthquake Eng. Struct. Dyn.*, 00; 1 - 19.

Degen, W., Baez, F., and Rose, M. (2005). Dry Bottom Feed Stone Columns at Pier 400, Phase II – An evaluation of CPT-based soil classification before and after treatment, *Proc. US-Japan Workshop "New Applications & Challenging Soils for Ground Improvement Technologies*, September, Kyoto, Japan.

Dickenson, S.E., Yang, S., Schwarm, D., and Rees, M. (2013). "Use of Strong Motion Records to Validate Dynamic SFSI Models for Pile Supported Wharves," *Proc. SMIP13*, California Geological Survey.

Dickenson, S.E. and McCullough, N.J. (2006). "Modeling the Seismic Performance of Pile Supported Foundations for Port and Coastal Infrastructure," Proc. of Seismic Performance and Simulation of Pile Foundations in Liquefied and Laterally Spreading Ground, Boulanger and Tokimatsu (eds.), Geotechnical Specialty Publication No. 145, ASCE, 173-191.

Dodds, A.M., Martin, G.R., Arulmoli, K., Bauleka, W., and Toan, D.V. (2004). "Lifeline Upgrade for a Wharf in Soft Ground," *Proc. Geo-Trans 2004, Geotechnical Engineering for Transportation Projects*, ASCE, Geotechnical Special Publication No. 126, Vol. 2, 1739 – 1746.

Donahue, M.J., Dickenson, S.E., Miller, T.H., and Yim, S.C. (2005). "Implications of the Observed Seismic Performance of a Pile-Supported Wharf for Numerical Modeling," Earthquake Spectra, EERI, 21(3), 617-634.

Duncan, J. M. (2004). "Friction angles for sand, gravel and rockfill," Kenneth L. Lee Memorial Seminar, Long Beach, CA April 28.

Egan, J.A., Hayden, R.F., Scheibel, L.L., Otus, M., and Serventi, G.M. (1992). Seismic repair at Seventh Street Marine Terminal, *Proc. Grouting, Soil Improvement, and Geosynthetics*, ACSE Geotechnical Specialty Publication No. 30, Vol. 2.

Earth Mechanics, Inc. (2006). Port-Wide Ground Motion and Palos Verde Fault Study, Port of Los Angeles, California, Final Report, prepared for the Port of Los Angeles, Project 02-131-11, December, 22.

Foxworthy, J., McNeilan, T., and Alcorn, A. (1998) Interim Pier 400 Landfill Status Report, *Proc. Ports '98*, ASCE, Vol. 1., 551 – 560.

Fugro West (2004). Stone Column Ground Improvement Pier 400 Container Wharf Phase 2, Port of Los Angeles, California, prepared for the Port of Los Angeles, March.

Fugro West, Inc. (2001a). Final Geotechnical Framework Report, Pier 400 Landfill Project, Port of Los Angeles, California, prepared for the Port of Los Angeles, April.

Fugro West (2001b). Geotechnical Data Report Pier 400, Stage 2, Post-Fill Investigation, Port of Los Angeles, prepared for the City of Los Angeles, Harbor Department, July.

Fugro West (2001c). Geotechnical Study Pier 400 Container Wharf Phase 2, Port of Los Angeles, California, prepared for the Port of Los Angeles, November.

GEOVision (2013). Report Surface Wave Measurements, Port of Los Angeles, Pier 400, Berth 404, Los Angeles County, California, prepared for New Albion Geotechnical, Inc., Report 13201-01, August 5.

Kawamata, Y. (2009). Seismic Performance of Pile-supported Container Wharf Structures in Rockfill, Ph.D. dissertation, School of Civil & Construction Engineering, Oregon State University, Corvallis, Oregon.

Krier, C.J., Restrepo, J.I., Blandon, C.A. (2008). Seismic Testing of Full-Scale Precast Prestressed Pile to Deck Connections, UCSD Structural Systems Research Project, Report No. SSRP-06/26, Univ. of California, San Diego, Dept. of Structural Engineering, prepared for the Port of Los Angeles, January.

Lehman, D.E., Roeder, C., Stringer, S.J., Jellin, A. (2013). Seismic performance of improved pile-to-wharf deck connections, *PCI Jrnl.*, Summer, 62-80.

Martin, G. (2005). "Port of Los Angeles Seismic Code: Presentation on Geotechnical Aspects," *Proc. POLA Container Wharf Seismic Code Workshop*, Los Angeles, September 13.

McCullough, N.J. (2003). The Seismic Geotechnical Modeling, Performance, and Analysis of Pile-Supported Wharves, Ph.D. dissertation, Dept, of Civil Engineering, Oregon State University, Corvallis, Oregon.

McCullough N. and Dickenson, S. (2004). The Behavior of Piles in Sloping Rock Fill at Marginal Wharves, *Proc. Ports 2004*, ASCE, May, Houston, TX.

Moriwaki, Y., Tan, P., and Choi, Y. (2005). Nonlinear analyses for design of piles in liquefying soils at port facilities, *Proc. of Seismic Performance and Simulation of Pile Foundations in Liquefied and Laterally Spreading Ground*, Boulanger and Tokimatsu (eds.), Geotechnical Specialty Publication No. 145, ASCE, 192-1203.

PIANC WG 34 (2001). Seismic Design Guidelines for Port Structures, Iai, S. (ed.), Working Group #34, International Navigation Association (PIANC), A.A. Balkema Publishers, 474 p.

POLA (2002). Pier 400 Container Wharf Phase II – Berths 404-406, Record Set, Stone Column Layout – Bents 200 to 204 (Drawing SC-4), prepared by City of Los Angeles, Harbor Department, Engineering & Construction Division.

POLA (2010). The Port of Los Angeles Code for Seismic Design, Upgrade and Repair of Container Wharves (POLA Seismic Code 2010), City of Los Angeles Harbor Department.

POLB (2012). Port of Long Beach Wharf Design Criteria, Version 3.0 (February).

Priestley, M.J.N. (2000). Pier 400 Strength and Ductility of Wharf Piles, prepared for the Port of Los Angeles, Report #00/01, August.

Rayamajhi, D., Nguyen, T.V., Ashford, S.A., Boulanger, R.W., Lu, J., Elgamal, A., and Shao, L. (2013). Numerical Study of Shear Stress Distribution for Discrete Columns in Liquefiable Soils, *Jrnl. Geotechnical and Geoenvironmental Engineering*, ASCE, DOI: 10.1061/(ASCE)GT.1943-5606.0000970.

Restrepo, J.I., Yin, P., Jaradat, O.A., and Weismair, M. (2007) Performance of New Pile-Deck Connections Under Earthquakes, *Proc. Ports 2007*, ASCE, San Diego, CA.

Roth, W.H. and Dawson (2003). Analyzing the Seismic Performance of Wharves, Part 2: SSI Analysis with Non-Linear, Effective-Stress Soil Models, *Proc. TCLEE 2003: 6th US Conference & Workshop on Lifeline Earthquake Engineering*, Long Beach, CA.

Roth, W.H., Dawson, E.M., Mehrain, M., and Sayegh, A. (2003). Analyzing the Seismic Performance of Wharves, Part 1: Structural-Engineering Approach, *Proc. TCLEE 2003: 6th US Conference & Workshop on Lifeline Earthquake Engineering*, Long Beach, CA.

Shafieezadeh, DesRouches, R., Rix, G.J., and Werner, S.D. (2012). Seismic Performance of Pile-Supported Wharf Structures Considering Soil-Structure Interaction in Liquefied Soil, *Earthquake Spectra*, EERI, 28(2), 729-757.

Wang, Z.L., Egan, J., Scheibel, L., and Makdisi, F.I. (2001). Simulation of earthquake performance of a waterfront slope using fully coupled effective stress approach, *Proc. 2nd Intern. FLAC Symposium*, Lyon, France, October, 100-108.

Weismair, M., Shahrestani, S., Lim, A., Priestley, M.J.M., and Lam, I.P. (2001). Seismic Design of Port of Los Angeles Pier 400 Container Wharf, *Proc. Ports '01*, ASCE

Yan, L., Arulmoli, K., Weismair, M., Aliviado, R., and Lam, I.P. (2004). Seismic Soil-Structure Interaction Analyses of an Underwater Bulkhead and Wharf System, *Proc. Geo-Trans 2004; Geotechnical Engineering for Transportation Projects*, Vol. 1, 547-555, ASCE Geotechnical Engineering Special Publication No. 126, July, Los Angeles.

VALIDATION OF FINITE ELEMENT ANALYSIS TECHNIQUES USING LOMA PRIETA RECORDINGS AT LOWER CRYSTAL SPRINGS DAM

Vojislav Cvijanovic, Mark G. Schultz, Ingrid J. Dittmar and William A. Fraser

California Department of Water Resources
Division of Safety of Dams

Abstract

Finite element modeling provides insight into the complex three-dimensional response of hydraulic structures and can heavily influence dam safety decisions. As the state of practice continues to evolve, confidence in results can only be gained once analysis methods have been validated and evaluated using direct measurements of known behavior. This paper focuses on comparing physical recordings of dynamic response to model calculations. The findings presented are intended to demonstrate how finite element analysis methods can capture wave propagation, site response, and structural response when material properties are well defined. The comparisons shown will demonstrate the capability of current modeling techniques to re-create a known earthquake and simulate dynamic response of a dam subject to seismic loading.

Introduction

Lower Crystal Springs Dam is a concrete gravity arch located on San Mateo Creek, approximately three miles west of the City of San Mateo. The structure was originally completed in 1888, and later raised by 30-ft in 1890. The dam was constructed using interlocking blocks and does not contain any contraction joints. It has a height of 149-ft with a crest length of 600-ft, a crest width of 40-ft, and a base width of 176-ft.

In 1906, the dam was subjected to significant seismic loading following rupture of the nearby San Andreas Fault, yet no damage was observed. The dam was also subjected to seismic loading during the 1989 Loma Prieta Earthquake. During this event, a series of instruments located throughout the site measured response at the dam toe, dam crest, left abutment, and a location approximately 550-ft downstream.

The Loma Prieta measurements were used to evaluate the analytical tools and finite element analysis methods typically used in making dam safety decisions. This study focuses on determining whether the current state of practice can accurately re-create the 1989 Loma Prieta Earthquake. Results will focus on comparing calculated and measured responses to assess whether the current state of practice can accurately capture wave propagation through a foundation, wave propagation through a structure, and dam-foundation-reservoir interaction.

Review of Site Geology

Supporting Geologic Studies

For the purpose of this study, a shear wave velocity profile for sandstone beneath the free field strong motion accelerometer (located 550-ft downstream of the dam) was needed. CSMIP records indicated that a Vs30 of 713 m/s was assigned to this instrument based on an estimated Vs30 value typical for Franciscan Sandstone. Although direct measurement of the Vs30 and rock weathering profile beneath the instrument would be ideal, the funding of those measurements was outside the scope of this study. Therefore, an approach which relies on statewide Vs30 databases and a study of the specific geology was utilized.

General Geology and Geomorphology

Lower Crystal Springs Dam is founded on Franciscan Formation, which consists of inclusions or blocks of varying size and rock type within a matrix of sheared shale known as the mélange. The right abutment, left abutment, and much of the terrain in the canyon downstream of the dam consist of a very large greywacke sandstone block. The greywacke sandstone is typically medium to coarse grained, well graded, and often contains interbedded shale and siltstone. The sheared mélange is predominately soft, light to dark gray sheared shale with rock fragments. The dam is located approximately 1,200-ft from the peninsula section of the San Andreas Fault Zone.

Pampeyan (1994) recognizes several Holocene aged units downstream of the dam, including younger alluvium (Qya) and slope wash/ravine fill/colluvium (Qsr). Pampeyan (1994) maps a widespread area of colluvium extending along the base of the right side of the canyon of San Mateo Creek. The colluvium consists of well graded, unconsolidated to moderately consolidated deposits of sand, silt, clay, and rock fragments accumulated by slow downslope movement of weathered rock debris and soil.

The source material for the colluvium is the underlying weathered greywacke sandstone. Rotational slides along the base of the right side of the canyon were observed, indicating thicker accumulations of colluvium. The rotated bases of trees and arcuate scarps along the south slope of the downstream channel provided further evidence of rotational slides developed in the thick colluvium deposits. The limits of the colluvium were confirmed by hummocky terrain clearly visible on the LiDAR image, compared to smooth surface in terrain underlain by in place sandstone. Overlaying the limits of the colluvium as mapped by Pampeyan (1994) and the limits of the hummocky terrain on the LiDAR showed remarkable agreement.

Geology Underlying Strong Motion Instrument

The metal box which housed the now abandoned strong motion instrument located approximately 47-ft (at a bearing of 263°) from the southwest corner of Highway I-280 Bridge Bent 3 (Figure 1). Although this instrument is shown in an area of colluvium on the regionally scaled Pampeyan (1994) map, a moderately weathered massive sandstone outcrop can be observed adjacent to the strong motion instrument. It appears that the immediate area surrounding the strong motion instrument has undergone significant man made modifications associated with the construction of the bridge in the 1960's.

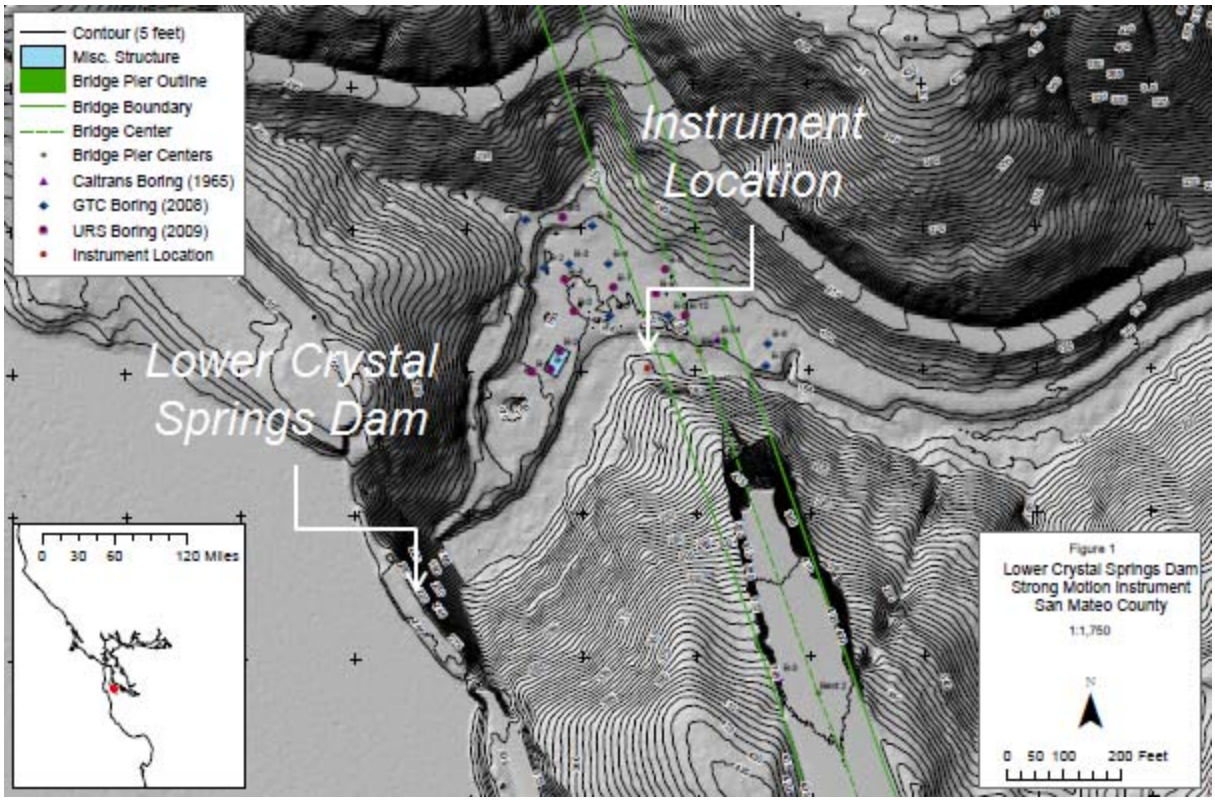

Figure 1. Lower Crystal Springs Dam Site Geology

The excavation was likely made to access a bent construction site, although the remaining evidence is subtle after 50 years. However, comparisons of the pre-bridge and current topography confirmed that approximately 15-ft of excavation has occurred at the instrument site. It is reasonable to assume that the colluvium and highly weathered and fractured sandstone in the immediate area of the instrument was removed for the construction of the bridge bent. When the strong motion instrument was installed in 1978, the site was likely chosen because of the convenient presence of exposed sandstone bedrock in the floor and cutslope of this then fresher excavation. Hand dug shallow subsurface exploration revealed that the instrument is in fact underlain by approximately 6-in of imported gravel underlain by moderately weathered sandstone bedrock.

Shear Wave Velocity Profile Estimation

The development of a shear wave velocity profile estimate at the location of the instrument is based on the assumption that the site possesses a Vs30 of 966 m/s, which is a median value for sites on Franciscan sandstone as determined by a statewide Vs30 database (Wills and Silva, 1998). A modification was then applied to that estimate based on the knowledge that lower velocity materials (which are present at sites considered by Wills and Silva) were removed at this instrument site (Figure 2).

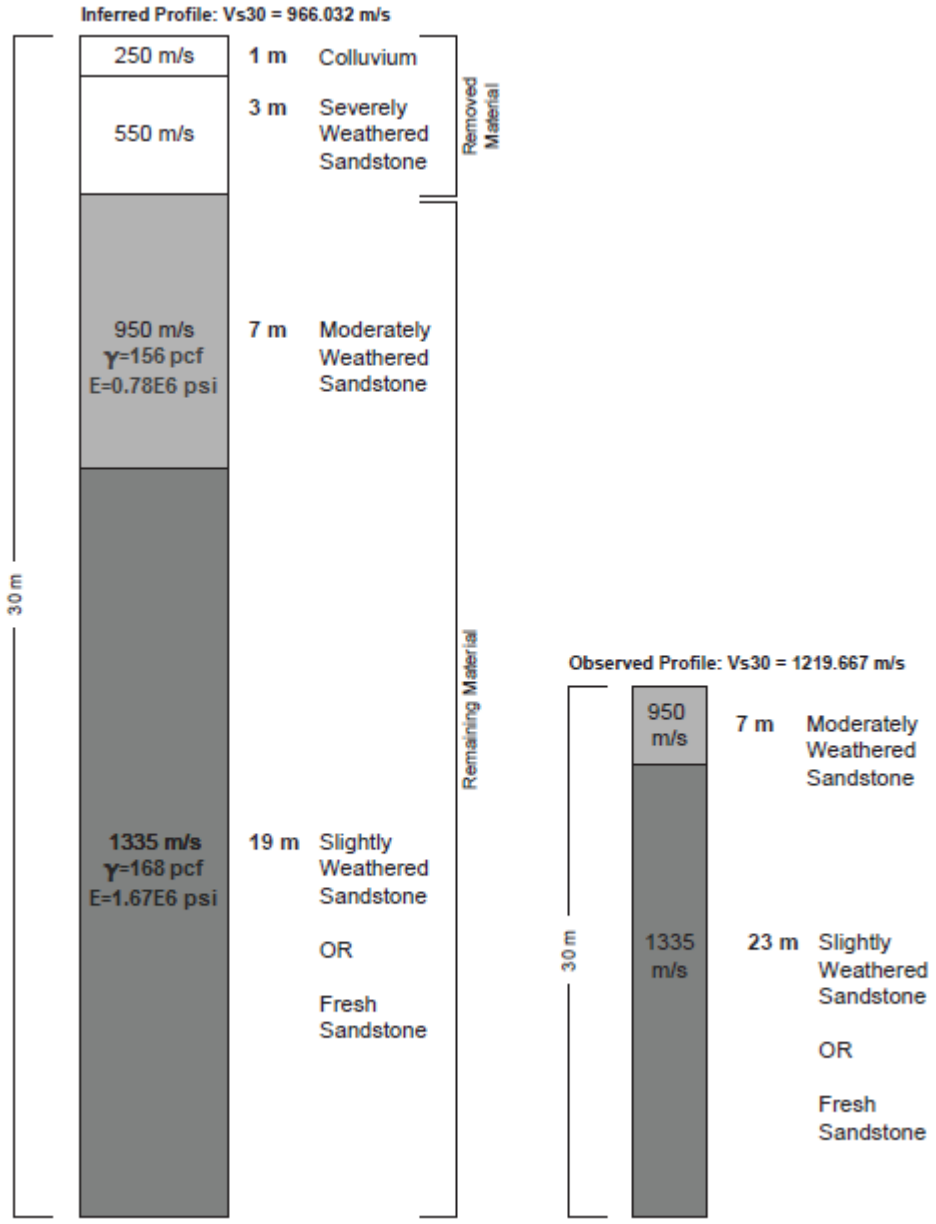

Figure 2. Shear Wave Velocity Profile of Geologic Units Underlying Downstream Instrument

To consider the local site conditions, the available boring logs (drilled during the bridge project and the nearby water distribution facilities) were reviewed to identify a rock weathering profile to a depth of 30 meters. The rock weathering profile contains four units which include surficial soils, severely weathered sandstone, moderately weathered sandstone, and slightly weathered to fresh sandstone.

Using the site weathering profile, the median Vs30 of 966 m/s was distributed across the four units. This produced a "typical" 30 meter weathering and shear wave velocity profile consisting of 1 meter of surficial soil at 250 m/s, 3 meters of severely weathered sandstone at 550 m/s, 7 meters of moderately weathered sandstone at 950 m/s, and 19 meters of slightly weathered/fresh sandstone at 1335 m/s. Since the colluvium and severely weathered sandstone have been removed by the bridge construction exposing moderately weathered rock immediately below the instrument, it is assumed that the downstream instrument site is underlain by the remaining 7 meters of moderately weathered sandstone underlain by slightly weathered to fresh rock (Figure 2).

FEM Model of Lower Crystal Springs Dam

The finite element analysis of Lower Crystal Springs Dam is based on an LS-DYNA model of the dam, foundation, and reservoir. The model consists entirely of elastic eight node solid and fluid elements. Due to adequate contact at the dam-foundation interface, the dam and foundation were modeled as fully merged (coincident nodes along the interface) and therefore, the dam and two foundation regions consist of one continuously uninterrupted mesh. The reservoir however, was modeled as an independent part with sliding contact interfaces applied along the dam-reservoir and foundation-reservoir boundaries. Note that the reservoir model was created to be consistent with the reservoir elevation at the time of the Loma Prieta Earthquake (which corresponds to 95-ft of head).

The dam concrete was modeled using an elastic material with modulus of 3,600 ksi (consistent with 4,000 psi concrete). A nonlinear constitutive material model is often used in typical seismic evaluations. However, one was not considered in this case given the low amplitude of the recorded motion as the concrete does not reach a nonlinear range.

The foundation consists of a two layer model downstream of the dam, which is consistent with the geologic profile previously discussed (slightly weathered sandstone beneath seven meters of moderately weathered sandstone). The material properties assigned to the foundation layers are consistent with estimations presented in Figure 2. Foundation material immediately beneath the dam however, only considers slightly weathered sandstone (Figure 4), as moderately weathered sandstone beneath the dam was removed during construction.

Ground Motion Propagation through a Mass Foundation

Application of ground motion should simulate the upward propagation of waves through a mass foundation. However, because frequency content of the upward propagating wave changes throughout the propagation process, a procedure which produces a free field match requires two independent analyses.

The initial analysis is based on direct application of the target motion at depth. The computed free field accelerations can subsequently be extracted and transformed into the frequency domain ($F_{Computed\ Free\ Field}$). The frequency function of the input is then scaled by a transfer function, which is represented by the frequency function of the target divided by the frequency function of the free field measurements (Eqn. 1).

$$F_{New\ Base\ Input} = \frac{F_{Target}}{F_{Computed\ Free\ Field}} \times F_{Initial\ Base\ Input} \quad (1)$$

The result is a frequency function for a new input ($F_{New\ Base\ Input}$) which can be transformed back into the time domain and applied at depth. Application of the modified record results in a free field calculation which matches the target (Figure 3).

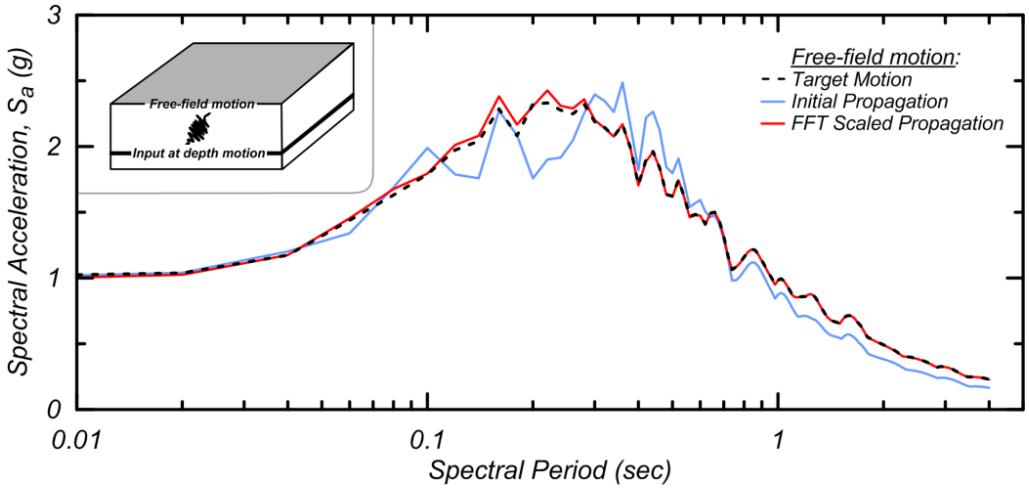

Figure 3. Example of Frequency Function Scaling.

Comparison of Loma Prieta Recordings to Analysis Calculations

The analyses completed are based on application of toe recordings at the dam toe. This decision is attributed to well-defined foundation properties beneath the structure, as moderately weathered material was removed prior to construction. Therefore, foundation uncertainties beneath the dam are limited whereas characterizing foundation material beneath the free field instrument was found to be much more of a challenge given the great deal of uncertainty.

To simulate upward propagation of waves, ground motions could not be directly applied at the toe. Therefore, analyses require developing an at-depth input which could propagate through the foundation and produce toe accelerations that match toe recordings (Figure 5). This procedure is based on the two phase ground motion application technique described above.

The initial analysis is based on the direct application of toe measurements at depth. Motions calculated at the dam toe were then used to scale the frequency function of the initial base input by a transfer function. The transformed motion, when applied at depth, then produces toe accelerations which match measured toe recordings. Once the model has demonstrated that the toe calculations coincide with the recorded toe measurements, calculated accelerations at other locations can be compared to physical measurements (Figure 6).

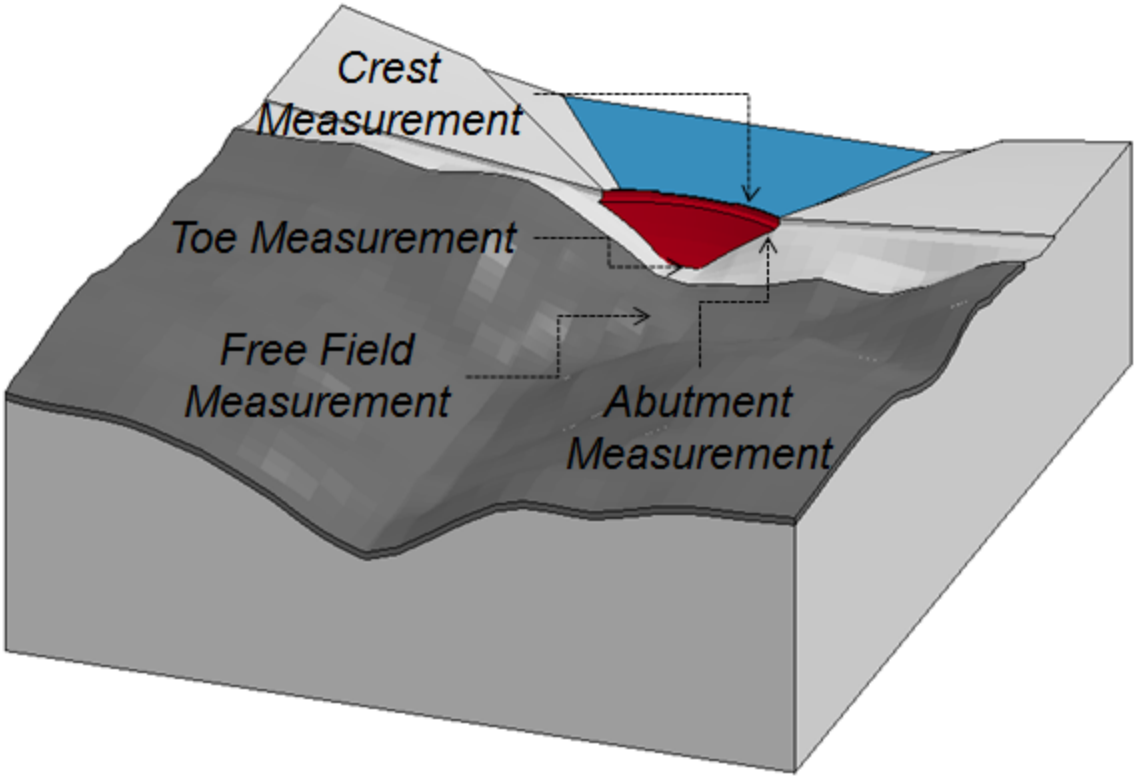

Figure 4. LS-DYNA Model of Lower Crystal Springs Dam.

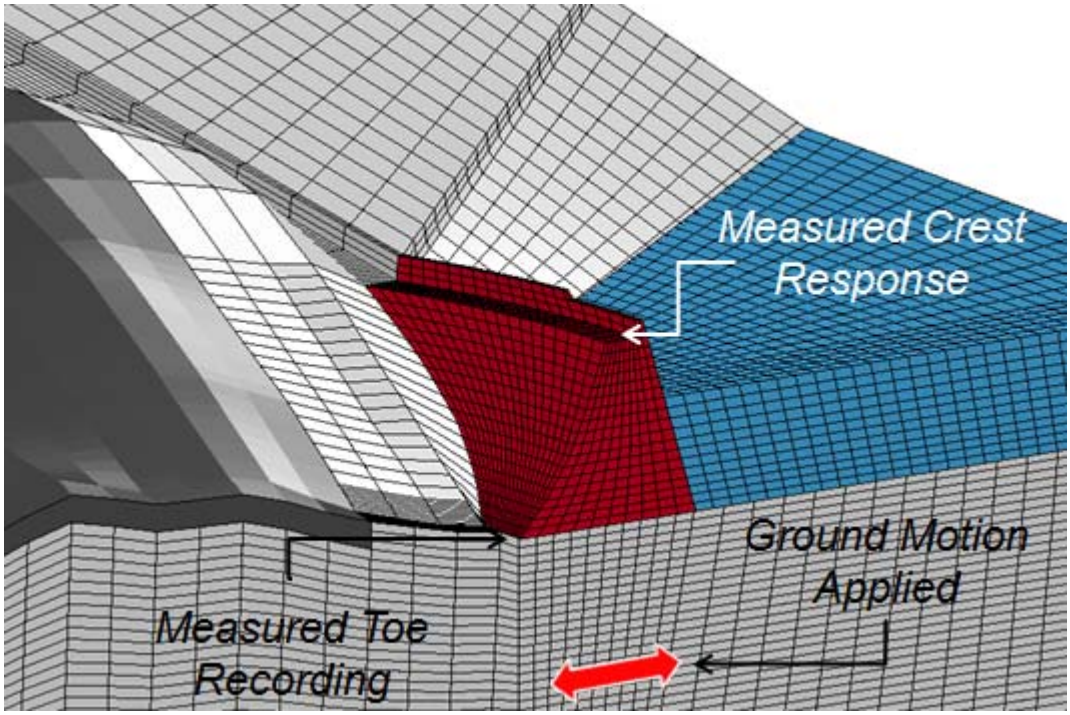

Figure 5. Ground Motion Propagation.

The analysis was found to produce positive results, which demonstrates the model's ability to re-create a recorded earthquake event. A comparison of response at the dam crest produced very favorable results, which implies that the model can accurately capture structural response. This is partially attributed to the well-defined foundation properties beneath structure, as moderately weathered material underlying the dam was removed prior to construction. Therefore, foundation uncertainties are limited and the one layer foundation profile (slightly weathered sandstone) accurately characterizes foundation properties beneath the dam.

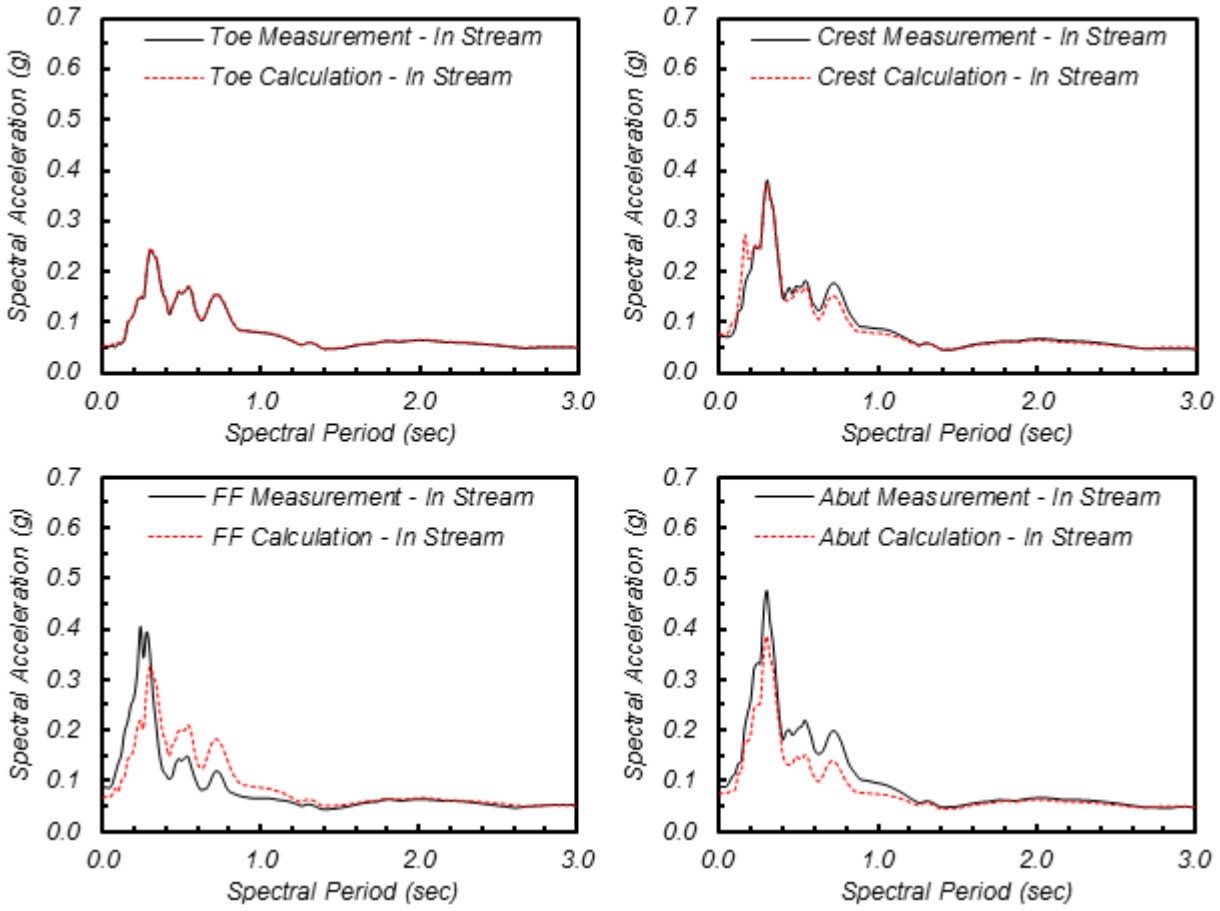

Figure 6. Comparison of Measured and Calculated Response.

Characterizing foundation material beneath the free field instrument however, was found to be much more of a challenge. This profile is based on a best estimate due to the lack of physically measured data. Therefore, the two layer foundation model beneath the free field instrument contains a great deal of uncertainty as the depth and properties of the moderately weathered sandstone are not known. This uncertainty leads to results which do not produce the same level of accuracy.

Because there are no actual shear wave measurements at the site, best estimates of moderately weathered sandstone parameters were given a range of acceptable values. This provides flexibility in evaluating how varying these parameters (within the acceptable range) affects free field response.

In Case 1, the shear wave velocity of the moderately weathered sandstone was reduced to 520 m/s, which is a lower bound stiffness estimate. As expected, amplification in free field response was calculated and results indicate a more accurate match.

In Case 2, the lower bound stiffness was combined with an upper bound moderately weathered layer thickness of 11 meters. This further amplifies response and begins to produce favorable results. Ultimately, results imply that the assumed profile may not be representative of what is present beneath the instrument. Therefore, additional exploration in this region could be helpful in better characterizing the sub-surface conditions and may lead to more accurate free field predictions.

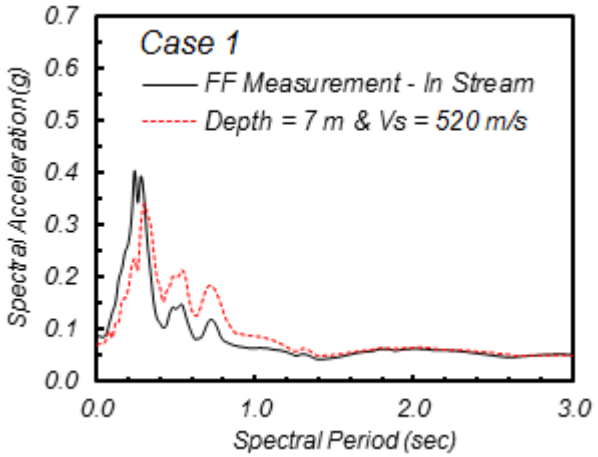

Figure 7. Sensitivity to Moderately Weathered Sandstone Stiffness.

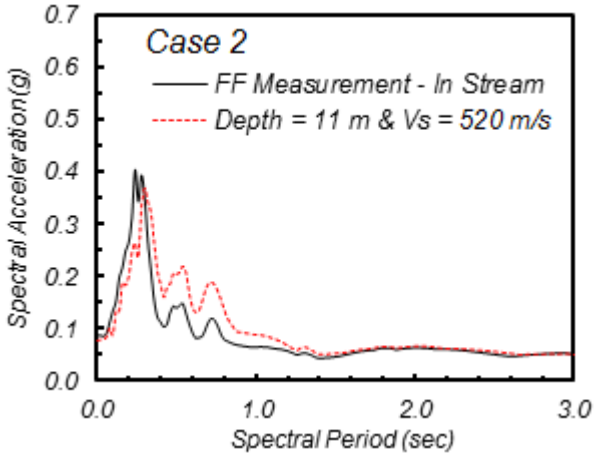

Figure 8. Sensitivity to Moderately Weathered Sandstone Depth.

Another sensitivity study was completed to evaluate how foundation damping affects response. In the previously discussed examples, five percent Rayleigh damping was applied to the structure, foundation, and reservoir. Given the favorable results produced at the dam crest, it is reasonable to conclude that applying five percent damping to the dam and reservoir is appropriate. Applying five percent damping to the foundation however, may not be suitable. Therefore, an analysis was completed to determine how sensitive free field response is to foundation damping.

The model used considers the best estimate shear wave velocity profile presented in Figure 2 and model parameters are consistent with those used in the initial analysis. The exception however, is that Rayleigh damping assigned to the foundation parts has been reduced to two percent (1-10 Hz). Note that significant changes in results were not identified (Figure 9).

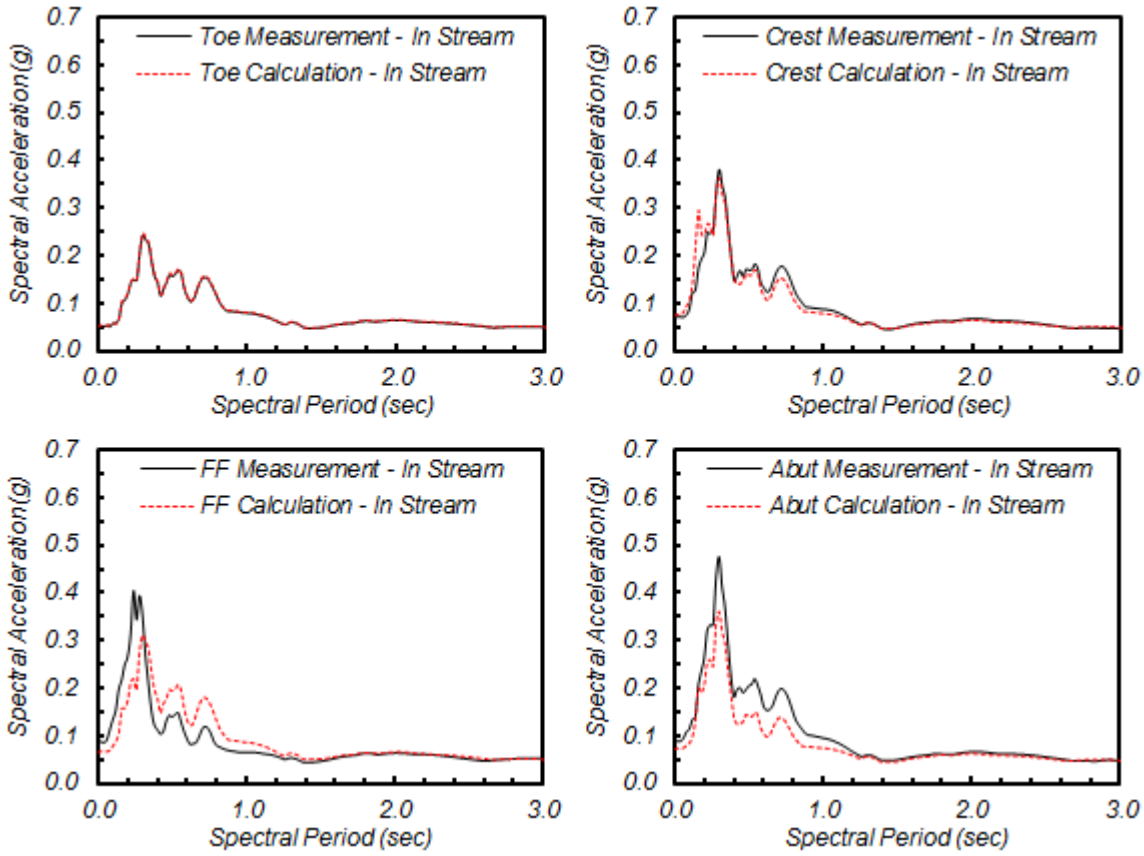

Figure 9. Sensitivity to Reduced Foundation Damping.

A final analysis was completed to evaluate how the model responds to the application of a two-component (in stream and cross canyon) toe record (vertical toe record is not available). For this analysis, five percent damping was applied to all parts and the best estimate shear wave velocity profile (presented in Figure 2) was considered. As shown in Figure 10, the comparison of response at the dam crest still produced favorable results, which implies an accurate representation of structural response.

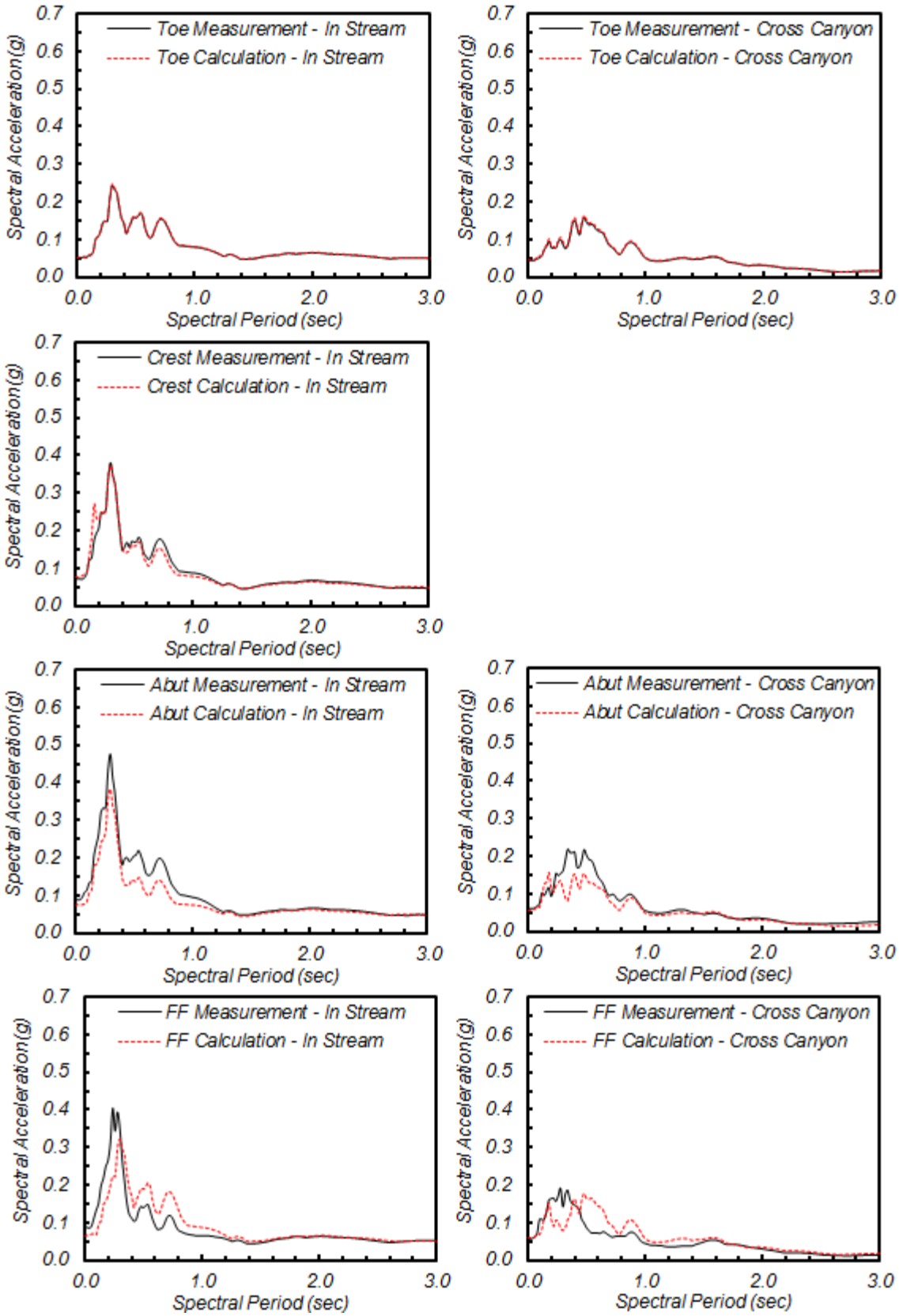

Figure 10. Two Component Ground Motion Application.

Conclusion

Findings presented in this paper are intended to demonstrate how finite element analysis methods can re-create a known earthquake when material properties are well defined. This idea is most clearly demonstrated at the dam crest, where the calculated response is in agreement with values measured during the earthquake. This comparison indicates that the model can accurately capture wave propagation through a foundation, wave propagation through a structure, structural response, and dam-foundation-reservoir interaction given well-defined properties for foundation materials underlying the structure.

In regions where material properties are not as well defined, characterizing foundation material is based on a best estimate with a certain degree of uncertainty. This uncertainty can lead to results which do not produce the same level of accuracy, as demonstrated by the free field comparison. Further exploration of material underlying the free field instrument could lead to more accurate results as demonstrated by this study through the variation of unknown parameters within a reasonable range.

Future efforts to further advance the state of practice will focus on case studies which consider stronger motion measurements. These studies will evaluate whether analytical tools can accurately predict non-linear structural response and behavior.

Acknowledgements

Although this research was supported by the California Department of Water Resources, the views expressed are those of the authors and do not necessarily represent the views of the Department. This study would not be possible without the generous assistance from staff of the San Francisco Public Utilities Commission and the California Strong Motion Instrumentation Program.

References

Fraser, W.A. (2014). Geologic Inspection of Strong Motion Instrument, Lower Crystal Springs Dam. Prepared for the Division of Safety of Dams.

Geotechnical Consultants (2008). Geotechnical Report, Crystal Springs Pump Station, CSSATSUP. Prepared for San Francisco Public Utilities Commission.

McDaniel Engineering Company (1994). As-Built Log of Test Boring – 3”, Earthquake Upgrade, San Mateo Creek Bridge. Prepared for the State of California Department of Transportation.

Pampeyan, E.H. (1994). Geologic map of the Montara Mountain and San Mateo 7.5' quadrangles, San Mateo County, California. U.S. Geological Survey, Miscellaneous Investigations Series Map I-2390, scale 1:24,000.

Prentice, C. (2009). LiDAR and Bathymetry Data Package, San Andreas Fault. Prepared for U.S. Geological Survey.

URS (2009). Geotechnical Investigation Work Plan, Crystal Springs Pump Station, CSSATSUP. Prepared for San Francisco Public Utilities Commission

Wills, C. J., & Silva, W. (1998). Shear-Wave Velocity Characteristics of Geologic Units in California. Earthquake Spectra, 14(3), 533.

LSTC (2007). LS-DYNA Keyword User's Manual, Version 971, Livermore Software Technology Corporation, Inc., Livermore, California.

XYZ Scientific (2006). TrueGrid User's Manual, Version 2.3.0, XYZ Scientific Applications, Inc., Livermore, California.

Schultz, M.G., P. Huynh, and V. Cvijanovic. (2014). Implementing nonlinear analysis of concrete dams and soil-structure interaction under extreme seismic loading. Prepared for United States Society on Dams.

Cvijanovic, V., M. Schultz, and R. Armstrong. (2014). Application of nonlinear analysis methods to hydraulic structures subject to extreme loading conditions. Prepared for United States Society on Dams.

MODELING SENSITIVITY IN COMMONLY USED COMPUTER PROGRAMS – CASE STUDIES OF INSTRUMENTED STEEL MOMENT-FRAME BUILDINGS

Daniel Swensen and Sashi Kunnath

Department of Civil and Environmental Engineering
University of California at Davis

Abstract

There are various nonlinear analysis programs in use today, and an even greater number of modeling choices within and between computer programs. It is essential for engineers to understand the nuances of nonlinear modeling so as to construct a reliable simulation model and analyze its seismic behavior. As a step towards such an understanding, the suitability of three widely used computer programs (SAP2000, Perform3D, and OpenSees) for seismic evaluation are investigated in terms of their response sensitivity to nonlinear modeling choices. Selected results from a set of nonlinear response history analyses of a 9-story steel moment frame building are reported in this paper.

Introduction

This paper presents some findings from a nonlinear sensitivity study of instrumented steel moment frame buildings. The study involved three instrumented steel moment frame buildings of varying height, however only select results from the 9-story building will be highlighted in this paper. The development of the 9-story elastic models in OpenSees, Perform3D, and SAP2000, as well as the subsequent calibration and validation of the models to recorded data is discussed in Swensen and Kunnath (2012). Nonlinear models were developed in OpenSees, Perform3D, and SAP2000 using moment-rotation hinges, moment-curvature hinges, and fiber hinges. Numerous nonlinear response history analyses were performed using both near fault and far fault ground motions. Response sensitivity to various modeling choices, including post-yield stiffness and hinge length, was investigated.

Case Study: 9-Story Steel Moment Frame Building

The building considered in this paper is the Aliso Viejo 9-story office building (CSMIP Station No. 13364). This 9-story office building located in Aliso Viejo, California was designed in 2006 according to the 2001 California Building Code, and constructed in 2008. The building is rectangular in plan with dimensions of approximately 220 ft. x 120 ft. The first floor story height is 17 ft. while the remaining story heights are 13.5 ft. for a total building height of 125 ft. There is a helistop located near the center of the building about 11 ft. above the roof level. Lateral forces are resisted in each direction by steel special moment resisting frames located at the perimeter of the building. The connection used in the moment frames is SSDA's proprietary slotted beam connection. Figure 1 shows the typical floor plan and moment frame elevation of the building.

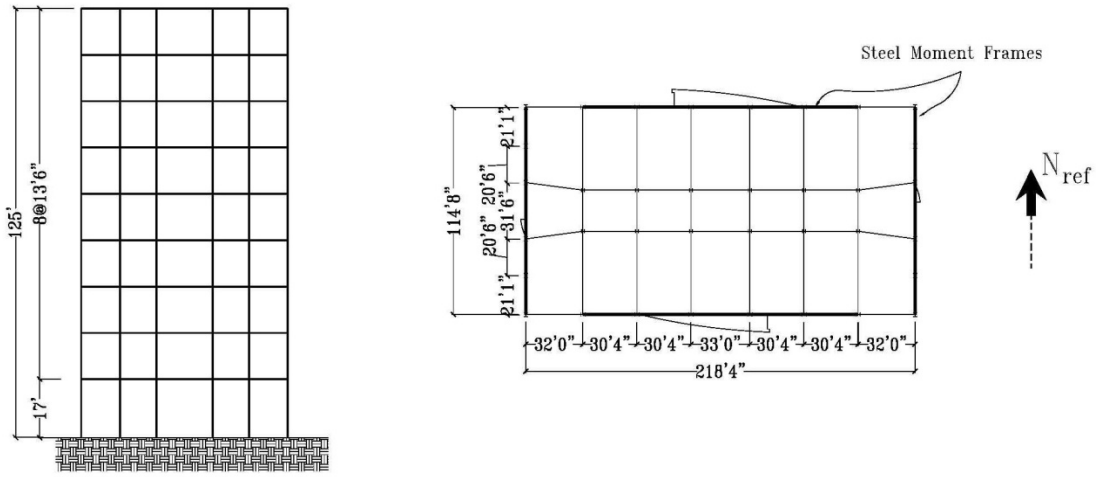

Figure 1: Elevation of typical steel moment frame (N-S Direction) and floor plan of the building

Ground Motion Selection

Seven time histories representing far fault ground motions and seven time histories representing near fault ground motions with forward directivity effects were selected from the PEER-NGA database to be used in performing nonlinear response history analyses of the calibrated SAP2000, Perform-3D, and OpenSEES models of the Aliso Viejo 9-story office building.

The response spectra for the selected motions and the mean spectra for each set are shown in Figure 2. In order to generate a robust set of nonlinear results from the time history analyses it was determined that the intensity for each of the selected ground motions should be sufficient to produce, at a minimum, 2% inter-story drift ratios along the height of the structure. This would guarantee sufficient nonlinearity in the models and make the results of the sensitivity study more meaningful. The intensity of each of the ground motions from the near fault set was sufficient, without scaling, to produce the desired inter-story drift ratios. The set of far fault ground motions however, required some scaling. The scale factor for each of the far fault motions was determined by uniformly scaling each far fault response spectrum to approximately 0.9 g at 2.2 seconds, the first modal period of the models used in the time history analyses.

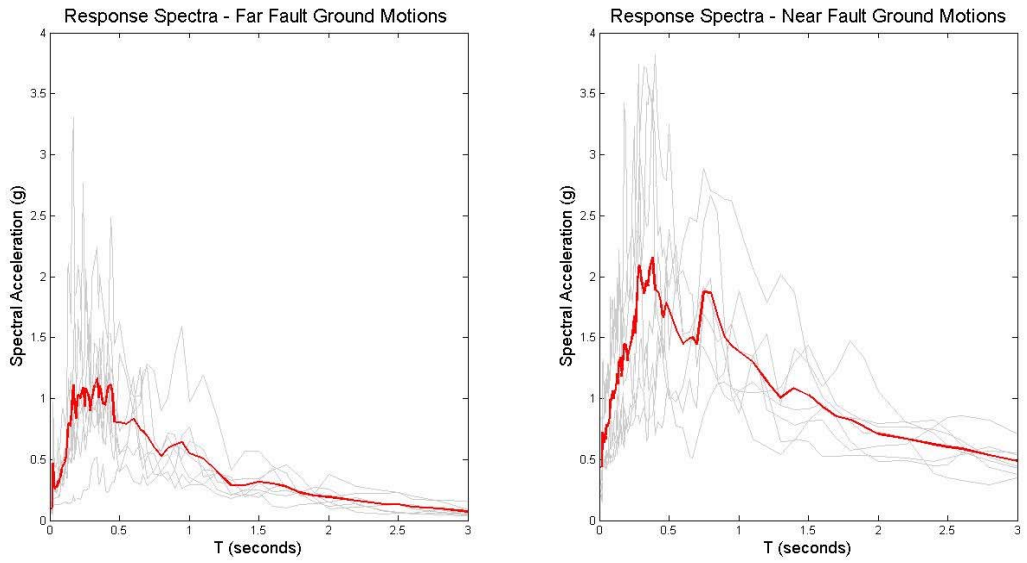

Figure 2: Individual (light lines) and mean spectra (bold line) of selected ground motions.

Nonlinear Simulations: Moment-Rotation Hinge Model

Two dimensional nonlinear models using moment-rotation hinges were completed in OpenSees, Perform3D, and SAP2000. The hinges were located at each end of each beam and column of the moment frame. The moment-rotation relationship for each hinge was assumed to be bilinear with the following variations in post-yield stiffness: 0.05%, 2%, and 5%.

Nonlinear response history analyses using the seven far fault and seven near fault ground motions were performed on a total of nine different moment-rotation models: three models from each of the three software, reflecting the variations in post-yield stiffness mentioned above. The following assumptions were made for the nonlinear response history analyses for each of the nine models:

- No dummy columns included
- Include the effects of P-delta
- 5% Rayleigh damping anchored at the first and third modes and proportional to mass and *initial* stiffness (no modal damping)

The dummy columns represent stiffness contributed by various non-structural components which is assumed effective at only low amplitude shaking; as the intention is to shake these models well into the nonlinear range it makes sense to exclude the dummy columns from the nonlinear models.

The equivalent gravity frame originally included in the elastic model was included in the nonlinear time history analyses, and a P-delta geometric transformation was used for the columns in both the moment frame and equivalent gravity frame for each of the models. Thus, the effects of P-delta should be sufficiently captured in the results of the nonlinear response history analyses.

For each of the nonlinear models the expected yield stress of the steel wide flange framing (55 ksi) was used instead of the design yield stress (50 ksi) for establishing the associated strengths of the force-deformation relationships. In the equivalent gravity frames for each of these models, moment-rotation hinges were used at each end of the gravity beams with an assumed elastic-perfectly plastic force-deformation relationship. The plastic moment capacities for these partially-rigid connections were determined in a manner similar to one outlined in Foutch and Yun (2002).

A comparison of the computed peak inter-story drift ratios of each model using 0.05% post-yield stiffness from the set of seven near fault ground motions and the set of seven far fault ground motions can be seen in Figure 3 and Figure 4, respectively. Figure 3 shows that each model produced very similar results with some minor variations, most notably in GM #3 and GM #4. There is greater dispersion in the far fault ground motion results, especially with SAP2000, as can be seen in Figure 4.

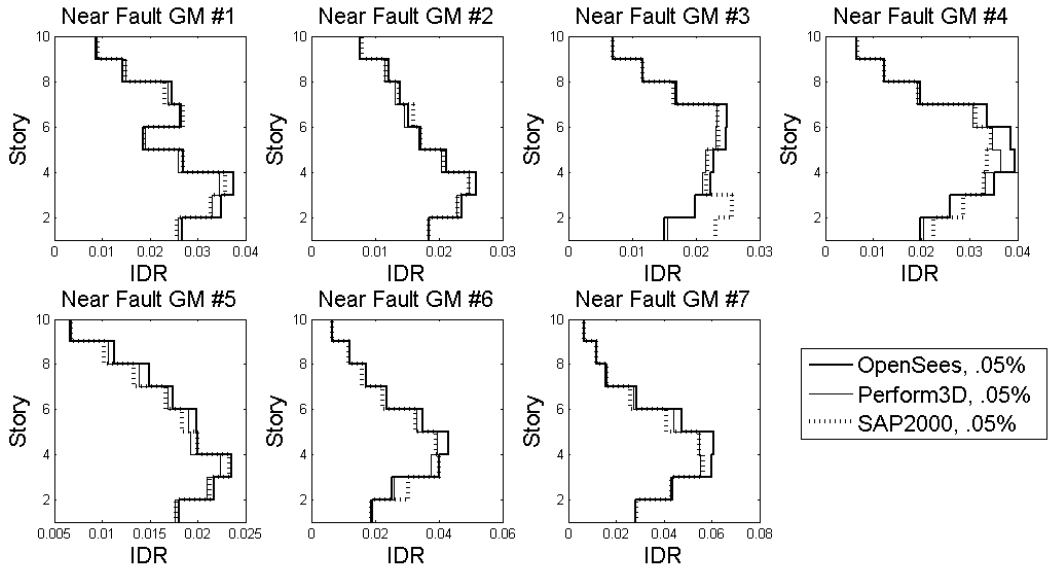

Figure 3: Comparison of computed peak inter-story drift ratios using moment-rotation hinges with 0.05% post-yield stiffness in OpenSees, Perform3D and SAP2000 from seven near fault ground motions with forward directivity effects

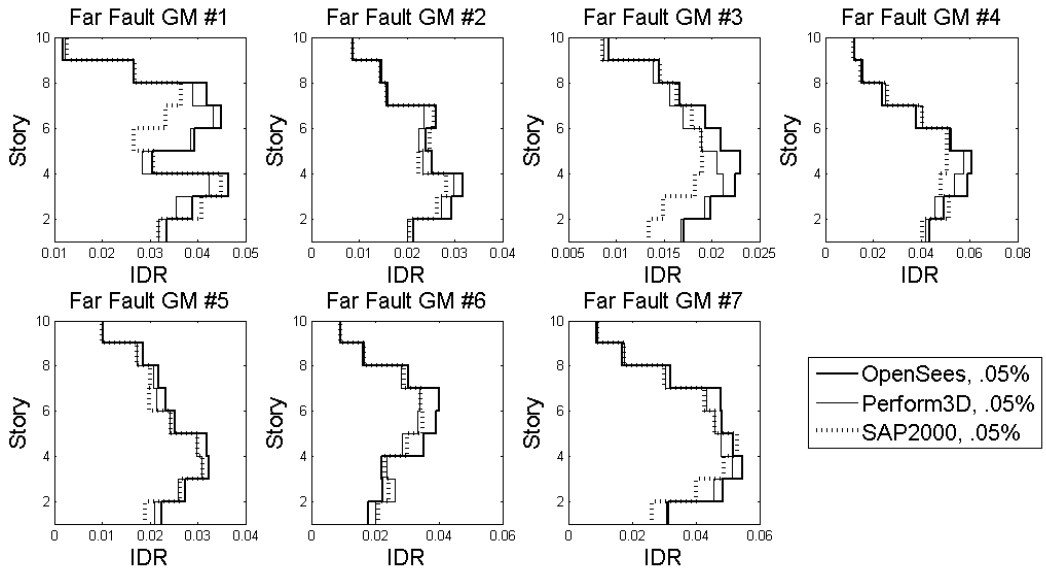

Figure 4: Comparison of computed peak inter-story drift ratios using moment-rotation hinges with 0.05% post-yield stiffness in OpenSees, Perform3D and SAP2000 from seven far fault ground motions

A comparison of the probability distributions of the maximum computed peak inter-story drift ratios of the seven near fault ground motions and seven far fault ground motions for the case of 0.05% post-yield stiffness can be seen in Figure 5. It can be noted that the median values and dispersions of the near fault results are quite similar, whereas the far fault results show more noticeable variation in both median value and dispersion.

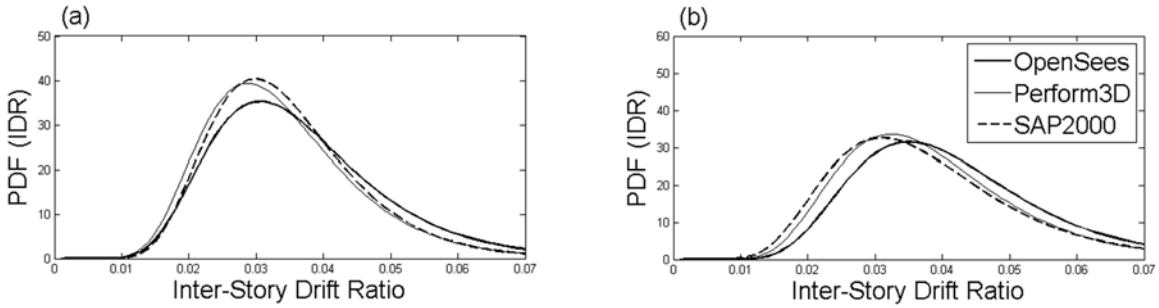

Figure 5: Probability distributions of the maximum computed peak inter-story drift ratios using moment-rotation hinges in OpenSees, Perform3D, and SAP2000: (a) 0.05% post-yield stiffness, near fault records; (b) 0.05% post-yield stiffness, far fault records

Nonlinear Simulations: Moment-Curvature Hinge Model

Two dimensional nonlinear models using moment-curvature hinges were completed in OpenSees, Perform3D, and SAP2000. The hinges were located at each end of each beam and column of the moment frame. Three different hinge length values were assumed, each expressed as a multiple of the beam depth (D): 1.0*D, 0.75*D and 0.50*D.

Nonlinear response history analyses using the seven far fault and seven near fault ground motions were performed on a total of nine different moment-curvature models: three models from each of the three software, reflecting the variations in hinge length mentioned above. The following assumptions were made for the nonlinear response history analyses for each of the nine models:

- Bilinear moment-curvature relationship with 0.05% post-yield stiffness
- No dummy columns included
- Include the effects of gravity columns and P-delta
- 5% Rayleigh damping anchored at the first and third modes and proportional to mass and *initial* stiffness (no modal damping)

A comparison of the computed peak inter-story drift ratios of each model, using a hinge length equal to the beam depth, from the set of seven near fault ground motions and the set of seven far fault ground motions can be seen in Figure 6 and Figure 7, respectively. Figure 6 shows very close agreement between the three models in most cases, with some significant variation at the lower levels in GM #3 with SAP2000. Figure 7 shows significant variation between the three models in most cases; GM #2 and GM #5 match fairly closely.

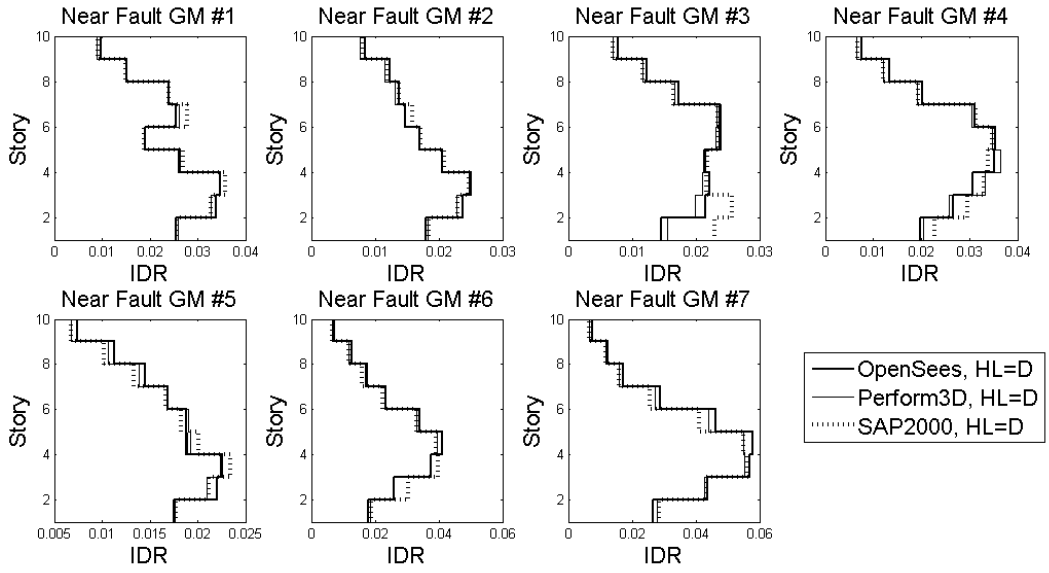

Figure 6: Comparison of computed peak inter-story drift ratios using moment-curvature hinges with hinge length (HL) equal to beam depth (D) in OpenSees, Perform3D and SAP2000 from seven near fault ground motions with forward directivity effects

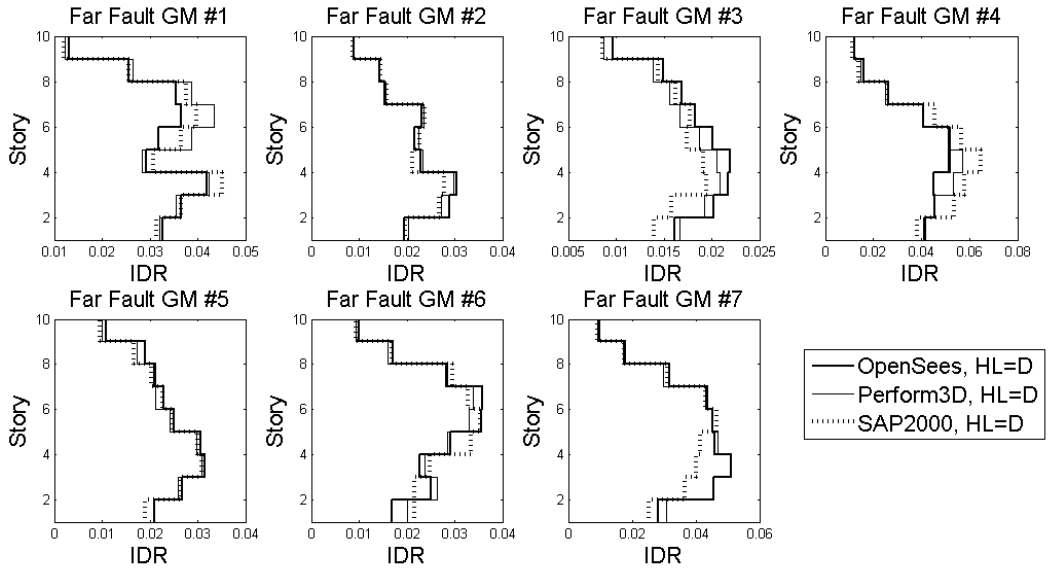

Figure 7: Comparison of computed peak inter-story drift ratios using moment-curvature hinges with hinge length (HL) equal to beam depth (D) in OpenSees, Perform3D and SAP2000 from seven far fault ground motions

A comparison of the probability distributions of the maximum computed peak inter-story drift ratios of the seven near fault ground motions and seven far fault ground motions for the case when the hinge length is set equal to the beam depth can be seen in Figure 8. It can be noted from the figure that in most every case the median values and dispersions are quite similar; Figure 8(b) shows some significant variation in both median value and dispersion.

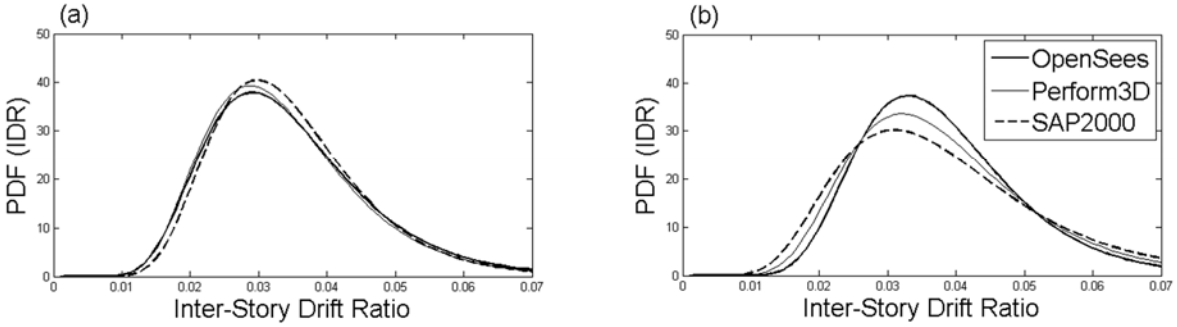

Figure 8: Probability distributions of the maximum computed peak inter-story drift ratios using moment-curvature hinges in OpenSees, Perform3D, and SAP2000:
(a) hinge length equal to beam depth, near fault records; (b) hinge length equal to beam depth, far fault records

Nonlinear Simulations: Fiber Hinge Model

Two dimensional nonlinear models using fiber hinges were completed in OpenSees, Perform3D, and SAP2000. The hinges were located at each end of each beam and column of the moment frame. Three different hinge length values were assumed, each expressed as a multiple of the beam depth (D): 1.0*D, 0.75*D and 0.50*D.

Nonlinear response history analyses using the seven far fault and seven near fault ground motions were performed on a total of nine different fiber hinge models: three models from each of the three software, reflecting the variations in hinge length mentioned above. The following assumptions were made for the nonlinear response history analyses for each of the nine models:

- Bilinear stress-strain relationship with 0.05% post-yield stiffness
- No dummy columns included
- Include the effects of gravity frames and P-delta
- 5% Rayleigh damping anchored at the first and third modes and proportional to mass and *initial* stiffness (no modal damping)

For each of the models in OpenSees, Perform3D and SAP2000 fiber hinges were located at the ends of the moment frame beams and columns. Nonlinear material relationships were confined to the hinge regions at the ends of these framing members, with the interior portion of the member set to perform in a linear-elastic manner. Each fiber hinge required a length and section definition be assigned to it. The section was defined by a combination of individual fibers, each with an associated cross-sectional area, location and bilinear stress-strain relationship.

No meaningful results were obtained from the SAP2000 fiber hinge models for either the near fault or far fault set of ground motions. The analysis for each of the ground motions in SAP2000 typically failed (convergence could not be achieved) within the first 10 seconds of the record.

A comparison of the computed peak inter-story drift ratios of each model, using a hinge length equal to the beam depth, from the set of seven near fault ground motions and the set of seven far fault ground motions can be seen in Figure 9 and Figure 10, respectively. Figure 9 shows close agreement between the two models in most cases, with some significant variation in GM #3. Figure 10 shows significant variation between the two models in most cases; GM #2, GM #5 and GM #7 match more closely.

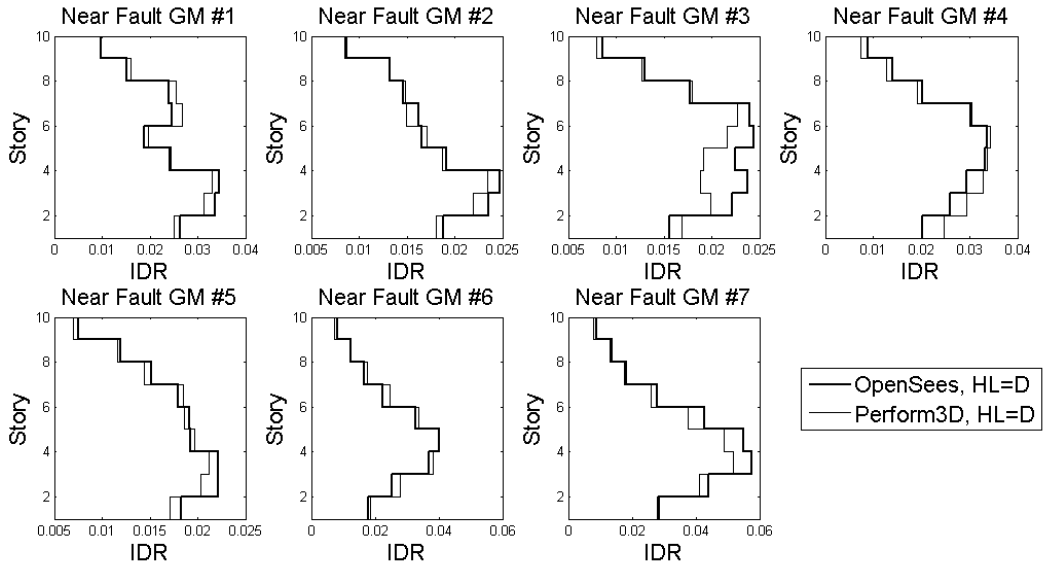

Figure 9: Comparison of computed peak inter-story drift ratios using fiber hinges with hinge length (HL) equal to beam depth (D) in OpenSees and Perform3D from seven near fault ground motions with forward directivity effects

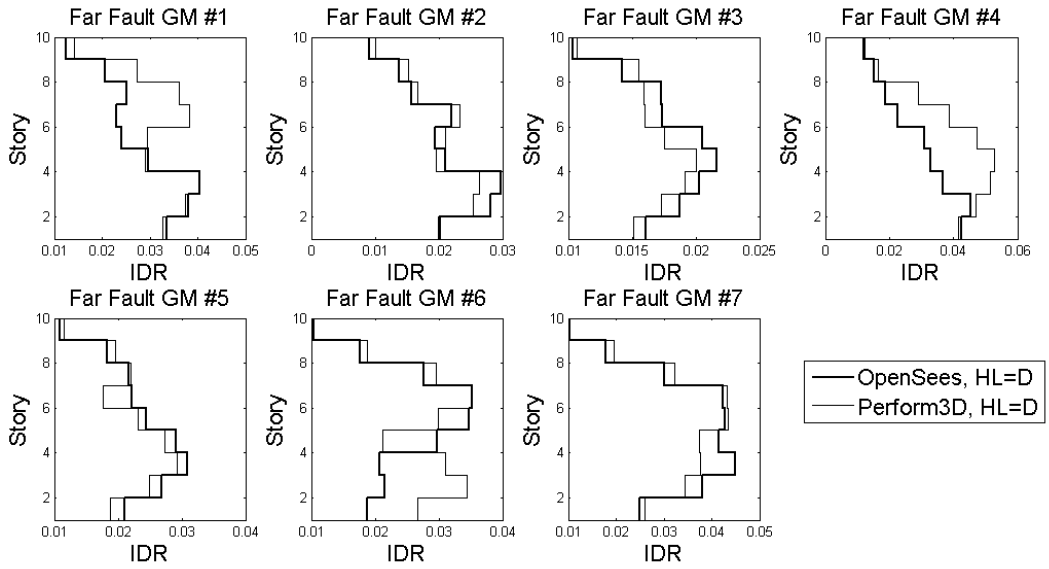

Figure 10: Comparison of computed peak inter-story drift ratios using fiber hinges with hinge length (HL) equal to beam depth (D) in OpenSees and Perform3D from seven far fault ground motions

A comparison of the probability distributions of the maximum computed peak inter-story drift ratios of the seven near fault ground motions and seven far fault ground motions for the case when the hinge length is set equal to the beam depth can be seen in Figure 11. It can be noted from the figure that in the case of the near fault records the median values and dispersions are quite similar between the models, while the results from the far fault records show greater variation in both median value and dispersion.

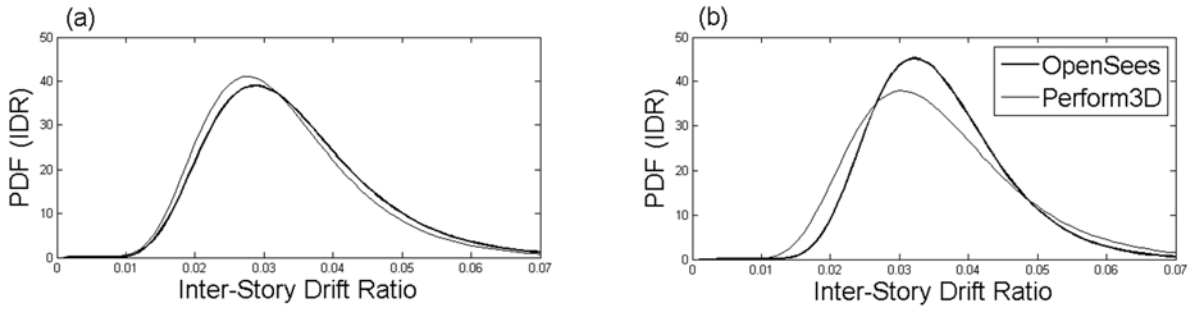

Figure 11: Probability distributions of the maximum computed peak inter-story drift ratios using fiber hinges in OpenSees and Perform3D: (a) hinge length equal to beam depth, near fault records; (b) hinge length equal to beam depth, far fault records

Concluding Remarks

For the case of moment-rotation hinges, the inter-story drift ratios resulting from the near fault ground motions compared fairly well both statistically and over the height of the building. The results from the far fault set of ground motions did not compare quite as well as those of the near fault set; the statistical results showed some variation in median value and there was greater variation over the height of the building (most notably with SAP2000). The inter-story drift results for the case of moment-curvature hinges mirror those obtained using moment-rotation hinges; the near fault results compare well both statistically and over the height of the building while the far fault results show slightly greater variation.

As mentioned previously, no SAP2000 results were obtained for the case of fiber hinges as convergence could never be achieved with either ground motion set. Significant variation can be seen in the far fault set of results between OpenSees and Perform3D over the height of the structure, and some modest differences in the statistical results. The near fault results show improvement over those from the far fault set.

Acknowledgements

The authors acknowledge the support provided by the California Department of Conservation, California Geological Survey, Strong Motion Instrumentation Program.

References

Foutch, D.A. and Yun, S. (2002). "Modeling of steel moment frames for seismic loads," *Journal of Constructional Steel Research*, 58 (2002), 529-564.

Swensen, D., and Kunnath, S. (2012). "Calibrating computer models for seismic analysis: case studies using instrumented building records." *Proceedings of the SMIP12 Seminar on Utilization of Strong-Motion Data*, Sacramento, CA, October 2, 2012, 57-68.

CALIFORNIA EARTHQUAKE EARLY WARNING SYSTEM – STATUS AND FUTURE DIRECTION

Richard M. Allen

Berkeley Seismological Laboratory
Department of earth & Planetary Science
University of California, Berkeley

Abstract

The demonstration earthquake early warning system, developed by the USGS, UC Berkeley, Caltech, ETH, and the University of Washington, named ShakeAlert, functioned well for the South Napa earthquake of August 24, 2014. The first ShakeAlert was generated by the ElarmS algorithm (Kuyuk et al., 2014) 5.1 sec after the origin time of the earthquake, and 3.3 sec after the P-wave arrived at the closest station 6.5 km from the epicenter. The initial alert was based on P-wave triggers from four stations, had an estimated magnitude of 5.7. The warning was received at the UC Berkeley Seismological Laboratory 5 seconds before the S-wave and about 10 sec prior to the onset of the strongest shaking. ShakeAlert beta-testers across the San Francisco Bay Area received the alert simultaneously including the San Francisco 911 center with 8 sec warning, and the BART train system. BART has implemented an automated train-stopping system that was activated (though no trains were running at 3:20 in the morning).

With the available network geometry and communications, the blind zone of the ElarmS alert had a radius of 16 km. The four stations that contributed to the first ElarmS alert all provide 1 second data packets, but the latency in transmitting data to the processing center ranged from 0.27 to 2.62 seconds. If all the stations provide data in 0.27 seconds, then the alert would have been available 2.3 sec sooner and the blind zone would be reduced to about 8 km. This would also mean that the city of Napa would have received about 1 second of warning. Overall the magnitude estimate and event location were stable from the initial alert onwards. The magnitude estimate did first increase to 5.8 and then dip to 5.4 2.6 sec after the initial alert, stayed at that level for 2 sec, and then returned to 5.7. The final magnitude estimate was 6.0 consistent with the ANSS catalog. In addition to the ElarmS contribution to the ShakeAlert, the Onsite algorithm also contributed with an initial alert 10.9 s after the earthquake origin time.

HIGHLIGHTS OF STRONG-MOTION DATA FROM THE M6.0 SOUTH NAPA EARTHQUAKE OF AUGUST 24, 2014

Anthony Shakal, Hamid Haddadi and Moh Huang

California Strong-Motion Instrumentation Program, California Geological Survey, Sacramento

Christopher Stephens

National Strong-Motion Project, US Geological Survey, Menlo Park

Abstract

The South Napa earthquake of August 24, 2014 caused the strongest shaking in the San Francisco Bay area since the 1989 Loma Prieta earthquake, 25 years earlier. Strong shaking occurred in the epicentral region, but low level shaking extended throughout the San Francisco Bay area. Over 400 strong motion records with peak accelerations above 0.5% g were recorded by the CISN seismic networks (BDSN, CGS/CSMIP, USGS/NCSN and USGS/NSMP) and these records are available at the CESMD website (www.strongmotioncenter.org) for view and download. Records with peak ground accelerations below 0.5% g are available for download at an associated FTP site.

Peak horizontal ground accelerations, velocities and spectral accelerations versus fault distance are compared with the ground motion predictions from Boore and Atkinson (2008; BA08). The comparisons show that the observed values are higher than would be predicted at distances less than about 20 km, while they generally drop off more rapidly with distance beyond that.

The last significant shaking in the Bay area was in the 1989 Loma Prieta earthquake. Many structures and sites have been instrumented since then, so this is the first set of significant data for many of these sites and structures. These structures include all of the major Caltrans toll bridges in the Bay area. For most of these bridges Caltrans also supported installation of geotechnical (downhole) arrays. The most striking new structure, the new Bay Bridge East Span, is not fully instrumented yet, though many channels were recorded. Another striking structure which recorded the first significant record is the recently instrumented concrete-core Rincon tower in San Francisco.

Strong-Motion Data from South Napa Earthquake

The Mw 6.0 South Napa earthquake occurred on August 24, 2014 at 03:20:44 PDT. The epicenter was at 38.216N and 122.312W, about 9 km SSW of Napa, California and about 82 km WSW of Sacramento, California. According to the USGS, the earthquake occurred near the well-known West Napa Fault. In the area of this earthquake, only the West Napa Fault is known to have displaced Holocene-age sediments. This earthquake was the most significant earthquake in Northern California since M6.9 Loma Prieta earthquake of October 17, 1989.

Strong-motion data were recorded from a total of over 445 CISN stations of the CGS Strong Motion Instrumentation Program (CSMIP), the USGS National Strong Motion Project (NSMP) and Northern California Seismic Network (NCSN), and the UCB Berkeley Digital Seismic Network (BDSN). The data also includes records obtained by the CA Dept. of Water Resources and P G & E. The stations are shown in the CESMD interactive map (Fig. 1) The strong motion stations include over 340 ground response stations, over 89 structures (buildings, bridges and other) and 14 geotechnical arrays. As of 6 October 2014, over 3000 channels (components) of strong-motion data are available for download through the Center for Engineering Strong Motion Data (CESMD) at www.strongmotioncenter.org. All of the ground-response data were used in the ShakeMap for the event. This note is focused on the engineering aspects of the strong motion data.

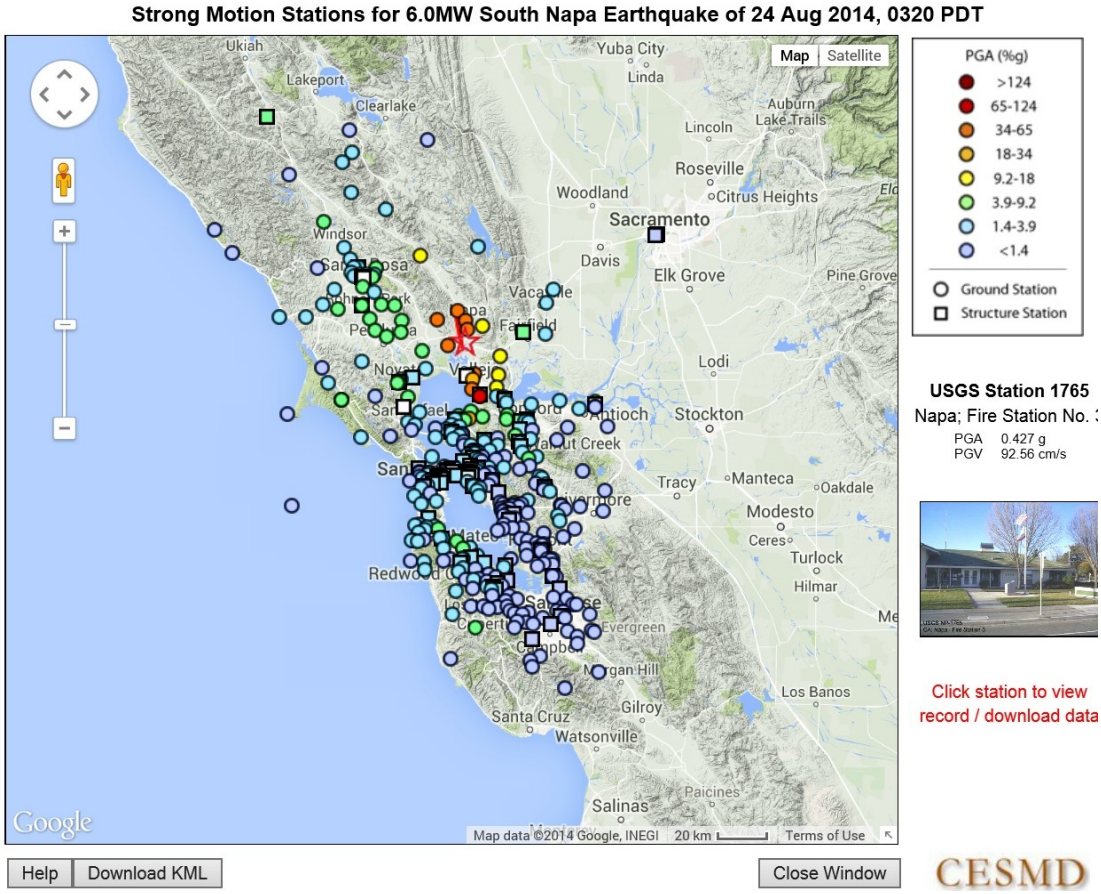

Figure 1. The interactive map at the CESMD website (www.strongmotioncenter.org) showing locations of strong-motion stations that recorded the South Napa earthquake.

The largest peak ground acceleration of 99%g was recorded by the surface instruments of the Crocket - Carquinez Br Geotechnical Array #1 (CGS 68206). The peak ground velocity at this station is 22 cm/s. A station on Main Street in downtown Napa (USGS N016), where the heaviest damage occurred, had a peak acceleration over 60% and a PGV of 47 cm/s. Napa Fire Station 3 (USGS 1765) in the northern part of Napa had the largest PGV, at 93 cm/s, with a PGA of 43%g. The duration of strong shaking was generally 10 to 15 seconds or less.

Near-Fault Ground Motions

Recorded ground accelerations in the Napa area and in the city of Vallejo are generally very strong with peak ground accelerations larger than 0.3 g. Many of the buildings in the Napa and Vallejo areas suffered damage to the chimneys and URM walls or facades. The recorded ground accelerations from five stations in the Napa area and three stations in Vallejo, in the east-west direction, are plotted on the CESMD interactive map in Figure 2. Perhaps due to the fact that the fault rupturing was from south to north (Dreger, 2014), the records in Vallejo tend to have two distinct arrivals separated by about 1.8 seconds. Although some of these records have relatively large peak accelerations, the peak velocities were not large because the peak accelerations were the results of high frequency motions.

Ground velocities integrated from recorded accelerations in the east-west direction are plotted on the CESMD interactive map in Figure 3. It is clear that the peak ground velocities in the Vallejo area are smaller than those in the Napa area. Some distinctly large velocity pulses are seen in the records in the Napa area. The largest peak ground velocity of 93 cm/s was recorded at NAPA Fire Station 3. It appears that the source mechanism plays a very significant role in generating large velocity pulses in the near field.

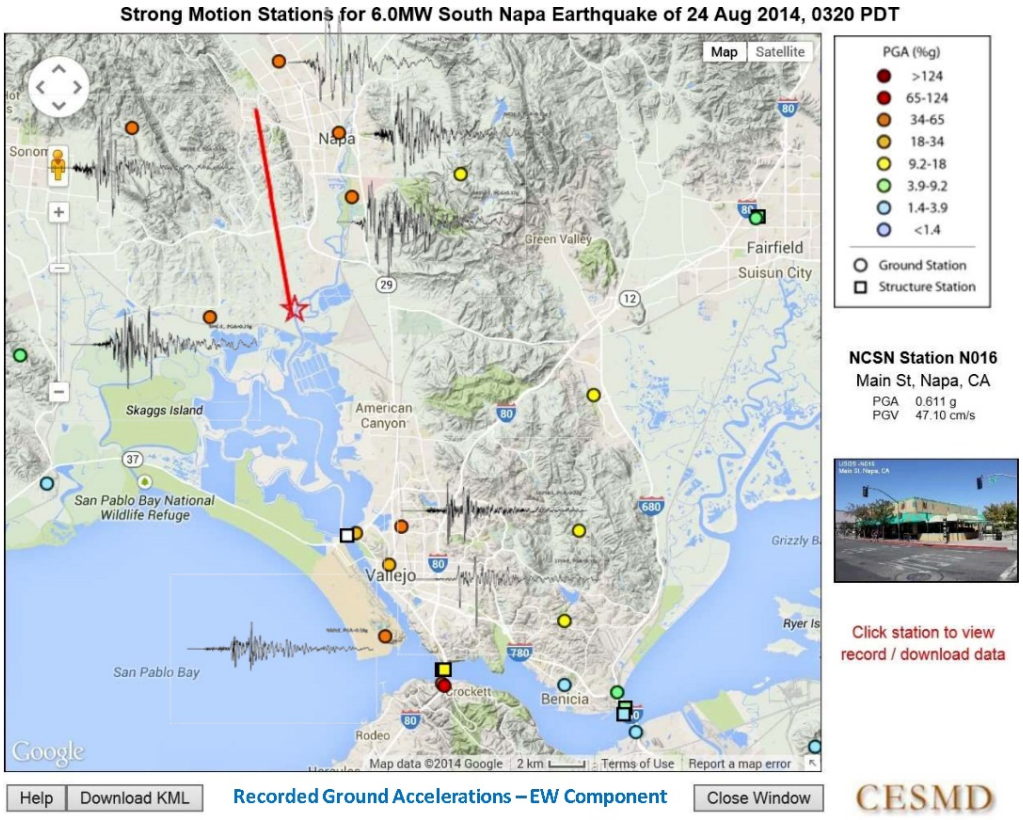

Figure 2. Recorded ground accelerations, EW component, in the Napa and Vallejo areas. Records of 20 seconds are plotted, with the same scale, on the CESMD interactive map.

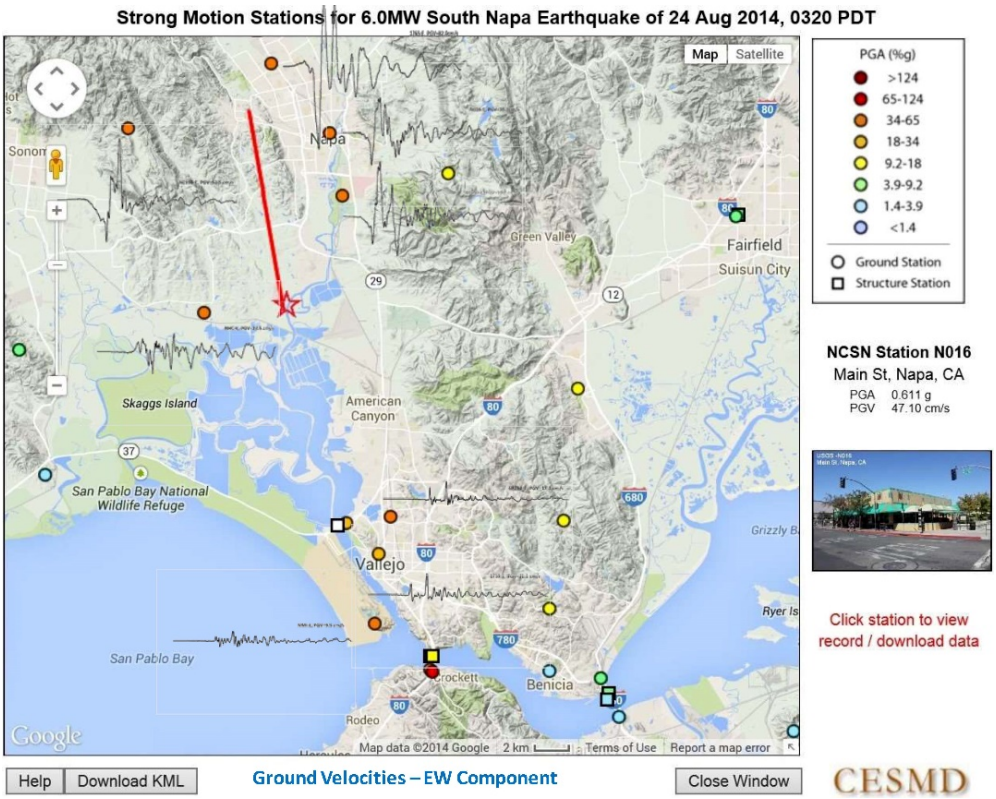

Figure 3. Ground velocities, EW component, in the Napa and Vallejo areas on the same base map as Figure2. Records of 20 seconds length are plotted, with the same scale, on the CESMD interactive map.

Peak Ground Motion Analyses

Peak Ground Acceleration

The Napa earthquake had high close-in accelerations that decayed relatively rapidly with distance. Figure 4 shows the geometric mean of the peak horizontal ground accelerations vs. the Rjb distance, the closest distance of a station to the projection of the fault model on the ground surface. The fault model was developed by Dreger (2014) at University of California, Berkeley and modified by Boatwright (personal communication) of the USGS.

The observed PGA values are compared with the ground motion predictions from Boore and Atkinson (2008; BA08) assuming a Vs30 of 760 m/s and strike-slip faulting. In general, the observed acceleration values are higher than the values that would be predicted at distances less than about 20 km, but many are within one standard deviation. Beyond that, the observed values generally drop off more rapidly than would be predicted, with many stations more than one standard deviation low.

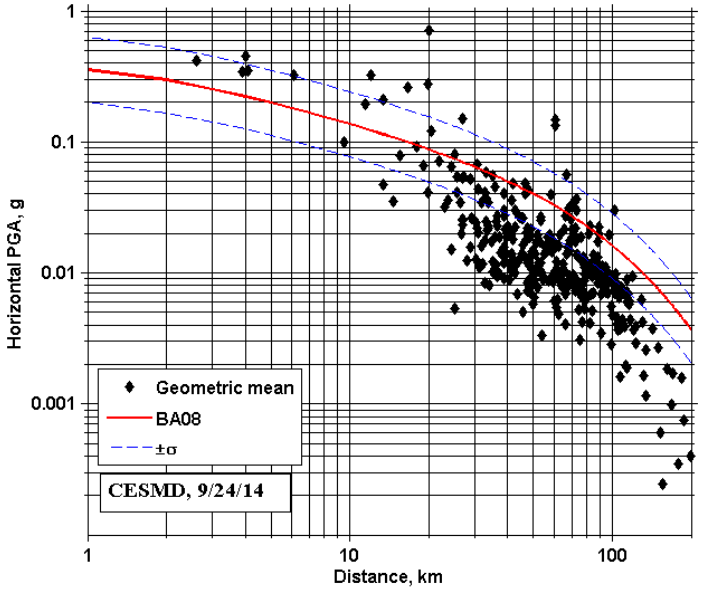

Figure 4. Peak horizontal ground acceleration (geometric mean) versus distance (Rjb), compared to the BA08 model of Boore and Atkinson (2008).

Peak Ground Velocity

It is also useful to compare the peak horizontal ground velocity vs. Rjb distance with the ground motion predictions of BA08, again assuming a Vs30 of 760 m/s and strike-slip faulting (Figure 5). The observed ground velocities are high close-in, but drop off beyond that. In general, the fit of the velocity data is better than that of the acceleration data.

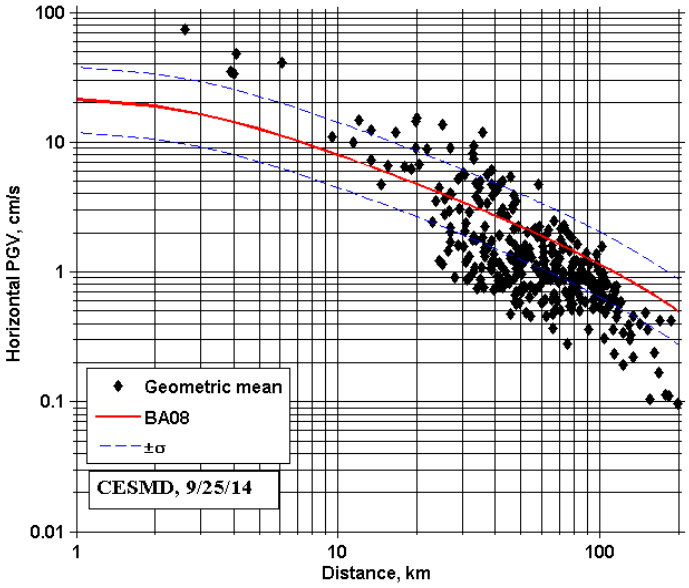

Figure 5. Peak horizontal ground velocity (geometric mean) vs. Rjb distance, compared to the BA08 model.

Spectral Acceleration

Spectral acceleration (geometric mean) values calculated at the three periods of 0.3, 1.0 and 3.0 seconds are plotted versus fault distance (Rjb) in Figure 6. Like the acceleration and the velocity versus distance plots, the spectral accelerations at the three periods also show higher observed values in the near field, and dropping off more with distance in the far field, compared to the spectral acceleration prediction of BA08.

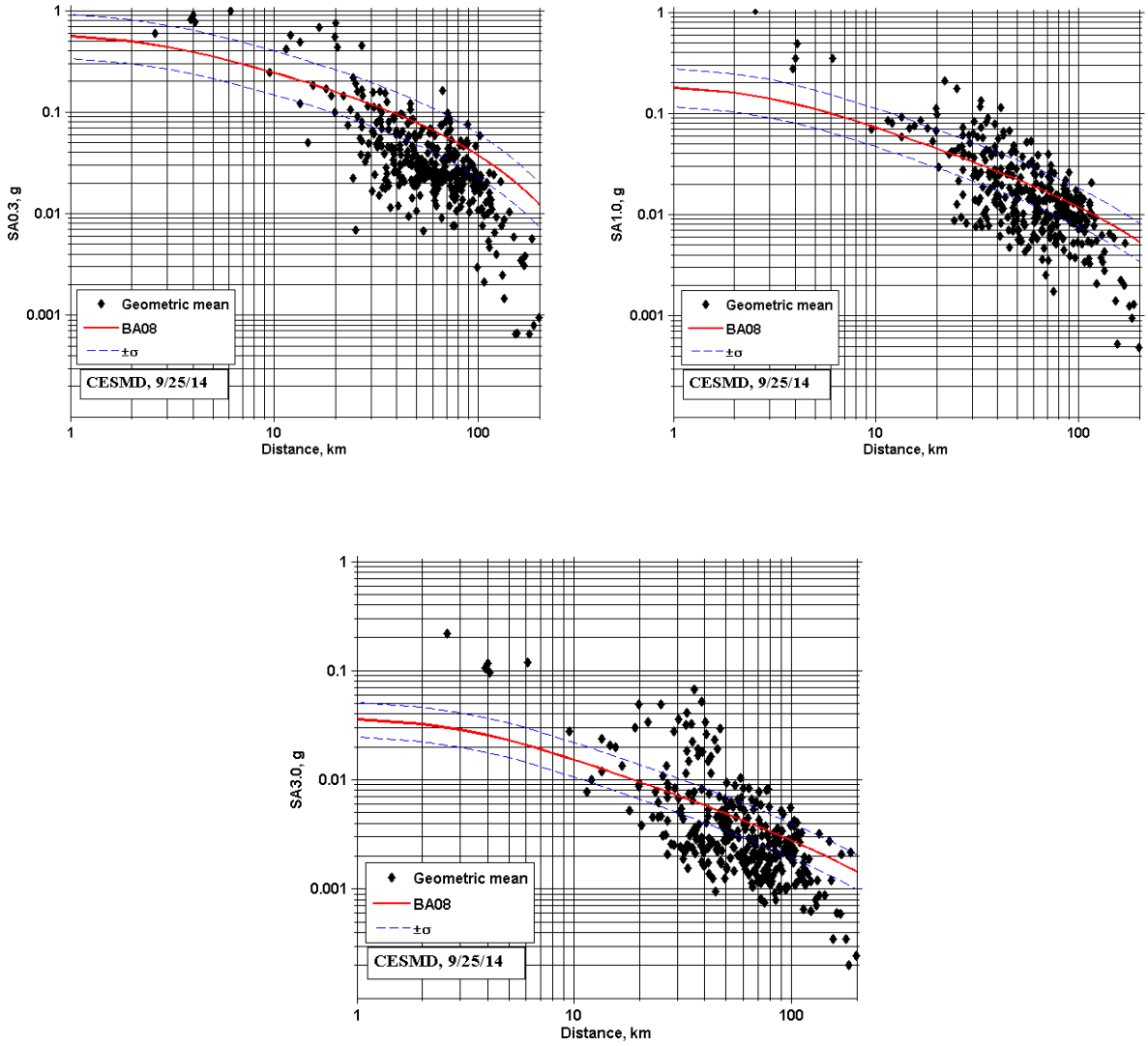

Figure 6. Spectral accelerations versus distance, compared to the BA08 model, for periods of 0.3 sec (upper left), 1.0 sec (upper right), and 3.0 sec (lower)

Strong-Motion Data from Geotechnical Arrays

Strong-motion data from the South Napa earthquake was recorded by14 geotechnical arrays and the data are available for download. The largest peak ground acceleration of 99%g was recorded by the surface instruments of the Caltrans-supported Crocket – Carquinez Br Geotech Array #1 (CGS 68206) near Crocket. The peak ground velocity at this station was 22

cm/s, not unusually high. It is striking that the Crocket – Carquinez Br Geotech Array #2, about 0.2 km from Array #1, recorded peak ground acceleration of 44%g on the ground surface instruments. The significant difference in ground motion at the two arrays could be due to site effects, path effects, structural response impacts. Studies to understand the motions are beginning. Figures 7 and 8 show strong motion acceleration plots at the two geotechnical arrays.

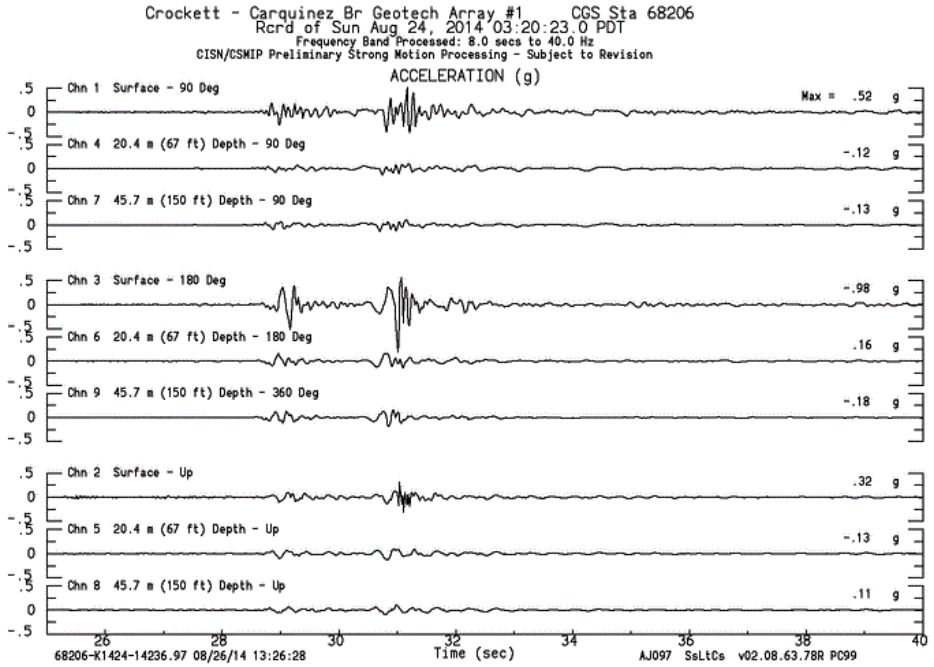

Figure 7. Strong-motion record of Napa earthquake at Crocket – Carquinez Br Geotech Array #1.

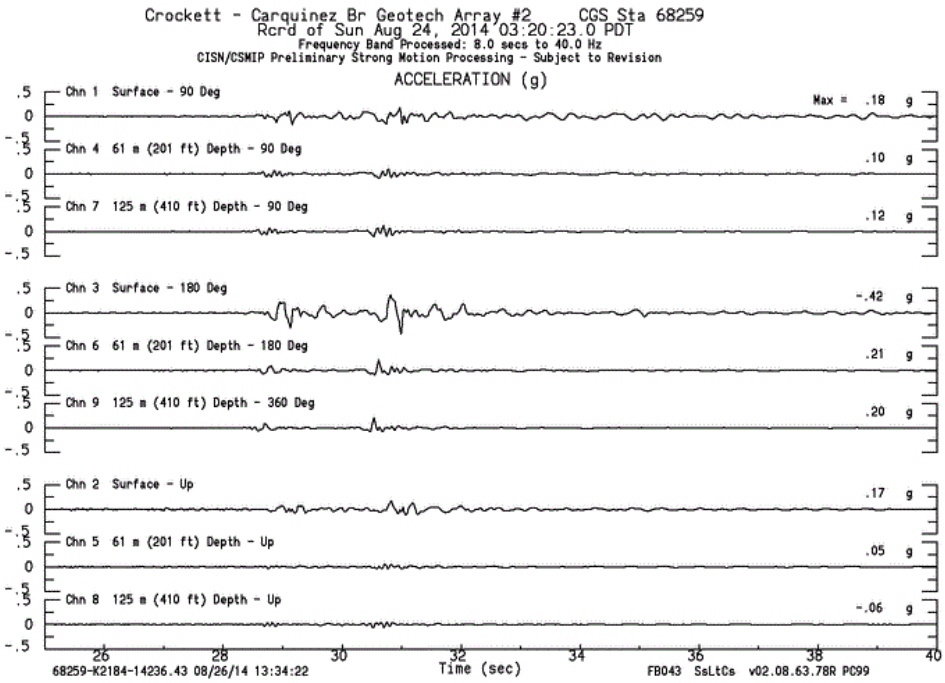

Figure 8. Strong-motion record of Napa earthquake at Crocket – Carquinez Br Geotech Array #2.

In addition to the South Napa earthquake mainshock, two aftershockes, an M3.6 on August 24 and an M3.9 on August 26, were recorded at the Geotechnical Arrays #1 and #2. Both aftershock epicenters were north-west of the geotechnical arrays, the first one at about 23 km distance and the second one about 16 km. Like in the mainshock, the observed ground motions from both aftershocks were larger at Geotechnical Array #1 ground surface, compared to those at the Geotechnical Array #2. The ratio of maximum ground acceleration at the Geotechnical Array #1 to the maximum at the Geotechnical Array #2 is 2.2 for the mainshock, and 1.8 and 1.7 for the two aftershocks. These observations suggest that the significant differences of peak ground accelerations at the two geotechnical arrays are probably not due to the source effects, since the mainshock and both aftershocks show the same high amplitude ground motion at the Geotechnical Array #1. Full understanding will await the results of studies now beginning.

Strong-Motion Data from Structures

Strong-motion records were obtained from a total of 89 structures during the South Napa earthquake. These structures include 64 buildings, 17 bridges, 3 tunnels/underground tubes, 4 wharves and 1 dam. Among 64 buildings, 11 are hospital buildings. Ten of the 17 bridges are toll bridge structures. The closest structure was the Hwy37/Napa River Bridge in Vallejo, 11 km from the epicenter. The peak ground shaking near the bridge is about 0.2g and the largest acceleration in the bridge response records is 0.66g. The closest building is the 3-story hospital in Fairfield, 24 km from the epicenter. Peak ground acceleration at the hospital is 0.04g, while the peak response of this steel structure was 0.17g. Many of the buildings in the San Francisco and Oakland areas experienced low-level ground shaking of only about 0.02g. However, records were obtained from buildings located in Sacramento and San Jose, which are about 82 and 105 km from the epicenter, respectively.

The most significant and important structural response records were obtained from Carquinez suspension bridge in Vallejo. This bridge is located about 19 km from the epicenter. The peak ground acceleration at the north abutment is about 0.08g and the suspension bridge recorded 0.79g on the main cable. The older bridge east of the suspension bridge, a steel truss structure, also experienced strong shaking and recorded high level of structural response. Both the north bound (concrete box girders) and the south bound (steel truss girders) bridges connecting Benicia and Martinez recorded structural response higher than 0.10g. The Golden Gate Bridge, 46 km from the epicenter, experienced larger structural response during the South Napa earthquake than in six previous earthquakes.

San Francisco – 62-story Residential Building

The first earthquake records were obtained from the 62-story residential building in San Francisco. The building is a tall concrete core shear wall structure. The instrumentation with 72 sensors was completed in 2012 in cooperation with USGS (Huang et al, 2012). Celebi et al. (2012 and 2013) analyzed the ambient motions due to wind to obtain the modal frequencies and mode shapes. Celebi (personal communication, 2014) does not see much difference in modal frequencies in the low-level seismic motion compared to the wind records.

Carquinez Suspension Bridge

The Carquinez suspension bridge was built and opened in 2003 to replace the original 1927 span. It is a cable suspension structure and is one mile long. The cable suspension bridge uses an isotropic steel box girder and has two concrete towers. The approach structure and the off ramp are concrete box girders. Both the main suspension and the off ramp structures were instrumented as part of the construction project. The suspension structure is extensively instrumented with 76 sensors while the approach structure and the off ramp were instrumented with 27 sensors (Huang et al., 2013). Sensors are placed along the height of both towers and in both anchorages. Sensors are planned to be installed on the pile cap and the pile tips at both towers, but they have not yet been installed. The suspended roadway is instrumented at eight locations along its length and typically accelerometers are placed inside the steel box girder. The box girder is continuous with shear keys at the towers. The box girder is allowed to move longitudinally and connected with viscous dampers at the towers. Sensors were also installed on the suspension cables at two locations to measure the transverse motions of the main cable. A geotechnical array (CGS 68259, Array #2) with sensors on the ground surface and at two depths was installed near the south anchorage of the bridge.

Before the South Napa earthquake, ambient motion data were recorded from the suspension bridge and were analyzed by system identifications to obtain the modal frequencies and mode shapes (Conte et al., 2008; Betti et al., 2008). The data from the South Napa earthquake is the first set of data obtained from the bridge during a seismic event. Although the design ground motions for the bridge are much higher than what the bridge experienced in the South Napa earthquake, the data provide excellent opportunities to calibrate the existing computer models and test various health monitoring methodologies.

Figure 9 shows 150 seconds of the recorded accelerations in the transverse direction at various heights of Tower T2. Peak accelerations were 0.159, 0.239, 0.164, and 0.126 g at the pile cap, lower strut, El. 80 m and the top, respectively. These peaks occurred during the first 20 seconds of ground shaking. The largest peak occurred at the lower strut, which supports the deck box girder. Close examination of the records shows that the tower was vibrating at a higher mode with a period of about 1 second. In this mode, the tower top was moving 180-degree out of phase with the lower strut. For the same locations, the corresponding displacements are shown in Figure 10. It is clear that after the ground shaking ceased, the whole bridge structure was in free vibration. The tower was dominated by the mode with a longer period (about 2.6 second), in which the tower displacements along its height are in phase. One can also compute relative displacements between these locations. For example, the maximum movement of the tower top relative to the pile cap is about 6 cm. Similar analysis can be performed for the motions of Tower T2 in the longitudinal direction, and Tower T3 in both directions.

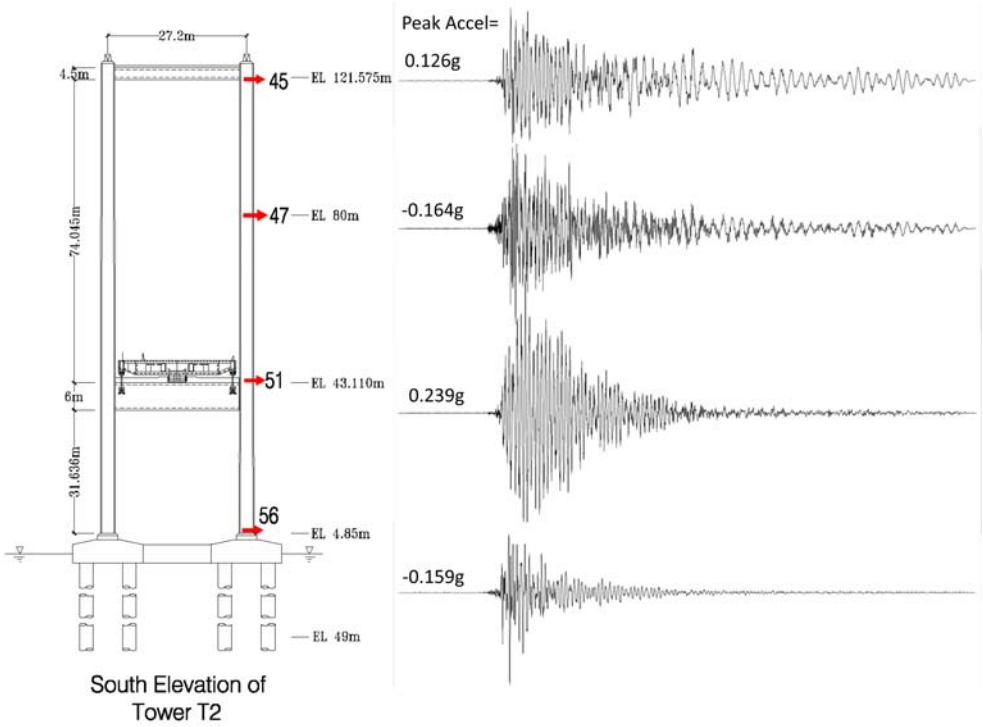

Figure 9. Recorded accelerations at Tower T2 of the Carquinez suspension bridge, in the transverse direction. Records of 150 seconds are plotted with the same amplitude scale.

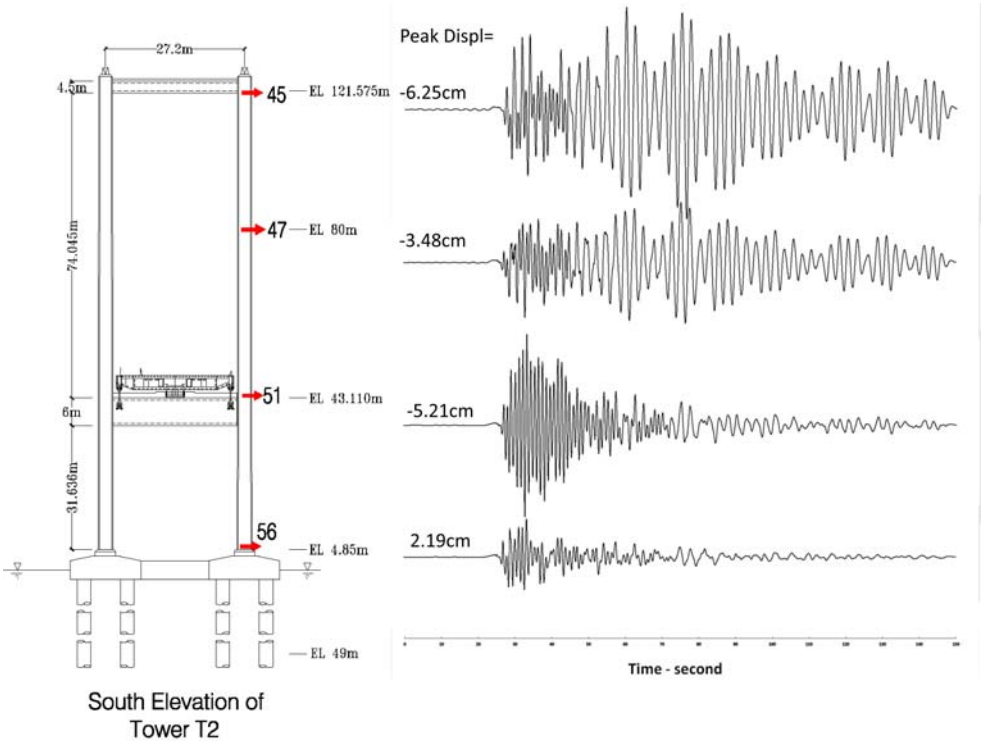

Figure 10. Displacements at Tower T2 of the Carquinez suspension bridge, in the transverse direction. Records of 150 seconds are plotted with the same amplitude scale.

Figure 11 shows 150 seconds of the displacements in the transverse direction along the deck box girder. For comparisons, the displacement at Abut A4 is also shown, which is much smaller than any points of the deck. The deck movement is constrained at both towers. It is interesting to observe that peak displacements occurred during the first 20 seconds for all locations and the amplitudes were not much different. The motions are dominated by a mode with a period of 0.5 second. However, in the later part of the record, the movements are larger in the center span than the side spans, and have a period of about 5.5 seconds, which is the period of the first mode (mainly transverse movement). Similar analysis of the records can be performed for the vertical and torsional motions of the box girder. Torsional response of the deck box girder seems to be dominant in the record.

More sophisticated system identifications can be performed on the records from many locations on the bridge. The modal frequencies and mode shapes can be compared with those derived from ambient vibration data to see how the bridge response parameters change from the baseline model parameters during the South Napa earthquake. These parameters can also be used to calibrate the existing finite element models for the bridge.

CSMIP Network Performance

The CSMIP program has a long-standing performance goal that 95% of the installed instrumentation should operate correctly in a given earthquake. Overall, the network performance was slightly less than that in this earthquake. However, that goal was reached and exceeded for conventional ground response stations, for buildings, and for hospital stations, each category had correct operation of over 98%. However, bridges and related stations were significantly less, near 85%. It was necessary to suspend maintenance late last year because of Caltrans funding shortfalls. Nonetheless, many good records were obtained, and the first records from many Caltrans-supported stations, because of the large number of new bridge installations that have come on in the last 5-10 years.

New Developments – New CSMIP Installations and New Types of Sensors

In-Pile Instrumentation

It is customary to locate strong motion sensors on the superstructure of bridges and other structures. However, it is desirable to know the motions input to the structure, through the piles under the structure. Installation of accelerometers in piles is significantly more difficult, technically, than other types of instrumentation. Downhole instrumentation in geotechnical arrays are similar, but the typical plastic (PVC) casing, and the controlled environment, make the installation easier. In-pile strong motion instrumentation requires steel casings, and in addition the construction environment means the casing often ends up with debris at the bottom, making the installation difficult. The first records obtained from sensors with known instrument orientation in downhole steel piles were recorded in this earthquake at the Benicia Bridge. The steel of the casing and the rebars in a pile make orientation via magnetic compass not possible, and other means had to be developed. CSMIP has several bridges for which in-pile instrumentation will be done as soon as an economical method to solve the debris problem is developed.

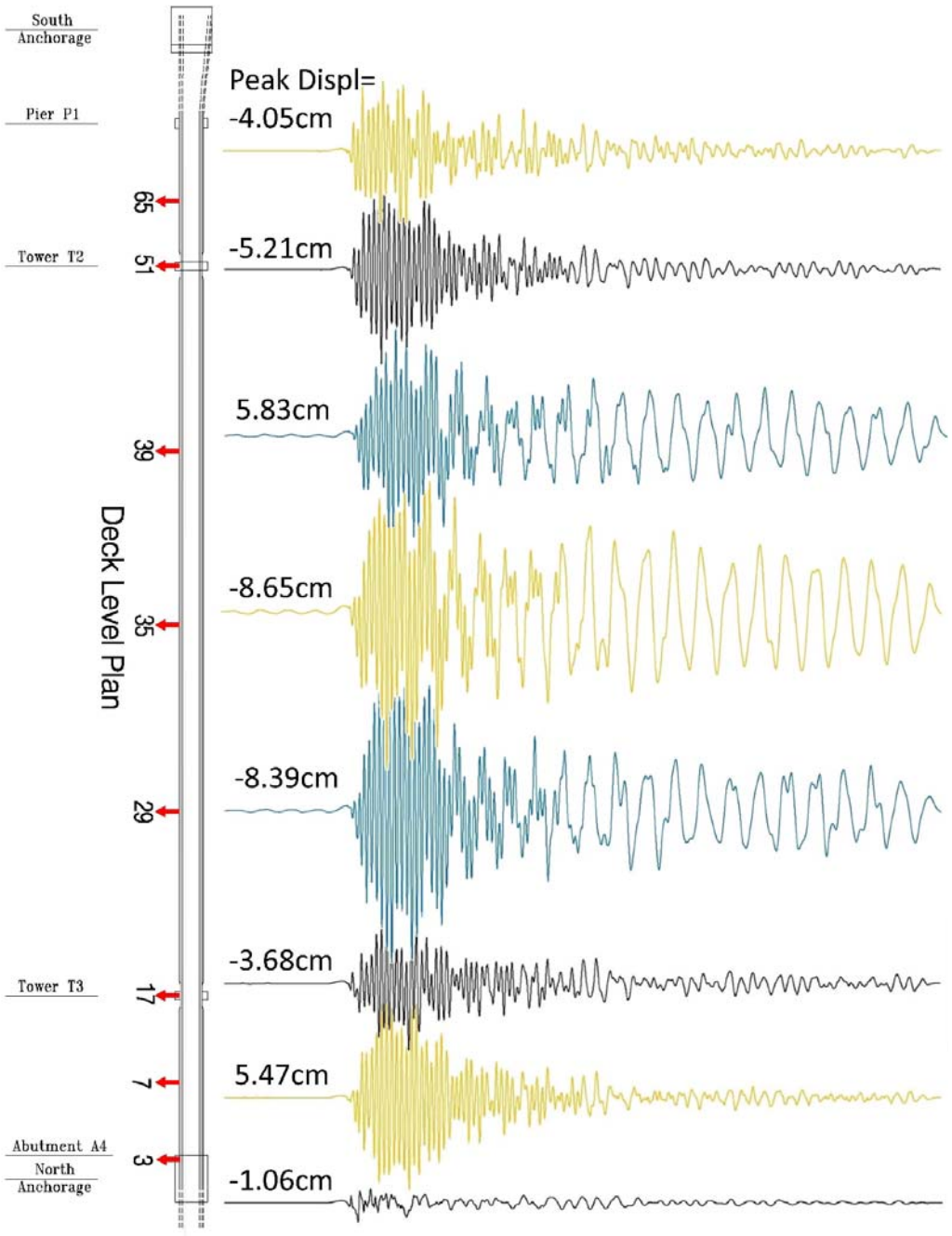

Figure 11. Displacements along the length of the deck box girder of the Carquinez suspension bridge, in the transverse direction. Records of 150 seconds are plotted with the same amplitude scale.

Strong Motion Instrumentation of Wharf Structures

The San Francisco Bay Conservation and Development Commission (SFBCDC) has begun requiring facilities in near-shore areas which are being built or modified to incorporate strong motion instrumentation. Two recently completed structures with strong motion

instrumentation include the Brannan Street Wharf in San Francisco (CGS 58559) and Redwood City's new shipping wharf (CGS 58566). The Brannan Street wharf sensor layout (Fig. 12) includes in-pile instrumentation, and Fig. 13 shows the data recorded at the pile tip, at 85 ft. depth. The wharf also includes instruments on the sea wall, as separate from the deck structure.

The Redwood City shipping wharf is the first case where SMIP has installed a tilt sensor on the structure, as reflected in the sensor layout in Fig. 14. (The new East Span of the Bay Bridge will also be instrumented with tilt sensors in the tower as construction is finished later this year.) Fig. 15 shows the tilt signal recorded, transverse to the long dimension of the structure. The data is also interesting as it shows apparent rotational motion of the wharf, that is, different transverse motion at the South end compared to the North.

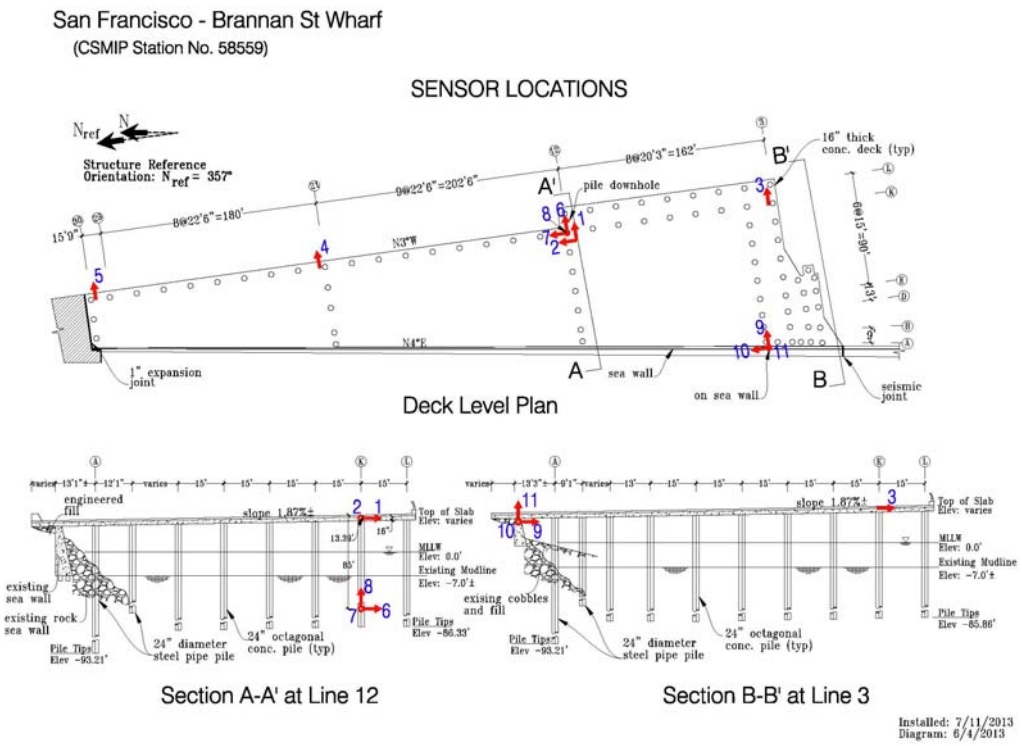

Fig. 12. Locations of sensors on the recently instrumented Brannan Street Wharf in San Francisco (CGS 58559). The instrumentation includes sensors in the pile-tip (sensors 6,7,8) and on the sea wall (sensors 9,10,11).

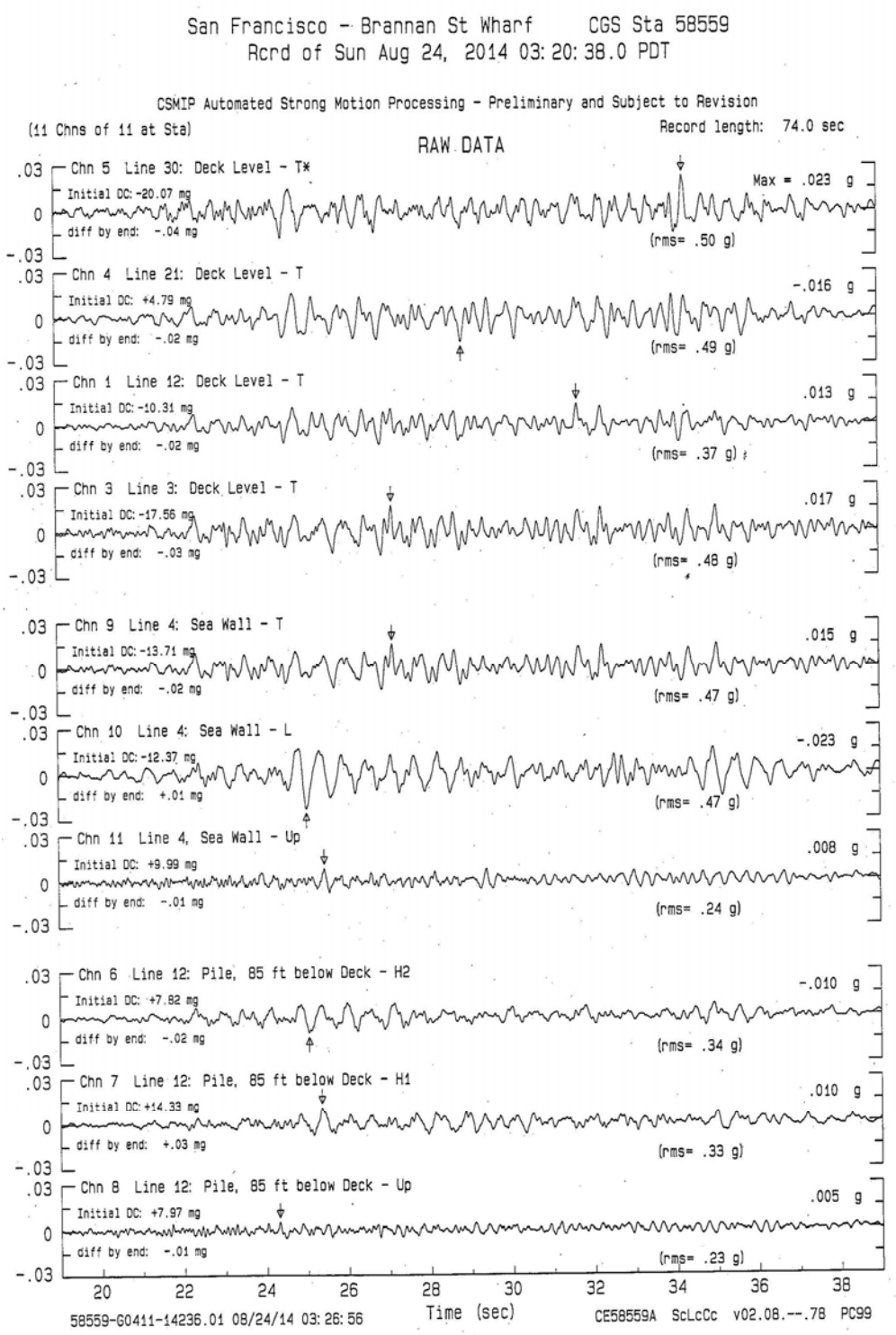

Fig. 13. Recorded accelerations at the Brannan Street Wharf during the South Napa earthquake, along the deck level (upper), sea wall (center) and at the pile tip (lower).

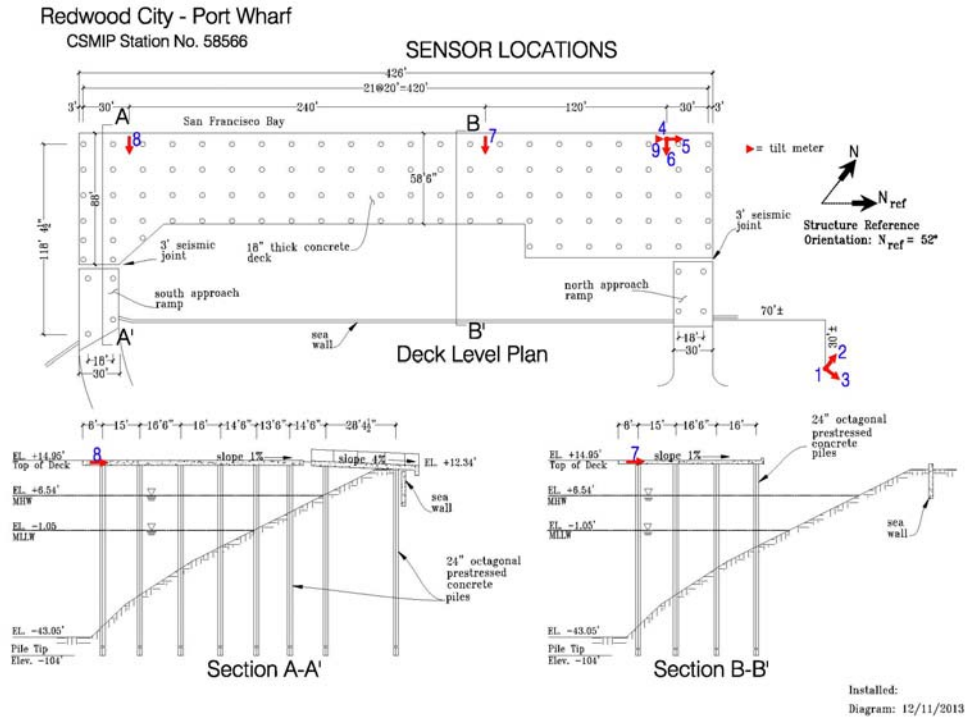

Fig. 14. Locations of sensors on the recently instrumented Redwood City Port Wharf (CGS 58566). The instrumentation includes three free field sensors, three transverse sensors along the length of the wharf (6,7,8) and a tilt sensor (9), sensitive to tilt around the longitudinal axis of the wharf.

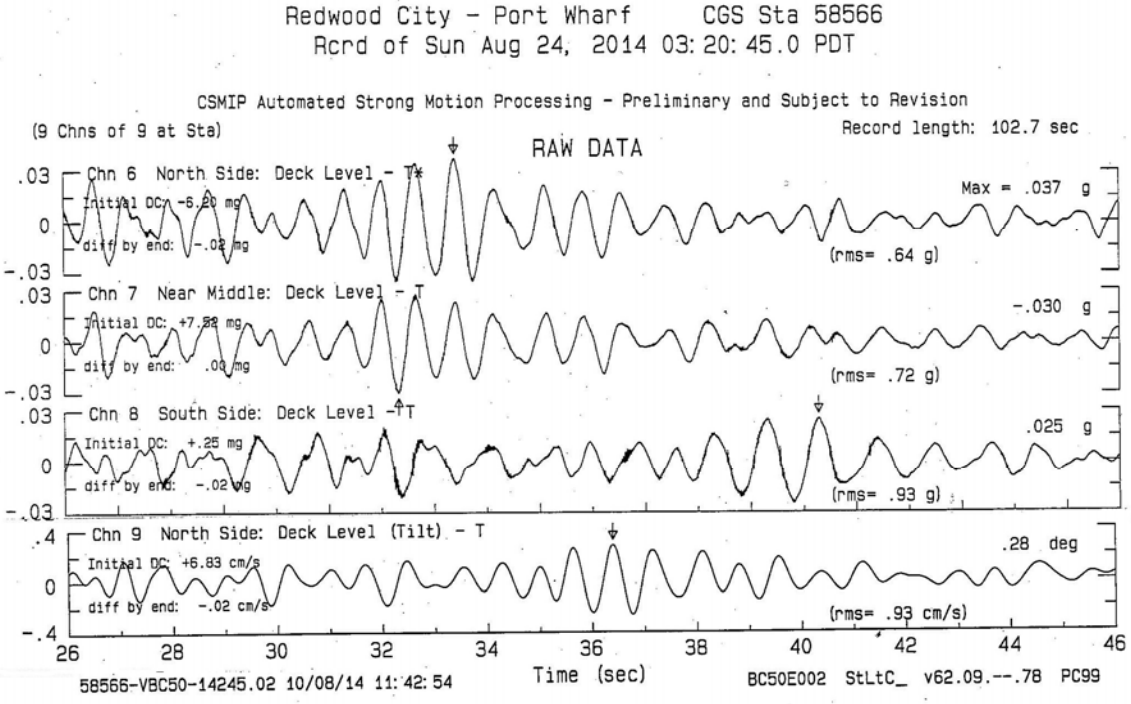

Fig 15. Recorded motions at the Redwood City Port Wharf during the South Napa earthquake, transverse accelerations (upper), and tilt (lower).

Direct Measurement of Relative Displacement in Strong Motion

Accelerometers can provide very accurate measurement of accelerations. If displacement is desired, however, accuracy is generally lower because the acceleration signal must be integrated twice, a process in long period noise increases. It is possible to obtain the relative displacement between two points on a structure without the long period noise problem if relative displacement sensors are used. CSMIP has been installing relative displacement sensors, between the superstructure of an isolated building and the base, for example, for many years. The first relative displacement sensors were installed as part of the Golden Bridge instrumentation in the mid-1990s. Despite the relatively large number of such cases, the first significant relative displacement record was not obtained until the 2014 Napa earthquake. Fig 16 shows the location of the measurement, made between a tower and the deck structure of the western suspension span of the Bay Bridge. Fig. 17 shows a plot of the relative displacement between the deck and Tower 3 of the west span of the Bay Bridge. The damper was installed as part of Caltran's retrofit of the West Span, and the sensor was recently added to the Caltrans-supported instrumentation system to measure the motion across the damper.

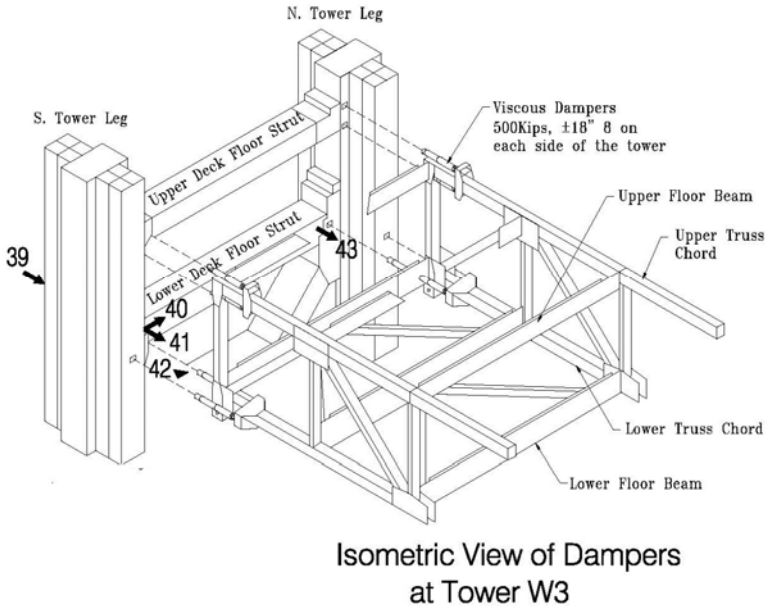

Fig 16. Location of the relative displacement measurement (sensor 42) measuring the relative displacement between the tower and the truss supporting the roadway.at Tower W3 of the West Span of the San Francisco Bay Bridge.

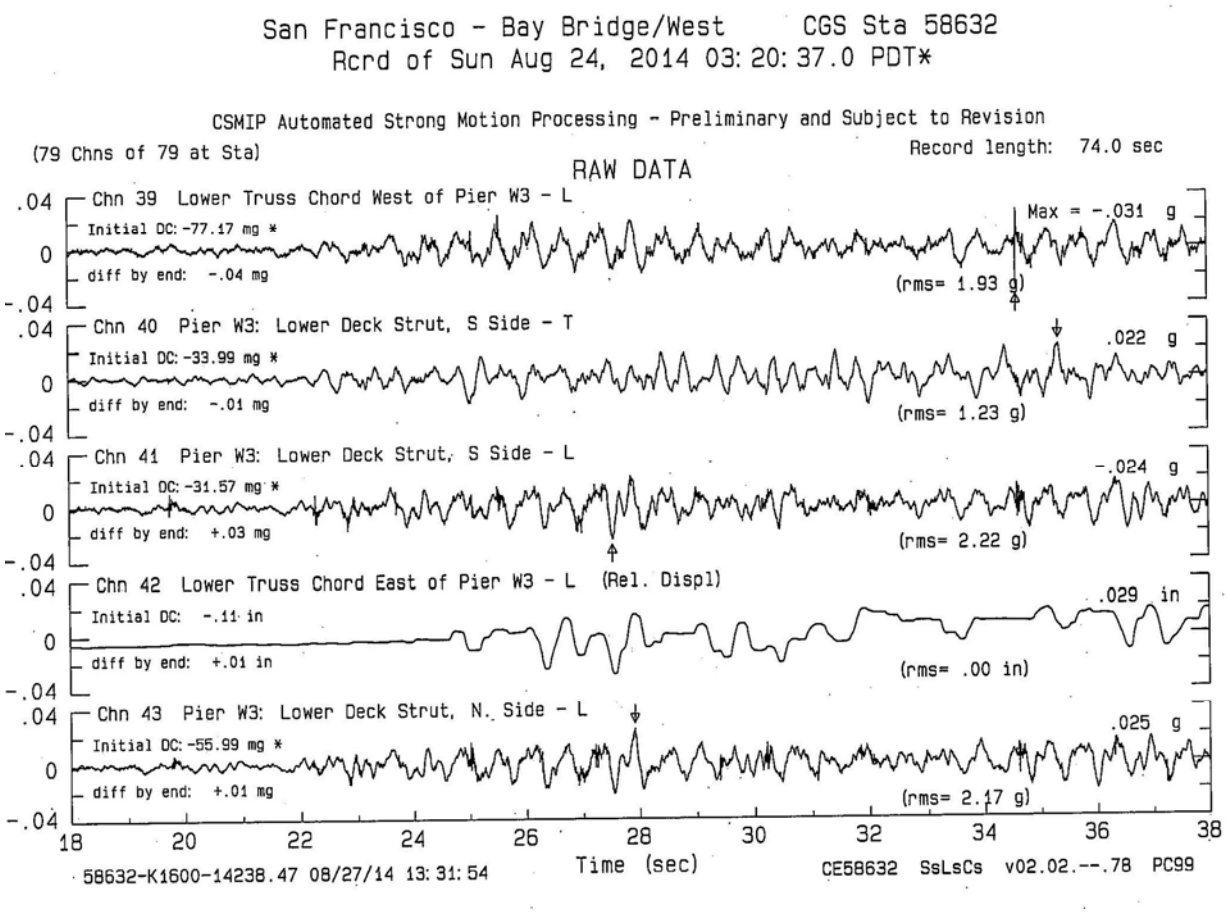

Fig 17. Relative displacement (chan 42; others are nearby accelerometers) between the tower and the roadway truss at Tower W3 of the West Span of the San Francisco Bay Bridge during the South Napa earthquake.

Cable Sensors

Recently instrumented suspension bridges have included sensors on the suspension cables themselves, as part of the Caltrans-supported instrumentation system. The Carquinez Bridge was the first bridge in which the instrumentation included accelerometers on the main cables at two locations. The nearly competed instrumentation of the new SFOBB East span now being completed also includes cable instrumentation, with triaxial sensors.

Petroleum Wharves

In recent years, the California State Lands Commission and the SFBCDC have encouraged strong motion instrumentation of petroleum wharf facilities, and SMIP has worked with the wharf owners to accomplish the instrumentation. The first outcome is an oil wharf near Richmond, which was instrumented in 2003, and good data was recorded during the Napa earthquake. The motion was low level, about 3% g. Oil wharves represent critical lifeline structures, and the measurement of their response during strong shaking is important. However, they also can present particularly difficult installation challenges, because of the explosion-proof

conditions that must be adhered to. Instrumentation is underway on two additional wharves in the Bay area, to be completed in the next several years.

Data Access

All of the data discussed here is available through the Center for Engineering Strong Motion Data (CESMD), a joint effort of the CGS California Strong Motion Instrumentation Program and the USGS National Strong Motion Project. The files for all records are available at www.strongmotioncenter.org, having gone through processing and error checking. Both the processed data and the raw data are available and can be downloaded. Users are encouraged to revisit this web site for updated information and data. The ground response data is also available from the CESMD Virtual Data Center at http://strongmotioncenter.org/vdc.

Acknowledgements

Station siting permission from property owners in the Bay area is acknowledged and appreciated. Careful field installation and maintenance work by field technical staff of both CGS and USGS was critical to successfully recording the strong motion during this earthquake, and it is also acknowledged and appreciated. Lijam Hagos's contribution in preparing ground motion figures is appreciated. Many of the records recovered in this earthquake would not be possible without the support of Caltrans, CalOES, OSHPD, DWR, Golden Gate Bridge, Livermore National Laboratory and BSEE.

References

Boore, D. M., and G. M. Atkinson (2008), Ground-motion prediction equations for the average horizontal component of PGA, PGV, and 5%-Damped PSA at spectral periods between 0.01s and 10.0s, *Earthquake Spectra*, *24*(1), 99-138.

CESMD, Center for Engineering Strong Motion Data Website, South Napa Earthquake of 24 Aug 2014, last visited on October 7, 2014. (www.strongmotioncenter.org)

Celebi, M., Huang, M., Shakal, A., Hooper, J. and Klemencic, R., Ambient Response of a Unique Performance-based Design Tall Building with Dynamic Response Modification Features, *Journal of the Structural Design of Tall and Special Buildings*, Volume 22, Issue 10, July 2013, Pages: 816–829

Celebi, M., Huang, M., Shakal, A., Hooper, J. and Klemencic, R. Ambient Response of a Unique Performance-based Design Building with Dynamic Response Modification Features, *Proceedings of SMIP12 Seminar on Utilization of Strong-Motion Data*, October 2, 2012, pp. 97 - 110.

Conte, J.P., He, X., Moaveni, B., Masri, S.F., Caffrey, J.P., Wahbeh, M. Tasbihgoo, F., Whang, D.H and Elgamal, A. (2008). "Dynamic Testing of Alfred Zampa Memorial Bridge." *Journal of Structural Engineering*, 134(6): 1006-1015

Dreger, D. (2014). Preliminary Finite Fault Results for the Aug 24, 2014 Mw 6.0 Earthquake 6 km NW of American Canyon, California Earthquake (Version 1) USGS Website at:

http://comcat.cr.usgs.gov/product/finite-fault/nc72282711/us/1409164884857/72282711.html, last visited on October 8, 2014.

Huang, M., Shakal, A., Petersen, C., Celebi, M., Hooper, J., and Klemencic R. Strong Motion Instrumentation of a 62-story Concrete Core Residential Building in San Francisco, *Proceedings of SMIP12 Seminar on Utilization of Strong-Motion Data*, October 2, 2012, pp. 81 - 96.

Huang, M., Hipley, P. and Shakal, A. (2013) Seismic instrumentation of Toll Bridges in California, Proceedings of the Seventh National Seismic Conference on Bridges & Highways, Oakland, May 20-22, 2013, Paper P10, 12 pages

Raimondo Betti, Ah Lum Hong (2008). Identification of the Baseline Modal Parameters of the Carquinez Suspension Bridge Using Ambient Vibration Data. *SMIP08 Seminar on Utilization of Strong-Motion Data*, September 28, 2008, pp. 63 – 82

USGS Earthquake Hazards Program Website, 2014 Significant Earthquakes Archive, M6.0 - 6km NW of American Canyon, California, last visited on October 7, 2014.